COMBUSTION SYNTHESIZED COBALT CATALYSTS FOR LIQUID FUEL GENERATION VIA FISCHER TROPSCH REACTION

A Thesis

Submitted for the degree of

Doctor of Philosophy

In the Faculty of Engineering

by

SNEHESH SHIVANANDA AIL

CENTER FOR SUSTAINABLE TECHNOLOGIES
INDIAN INSTITUTE OF SCIENCE
BANGALORE - 560012
FEBRUARY 2016

Dedicated to

my teachers

&

all my friends

Acknowledgements

I express my deepest gratitude to Prof S Dasappa for accepting me as a PhD student in the Center for Sustainable Technologies, for providing me with cutting edge tools and experimental facilities at the Combustion Gasification and Propulsion Laboratory (CGPL). I also thank him for the constant scholarly support. I would like to thank Dr N K S Rajan for arranging splendid computational facilities at CGPL and for his motivational thoughts. I am extremely thankful to Prof H S Mukunda for his valuable time, brilliant ideas and for all the inspiration. I expressly thank him for his book *Unerstanding clean energy and fuels from biomass*. I am also grateful to the entire team of technicians at CGPL - without their support none of the experiments would have been possible. My sincere thanks to the members of the CGPL students room and other friends at the Institute for useful discussions, suggestions and more than that for making my stay at the Institute lively and memorable. I would like to thank the Ministry of New and Renewable Energy (MNRE), Govt. of India for the financial support. I would also like to thank the National Center for Combustion Research and Development (NCCRD) for facilitating the analytical tools. I am thankful to Prof Kashinath C Patil for his time and steady encouragement. I extend my special thanks to my parents and my sister.

Contents

List of Figures

List of Tables

Abstract

This thesis is concerned with studies on the conversion of syngas to liquid hydrocarbons with the Fischer Tropsch (FT) reaction. A major part of the effort is aimed at synthesising the catalyst and use of it in a specifically designed high pressure-high temperature reactor to produce liquid hydrocarbons with FT synthesis. This study was motivated by two important considerations: (a) The predominant need to produce biomass derived liquid fuels such as gasoline and diesel. (b) Identify the key catalyst properties that influence the hydrocarbon yield and accordingly synthesize catalysts that compare with the commercially available catalysts or with the catalysts from vast literature sources. The specific areas of this research are: (i) Produce active, efficient catalysts from basic materials and characterise them for Fischer-Tropsch process, (ii) Build a reactor for operations at suitable pressure and temperatures and test the conversion process that involves various catalysts depending on the process used for producing them with the principal control parameter being the residence time and (iii) Examine the economics of building such systems at smaller throughputs of particular reference to India.

Cobalt catalysts supported on alumina and silica-doped alumina (SDA) were synthesized by incipient wetness impregnation (IWI) method and combustion synthesis (CS) method. The CS catalysts have been developed and used for several industrial reactions, especially environmental catalysts. However, its use for FT reaction has been limited to a few laboratory scale studies. The major drawback for CS process is the large heat release and temperature rise rates, resulting in the evolution of combustion products with uncontrolled explosion, eventually powdering the catalysts and in most cases resulting in the loss of active components. Such vigorous behaviour of CS reaction is distinctly evident for metal loading above 5%. The use of these powdered catalysts in a fixed bed reactor demands either re-pelletizing or re-moulding which is considered very disadvantageous. The CS catalysts used in this thesis have been deposited over support spheres with a metal loading of 20% and without affecting the integrity of the support structure. During the course of this study, the functionality of IWI catalysts were compared to that of CS catalysts and also the effect of supports on FT reaction were investigated.

The Al_2O_3 supported (1 mm diameter spheres, BET surface area = 158 m^2/g, pore volume = 0.45 ml/g) cobalt catalysts were synthesized using the CS and IWI method. CS catalysts were synthesized using hexamethylenetetramine (HMT) as the fuel. The synthesized catalysts resulted in an average cobalt oxide crystallite size of 7 - 10 nm and metal dispersion ranging from 11 - 13.5%. The X-ray photoelectron spectroscopy and the H_2 chemisorption analysis of the synthesized catalysts showed that the CS catalysts display reduced metal support interaction in comparison to the IWI catalysts. Strikingly, the Al_2O_3 supported CS catalysts reduced at temperatures that are 350 K higher than reduction temperatures of IWI catalysts, a feature not explicit in literature. The high reduction temperatures were associated to the reduction of surface Co^{2+} ions in the Co^{2+} - Al^{3+} spinel structure.

A further effort was made to synthesize cobalt catalysts directly in a single step without the need for further reduction by employing fuel rich conditions (equivalence ratio (ϕ) of 1.2 and 1.5). It was observed that, even under the fuel rich conditions, the redox mixture interacts with the atmospheric oxygen, yielding Co_3O_4. These catalysts (CS-ϕ = 1.2, and CS-ϕ = 1.5) were characterised by higher degree of reduction (DOR = 75% and 77% respectively) and higher dispersion (D=12.8% and 13.2% respectively) compared to the CS catalysts synthesized with unity equivalence ratio (DOR = 69% and D = 11%).

The Al_2O_3 supported CS catalysts resulted in an increased FT activity, as the CO conversion increased from 32% for IWI catalysts to 41% for CS catalysts. Similarly, enhanced CO conversion rates were observed for CS catalysts synthesized with ϕ=1.2 and 1.5, with a highest CO conversion of 61% for CS (ϕ = 1.2). Strikingly, the FT product spectrum reported a maximum weight fraction of wax hydrocarbons (C_{24+}), allowing for higher degree of surface polymerization for CS catalysts. The formation of waxes reduced with increasing equivalence ratios.

In order to further examine the support influences on catalytic activity, cobalt was impregnated into 40 wt.% silica doped alumina supports by IWI and CS method. Therefore, the second part of this thesis investigates the effect of 40 wt.% silica doping in alumina support on the properties of the synthesized catalysts and thereupon the FT activity and selectivity. The effect of metal support interaction and its consequent effect on the FT activity and hydrocarbon selectivity were investigated. A 34% increase in the degree of cobalt reduction is

observed for SDA-CS catalysts, compared to Al_2O_3 -CS catalysts. In addition, the fraction of active cobalt sites increases by a margin of 48% for SDA-CS catalysts. A 16% increase in the CO conversion was recorded for SDA-CS catalysts compared to Al_2O_3 -CS catalysts, with a 12% increase in the C_{5+} hydrocarbon yield.

The results of the product spectrum of SDA supported cobalt catalysts explicit the formation of middle distillate hydrocarbons (C_{10}-C_{20}) as the primary liquid hydrocarbon product, compared to waxes (C_{24+}) for Al_2O_3 supported cobalt catalysts. The difference in the product spectrum for alumina and SDA supported catalysts was attributed to the enhanced surface acidity of the SDA support. NH_3-TPD analysis of the SDA support showed a 91% excess surface acidity compared to the Al_2O_3 support. Additionally, the effect of the bed residence time on the overall conversion was determined. Reducing the space velocities from 2610 ml/h·g_{cat} to 873.3 ml/h·g_{cat} increased the hydrocarbon yield by 86% with the product spectrum gradually shifting from waxes to the liquid hydrocarbons.

The third part of this thesis is related to evaluating the overall energy conversion of biomass to liquid fuel, coupled with the techno-economics of BTL systems for an annual consumption of a nominal 10000 tonne woody biomass system with expected liquid hydrocarbon output of 1500 tonnes, a size, if found economical would be of great importance to the field. Detailed capital cost estimates for each section involved in the BTL system are set out, on the basis of which future commercial large-scale facilities producing fuel and/or power are evaluated. Cost analysis involving a 1000 kg/h steam-oxy biomass gasification plant paired with FT plant has been evaluated. The gasifier considered in this analysis is the downdraft reactor configuration, operating on oxy-steam system at an equivalence ratio of 0.1 and a steam to biomass ratio in the range of 0.8 - 1.2 to generate syngas with H_2/CO ratio of 2.1:1. The exit syngas from the gasifier comprises 47% H_2, 22% CO, 27% CO_2 and 4% CH_4 (by volume). For a once-through FT reactor configuration, substantial energy exists in the gas phase, which includes C_1-C_5 hydrocarbons and unconverted syngas. The analysis shows that, a market competitive liquid fuel can be produced with a CO conversion greater than 60%, at a cost ranging from 35 to 40 Rs/litre (0.5 - 0.6 USD/litre) with electricity as a major co-product in the BTL system. The results

emphasize that an economically affordable and environmentally favourable BTL system can be produced even at the levels discussed here. It can only be expected that at larger levels, the economics will be even better.

Chapter 1

Introduction

This chapter provides an introduction to the current global energy scenario and supports the need to produce liquid fuels from biomass, exclusively by the Fischer Tropsch reaction. The chapter reviews the current status of biomass to liquid fuel conversion and focuses on the technological developments in the FT process.

1.1 Background

Several nations across the globe, since past two decades, are working towards creating technologies and devising policies to secure uninterrupted energy for their citizens. Petroleum products derived from crude oil, even to the present day, act as an imperative demand for the current energy and economic situation.

Globally, oil is known to provide close to 33% of the the total energy consumption. In 2014, total oil consumption stood at 91 million barrels per day [Sieminski, 2014]. Liquid fuels, mostly transportation fuels, account for the largest factor in global oil consumption and the demand continues to grow steadily. According to International Energy Outlook-2011 [Conti et al., 2011], liquid fuel consumption increases at an average rate of 1% from 2008 to 2035 and is expected to continue dominating the transportation sector, even with increasing fuel prizes. Economically developing nations, India and China, show increasing energy demand further increasing its grip on the tightening oil supply. The bottom line being, with the ever increasing demand of the depleting resource, oil prices will continue to be dictated by countries with the largest oil reserves, *regardless of their production capability*. India consumes 3.7 million barrels per day (mbpd) of oil and produces just 0.98 mbpd. For a country which imports nearly 75% of its crude oil, a need indubitably arises for the use of sustainable energy

sources.

Apart from the economic considerations, use of alternative sources of energy are also called for owing to the increased concentration of anthropogenic greenhouse gasses. Rising concentrations of CO_2 in the atmosphere cause a positive radiation forcing resulting in high surface temperatures and rising sea levels. As reported by Meehl et al. [2005], even if GHG emissions are immediately stabilized, the thermal inertia gained by the climate system would still cause unrelenting rise in sea levels for next 100 years. No doubt, essential riddance of the emissions is instantly required for stabilizing the planet temperatures, sea level rise and creating opportunities for a sustainable development. All possible ways to *fix* the GHG emissions have to be considered to restore the climate change. Based on the sectoral global CO_2 emissions, major GHG emissions are generated by the energy sector (electricity and heat production). A quarter fraction of the total anthropogenic emissions are released by electricity and heat production unit, while 14% of the direct GHG emissions are contributed by the transport sector [Pachauri et al., 2014]. Except for a few cases, all prime modes of transport use combustion of liquid fossil fuels, and the total emissions for Indian transport sector was 258.1 Tg in 2003-2004, with highest contribution from roads and aviation transport. 18% of India's total CO_2 emissions arise from its transport sector, while for OECD (Organisation for Economic Co-operation and Development) nations, 30% of the overall GHG emissions are from the transport sector. Despite rigid transport related emission norms, the GHG outpouring by itself cannot be reduced entirely by changing to fuel efficient vehicles. The fuels itself must be less carbon intensive - *sustainable liquid fuel*

Amongst the alternative energy sources, biomass plays a major role in the energy sector. The only natural, renewable carbon resource and large fraction of substitute for fossil fuels is biomass. A wide range of biomass based materials have been proposed for use, which include crop residues, agro-crops and several tree species. These products can be burnt directly for energy and can also be processed further for conversion to liquid fuels like ethanol and diesel [Dhillon and von Wuehlisch, 2013]. Thermal processes offer an effective means for the conversion of the energy content of the wood and other lignocellulosic biomass. Wood constitutes 80 percent or more of volatile matter and nearly 20% char can be converted to gaseous fuels. Biomass to liquid (BTL) is suggested to be a

positive route to reduce the inclination towards fossil transportation fuels and is also a key to keep the environment clean [Hamelinck and Faaij, 2006]. For 20% of the total liquid fuels produced from carbon neutral sources, like biomass, 15% CO_2 emissions reduction could be achieved - just by fuel replacement [Butterman and Castaldi, 2009]. All the more, biomass is subjected to several processes for generation of liquid fuels. These processes include, fast pyrolysis of biomass, transesterification of vegetable oils to produce diesel fuel, production of bio-ethanol from agricultural crops to blend with gasoline, production of bio-oil from algae, and most recently the Fischer Tropsch process for conversion of biomass derived syngas to higher hydrocarbons. The following paragraphs briefly describe the above mentioned processes for biomass to liquid fuel generation (BTL), as indicated in Fig 1.1.

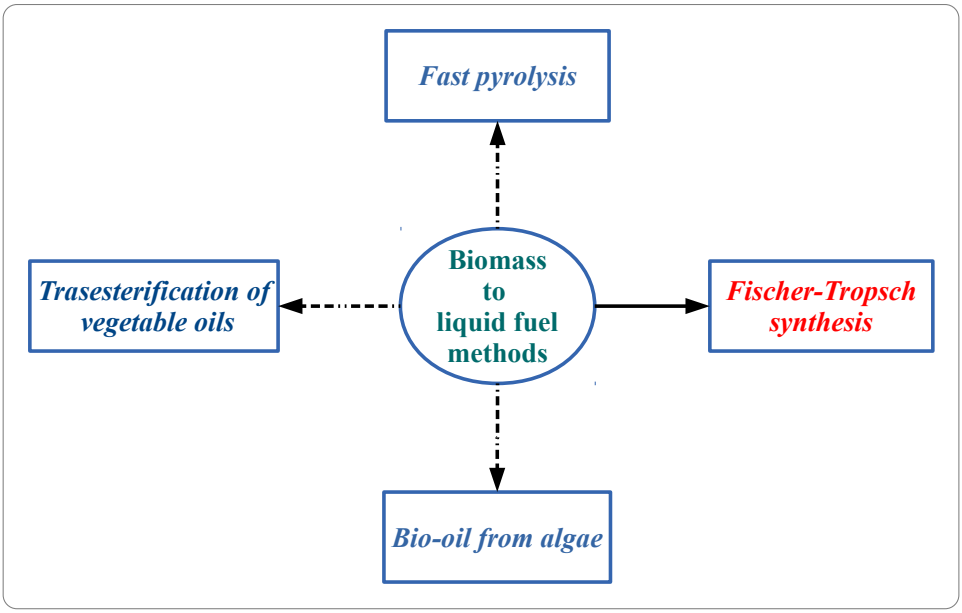

Figure 1.1: Widely used methods of converting biomass to liquid fuels

1.1.1 Fast pyrolysis

Fast pyrolysis of biomass includes treating of biomass in the absence of O_2 in the temperature ranges of 450-500 °C, at heating rates of 10^3-10^4 K/s with vapour residence times of 1s [Goyal et al., 2008] [Bridgwater, 2012]. The main constituent of this process, pyrolytic-oil, contains 75-80 wt% polar organics and 20-25 wt% H_2O and has a yield of 65-70 wt% of total product output along with

char and gas as the by-products [Bridgwater et al., 1999]. Even with high yields of liquids, problems with the fast pyrolysis process exist in its energy efficiency and scaling to commercial sizes [Scott et al., 1999]. One of the major disadvantages of these pyrolytic oils include the presence of high content of O_2 and H_2O which makes them low quality fuels compared to regular hydrocarbon fuels. Also, phase separation and polymerization of these bio-oils cause great difficulty in their storage [Brown and Holmgren, 2009]. Some of the companies involved in the commercial production of bio-oil are Dynamotive and New Earth. Fast pyrolysis of biomass and its consecutive upgradation to liquid transportation fuels have several challenges which need to be addressed and only then can this technology achieve a level of commercialization for the transportation fuel industries Wright et al. [2010].

1.1.2 Transesterification of vegetable oils

Oil seed bearing trees are an ideal source of bio-diesel. Some of these trees include palm oil(oil productivity = 3.7t/ha/yr), coconut(oil productivity = 2.2t/ha/yr) and jatropha(oil productivity = 3.7t/ha/yr) amongst many others [Mukunda, 2011]. Oil obtained from these seeds are subjected to the process of transesterification with methanol using NaOH or KOH dissolved in methanol as catalyst, to produce methyl esters of straight chain fatty acids [Pandey and Press, 2009] [Kim et al., 2004]. This process is fairly simple and the properties of bio-diesel obtained are very similar to those of the conventional diesel fuel [Schuchardt et al., 1998]. However, this process requires separation of a large amount of waste water produced and cleaning of catalyst and products [Kim et al., 2004]. On a larger scale, the concern always remains with the the magnitude of energy input required for the production of bio-diesel from vegetable oils. A meaningful way of justifying this issue is by evaluating the energy ratio, defined by the ratio of the energy output of the end product to the fossil energy required for producing this bio-diesel. For the production of bio-diesel from soyabean, this energy ratio is 3-3.5, and for palm oil the ratio is 9-9.5 [Mukunda, 2011] [Pradhan et al., 2009]. This means that palm oil would yield 3 times more energy unit for every unit of fossil energy consumed as compared to soyabean. In order to make overall economics of this process feasible, the by products - protein and glycerine have to be efficiently recovered. Above all, the choice of feedstock

plays a major factor in deciding the profitability of bio-diesel production [Anselm et al., 2011].

1.1.3 Bio-oil from algae

At present a lot of research is being conducted to establish the potential of microalgae for the production of bio-diesel. Surprisingly, oil crops like soyabean, jatropha and palm oil are being used extensively for the production of bio-diesel, but the oil yield per hectare is 10 to 20 times higher for algal bio-diesel, which is an attractive motive for several institutions and industries to invest into the research and development for the production of bio-diesel from microalgae. As an example, the oil palm requires 24% of US cropland for the production of 50% of its transportation fuel, whereas equal contribution to the transportation fuel is provided by algal biomass cultivated over just 1-3% of its total cropland [Chisti, 2007]. Algae contain lipids and saccharides with 2%-40% of lipids/oils by weight [Mukunda, 2011]. The oil fraction in microalgae can be more than 80%, but weight of dry biomass and oil levels are mostly in the range of 20 - 50%. Production of microalgae is generally more expensive than growing oil crops [Chisti, 2007]. Microalgae are grown in open ponds or in photo-bioreactors. Though these ponds are supplied with adequate water, nutrients, CO_2, and are designed for appropriate exposure to sunlight, open ponds are prone to contamination by micro-organisms and extremely dependent on environmental variations(temperature, sunlight) [Achara et al., 2012] [Demirbas, 2011]. Photo-bioreactors provide suitable conditions for algal growth, but are very expensive for large scale production.Some of the constraints being the provision of CO_2 from fossil fuel combustion units at the algae growth sites, supply of nitrogen and phosphorous nutrients and drying of water for the processing of algae [Chisti, 2013]. Above all the best energy ratio for the production of bio-diesel from algae is estimated at 1.4 [Liu et al., 2012].

Rapid growth rate, high energy content, ability to feed on high levels of CO_2 from fossil fuel combustion and the capability of growing algae in low quality water, are some of the key reasons to look towards production of bio-diesel from microalgae, despite the several drawbacks [Achara et al., 2012].

1.1.4 Biomass to liquid (BTL) fuel via Fischer Tropsch

The Fischer Tropsch (FT) process is used for conversion of syngas (a mixture of H_2 & CO) to higher hydrocarbons that primarily consist of liquid fuels and waxes. All the large scale FT plants (liquid fuel production capacity ranging from 10000 to 140000 bpd) are either based on CH_4 reforming or coal gasification systems. Overall schematic of the FT process is described in Fig 1.2. Biomass gasification coupled with FT process plays an assuring and an encouraging option for the production of "green" liquid fuel. Here, biomass is gasified and the bio-syngas generated is used for FT synthesis to produce long chain hydrocarbons that are converted to diesel. FT reaction is catalysed by cobalt or an iron based catalyst utilizing a fixed, fluidized or a slurry bed reactor. The final product, syncrude, which consists of gaseous, organic liquids, aqueous and organic solids, is subject to an upgrading step to transform the product spectrum into more useful products. Primary motive for the installation of FT plants was to produce transportation fuel but, over due course of time, the FT plants have been designed and tuned to produce more profitable chemicals [de Klerk, 2011]. The diesel fraction obtained from FT process has high cetane number, and are generally devoid of sulfur, asphaltenes, and aromatics which are generally present in hydrocarbon products obtained from mineral oil. The choice of catalysts, type of FT reactors and the process conditions used have a wide impact on the nature product spectrum. Though, at present, a lot of focus is being concentrated on BTL via FT process, a significant effort still needs to be put towards the large scale installation of this process.

The following section contributes crucial information from the literature providing FT catalyst properties, process conditions, novel synthesis procedures, FT process coupled to biomass gasification systems and the overall economic scenario for FT based BTL systems.

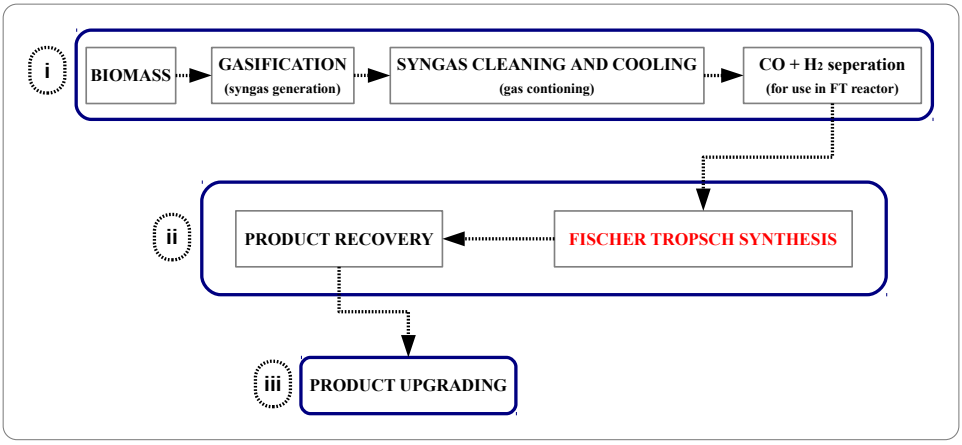

Figure 1.2: BTL schematic
[*(i) Syngas generation and purification unit; (ii) Fischer Tropsch synthesis; (iii) Upgradation of FT crude to desired products*]

1.2 Earlier literature

FT reaction, originally discovered in 1923 by Franz Fischer and Hans Tropsch, involved reaction of synthesis gas over cobalt catalysts resulting in the production of higher hydrocarbons - *gasoline, diesel, middle distillate and heavy waxes*. Considering occasional fluctuations in crude oil availability and its oscillating prices, there has always been a developmental eye for the FT process, which has lead to several large scale industrial establishments. Table 1.1 lists the commercially established FT plants which are functioning even to the current day. The largest FT based plant is based in Qatar with a production capacity of 140000 barrels per day (bpd) which uses natural gas as the feedstock. Table 1.1 evidences that all the commercial plants predominantly operate with natural gas or coal as feedstock. Only remotely stranded natural gas can be subjected to reforming process for the generation of syngas in the gas to liquid (GTL) operation. If the natural gas (NG) obtained from reservoirs can be synced to the NG distribution network, it would be environmentally irresponsible to use this gas for GTL application, since the loss of carbon associated with conversion of NG to another energy carrier cannot be rationalized. Similar to natural gas, coal is converted to syngas via the gasification process. Coal based FT plants are commercially established in South Africa, by Sasol®. Use of coal to generate syngas for FT application can be applied to locations with abundant coal, but lacking other fossil fuels, like India.

Table 1.1: Commercially established FT synthesis plants Guettel et al. [2008]

Company	**Site**	**Capacity [bpd]**	**Raw material**	**Commissioning date**
Sasol	Sasolburg	2500	Coal	1955
Sasol	Secunda	85000	Coal	1980
Sasol	Secunda	85000	Coal	1982
MossGas	Mossel Bay	30000	Natural Gas	1992
Shell	Bintulu	12500	Natural Gas	1993
Sasol/Qatar Petroleum	Qatar	34000	Natural gas	2006
SasolChevron	Escravos	34000	Natural gas	2007
Shell	Qatar	140000	Natural gas	2009

Use of biomass derived syngas for further conversion to liquid fuel is a propitious method for producing environmental friendly fuels. Biomass is the only renewable energy source that is suitable for the sustainable production of carbon based transportation fuel and chemicals.Though several R&D efforts remain focused on the conversion of biomass to liquid transportation fuel, no commercial scale BTL plants exist, like those installed for CTL or GTL. Most of the documented BTL plants are either on demonstration scale or on an experimental stage. The first ever commercial scale BTL plant was instituted by CHOREN industries in Freiberg, German, in 1996. In 2005, its *Beta* plant had a fuel production capacity of 310 barrels per day. The BTL plants which are presently under engineering phase are mostly centred in Europe and USA, as listed in Table 1.2.

Though there are several large scale biomass gasification systems employed for electricity generation and thermal application, it is only recently that research is being concentrated on converting biomass derived syngas to higher hydrocarbons via FT process. The following section briefs about the biomass gasification processes involved

1.2.1 Biomass gasification

Biomass gasification is sub-stoichiometric combustion process where pyrolysis, oxidation and reduction reactions predominate. Eqn.1.1, Eqn.1.2, Eqn.1.3, Eqn.1.4, Eqn.1.5 and Eqn.1.6 describe the overall reactions which occur in a gasifier.

Table 1.2: BTL plant installations

Name	**Location**	**Capacity (bpd)**	**Product**	**Biomass feed**
Green-Sky **Solena fuels**	Essex, UK	1157	Jet fuel	Municipal &, commercial waste
Red Rock Biofuels **Velocys**	Oregon, USA	1100	Gasoline Diesel	Forest & sawmill waste
Sierra BioFuels **Fulkrum Bio-energy**	Nevada, USA	657	Jet fuel Diesel	Municipal solid waste
SYNDIESE **CEA**	Saudron, France	530	Diesel Kerosene Naphtha	Forest & agricultural residue

$$biomass + heat \longrightarrow volatiles + char \tag{1.1}$$

$$volatiles + O_2/Air \longrightarrow CO_2 + H_2O + Heat \tag{1.2}$$

$$C + H_2O \longleftrightarrow H_2 + CO;\ \Delta H = 131.4\, kJ/mol \tag{1.3}$$

$$C + CO_2 \longleftrightarrow 2CO;\ \Delta H = 172.6\, kJ/mol \tag{1.4}$$

$$CO + H_2O \longleftrightarrow CO_2 + H_2;\ \Delta H = -41.2\, kJ/mol \tag{1.5}$$

$$C + 2H_2 \longleftrightarrow CH_4;\ \Delta H = -75\, kJ/mol \tag{1.6}$$

The gasification process conditions such as temperature, gasifying agent and residence time play a crucial role in the syngas composition, overall efficiency and the system performance. Air gasification of biomass, which uses air as a gasifying media, is a prevalent process for syngas generation. The work related to biomass gasification at Indian Institute of Science, Bangalore, has eventuated into an open-top downdraft gasifier design producing gas with low tar concentrations (<2 mg/m^3) and syngas composition (vol.%) of H_2 - 20±2%, CO - 20±2%, CO_2 - 12±1%, CH_4 - 1.5±0.5% and balance N_2 [Dasappa et al., 1989]. Simultaneously, using using steam as gasification medium, water gas reaction (see Eqn.1.3) can be enhanced resulting in higher H_2 concentration in the exit syngas. By varying the steam to biomass ratio (SBR, ratio of H_2O to biomass) and the equivalence ratio (ER, ratio of O_2/biomass), syngas with composition (vol.%): H_2 - 35 to

55%; CO - 10 to 25%; CH_4 - 2 to 5% and CO_2 - 25 to 35% is obtained [Sandeep and Dasappa, 2014].

The Fischer Tropsch reactions require syngas with H_2/CO ratio > 2.1. Steam-oxy gasification of biomass generates syngas which is ideal for FT reactions. For lower H_2/CO ratio, additional reforming reactor is required for increasing the H_2 content to satisfy the FT stoichiometry. Additionally, due to large feedstock variation, significant variation in the syngas composition can be observed, especially with respect to the nature of impurities. Hence, syngas cleaning constitutes a major challenge for the development of BTL process. The gas purification requirement for FT application demands, total sulphur<0.06 mol.ppm, HCN<0.01 mol.ppm, NH_3<0.1 mol.ppm, total halides<0.01 mol.ppm and alkalis<0.01 mol.ppm. Hetero-elements and some inorganic compounds present in the biomass generated syngas affect the BTL process by poisoning the FT catalysts and consequently affecting the overall conversion and product selectivity. Chlorine, fluorine, and bromine containing compounds are highly water soluble and can be eliminated in water cleaning units. Sulphur containing compounds which easily poison the FT catalysts, can be effectively stripped, along with CO_2, using acid gas removal processes. The removal of trace contaminants, from the acid-gas treatment gas-stream, is achieved using processes based on physisorption, chemisorption, or chemical reaction over solid carrier bed [Chiche et al., 2013]. The synthesis gas also must contain very low tar and particulate matter. The tar and particulate matter removal system of the open top downdraft gasifier developed at Indian Institute of Science consists of cyclone separators, specially designed scrubbers, an additional chilled scrubber and a final fabric filter section to remove matter less than 5μ. The cleaned gas has tar concentrations of 3 mg/Nm^3, which is within acceptable limits for FT process. Overall, the syngas purification system should effectively reduce impurities to levels which minimize the catalyst poisoning and has no deteriorating impact on the overall conversion and product yields.

1.2.2 Fischer-Tropsch chemistry

FT chemistry is often regarded as the vital technological input for converting syngas to a range of hydrocarbons, which are further hydrocracked into liquid transportation fuels and other chemicals. The FT reaction is catalysed

most effectively by iron and cobalt at pressures ranging from 1 MPa to 6 MPa and temperatures ranging from 463 K to 623 K. The formation of primary FT products, viz., paraffins and olefins are described in Eqn.1.7 and Eqn.1.8. In case of both the reactions, H_2O is the prevailing oxygenated FT product. The water-gas shift reaction which has been described earlier in Eqn.1.5, has a severe effect on the FT stoichiometry, directly affecting the reaction rates. With cobalt catalysed FT reaction, the WGS activity is negligible, and this reaction can be considered as a non-reversible reaction resulting in the formation of minimum concentrations of CO_2. However, in case of iron catalysed FT process, the WGS reaction approaches equilibrium at temperatures in the range of 523-573 K and, under these conditions CO_2 is treated as a reactant along with H_2 and CO. Over Fe catalysts, WGS reaction occurs synchronously with FT reaction, subsequently making it possible to use syngas with H_2/CO ratio less than 2.1. Consequently, for cobalt catalysts, which have low WGS activity, the ratio of consumption of H_2 and CO is between 2.06 and 2.16. Alcohols are also produced in small quantities as side reactions, during the FT process (Eqn.1.9)

$$(2n+1)H_2 + nCO \longrightarrow C_nH_{2n+2} + nH_2O \tag{1.7}$$

$$2nH_2 + nCO \longrightarrow C_nH_{2n} + nH_2O \tag{1.8}$$

$$2nH_2 + nCO \longrightarrow C_nH_{2n+2}O + (n-1)H_2O \tag{1.9}$$

FT synthesis yields a wide range of hydrocarbon products. Like conventional crude oil, the products of FT synthesis does not refer to a single product, but a mixture of straight chain, branched and oxygenated hydrocarbons. The product spectrum is a direct function of the catalyst and reaction conditions. The FT product mostly comprises of four phases - gaseous hydrocarbons, organic liquid, aqueous liquid and organic solids. The separation and refining of this syncrude results in the conversion of FT products into useful components. The overall value addition to the final FT product is attained only after the refining process.

1.2.2.1 FT reaction mechanisms

The FT reaction, is a surface polymerization reaction, where the reactants, CO and H_2, adsorb and dissociate on the catalyst surface. The dissociated molecules

alternatively combine to form a chain initiator specie, moulding the reaction to proceed by chain propagation, chain termination and product desorption. This type of product distribution has been explained using step-by-step addition of CH_2 monomers into the growing chain, as shown in Eqn.1.10.

$$2nH_2 + nCO \longrightarrow -(CH_2) -_n + nH_2O \tag{1.10}$$

Three distinct reactions have been identified explaining the formation of FT products from the surface species, viz., chain intitation, chain propagation and chain termination. *Chain* here refers to the length of the higher hydrocarbon FT products. The formation of chain starter monomer unit corresponds to the initiation reaction, while propagation refers to the insertion of the monomer units to the growing chain. Termination reaction is the desorption of growing chains from the catalyst surface [Steynberg and Dry, 2004]. Based on the initiation, propagation and termination steps, FT reaction mechanisms have been proposed which broadly explain the nature of the hydrocarbon product spectrum. Four mechanisms have been developed to capably anticipate the product distribution - *alkyl, alkenyl, enol and CO-insertion* mechanism. Each of these reaction mechanism vary from the other with respect to the monomer specie formed and the chain initiator molecule.

In the *alkyl mechanism*, which is the most widely accepted mechanism, CH_2 is the building block and CH_3 specie is the chain initiator. The hydrocarbon chain growth is achieved by successive addition of CH_2 species to the alkyl molecule and chain termination occurs by β-hydride elimination yielding α-olefins or by hydrogen addition yielding n-paraffins. Similar to alkyl mechanism, the *alkenyl mechanism* has CH_2 as the monomer unit. However, reaction initiation occurs by generation of surface vinyl species (-CH=CH_2). The chain further develops by incorporation of CH_2 species to the vinyl species resulting in the formation of surface allyl species (CH_2-CH=CH_2). Subsequent isomerization reaction results in the formation of alkenyl species (-CH=$CHCH_3$). Chain termination occurs by hydrogen addition yielding α-olefins. In the *enol mechanism*, the chain initiator as well as the main monomer is the $=CHOH$ specie, formed by the hydrogenation of chemisorbed CO. The chain growth occurs via the dual reaction comprising condensation reaction between enol species and the dehydration reaction. This

mechanism effectively postulates the formation of branched hydrocarbons. The *CO insertion mechanism* considers chemisorbed CO as the monomer unit and the surface methyl (-CH_3) as the chain initiator. Propagation occurs by the resulting conjugation of the CO monomer to the -CH_3 specie and subsequent hydrogenation and de-oxygenation step, generating alkyl species. The chain termination step in this mechanism occurs identical to the alkyl mechanism. This mechanism also estimates the formation of aldehydes and alcohols due to the presence of oxygenated species. Table 1.3 summarizes the four Fischer-Tropsch reaction mechanisms. Investigative study reported by Davis [2001] concluded that oxygenate mechanism similar to enol mechanism is ideal for iron based catalysts. While, surface carbide mechanism is an ideal choice for cobalt based catalysts to adequately predict the FT product distribution. Gaube and Klein [2008] effectively postulated a modified alkyl mechanism coupled with the CO insertion mechanism to interpret the effect of cobalt and iron catalysts.

Table 1.3: Summarizing FT mechanism

Mechanism	**Monomer**	**Initiatior**	**Products**	**Remarks**
Alkyl	$\models CH_2$	$\vdash CH_3$	α-olefins, n-paraffins	Inadequate to account formation of branched HC and oxygenates
Akenyl	$\models CH_2$	$\vdash CH{=}CH_2$	α-olefins	Only explains formation of α-olefins as primary products
Enol	$\models C\begin{smallmatrix}H\\OH\end{smallmatrix}$	$\models C\begin{smallmatrix}CH_3\\OH\end{smallmatrix}$	aldehydes alcohols α-olefins	Unable to explain formation of n-paraffins
CO-insertion	$\models CO$	$\vdash CH_3$	α-olefin n-paraffin aldehyde alcohol	Primary pathway for formation of oxygenated FT compounds

Considering the well established fact that FT reactions yield predominantly aliphatic hydrocarbons, the analyses of the product distribution show that the nature of product spectrum follow the Anderson-Schulz-Flory (ASF) statistics.

Eqn.1.11 describes the ASF equation. Here, w_n is the weight fraction of the product with carbon number n, and α is the probability of chain growth. Higher α values indicate the formation of longer chain hydrocarbons.

$$log(\frac{w_n}{n}) = n\ log(\alpha) + log(\frac{(1-\alpha)^2}{\alpha}) \tag{1.11}$$

A plot of $\log(x_n)$ against the carbon number n, is shown in Fig 1.3. Descriptions of these nature are called ASF plots and are used to characterize FT product spectrum. This distribution suggests that chain propagation and termination result with probabilities which are almost independent of chain length. Fig 1.4 shows hydrocarbon selectivity as a function of the chain growth probability factor, α. Higher alpha values indicate higher selectivity for longer chain hydrocarbons, and chain growth probability of zero implies production of methane with 100% selectivity - methanation. The FT reaction can only proceed when this thermodynamically favoured methanation reaction is suppressed, eventually leading to the formation of higher hydrocarbons. From Fig 1.4 it can be observed that the maximum yield of middle-distillate (C_{10}-C_{20}) yield is ∼40 wt.%, obtained at α=0.85. For, higher production of C_{10}-C_{20} hydrocarbons, the FT process must be operated with α=0.95, so that the wax can then be hydrocracked to middle-distillate hydrocarbons.

The chain growth probability factor, α, is directly dependent on the choice of catalysts and the FT operating conditions (temperature, pressure, bed residence time, superficial velocity, H_2/CO ratio). Within a certain limits, α can be tuned by adjusting these parameters. Low temperature (453 K - 503 K) results in high α value ranging from 0.92 to 0.95, whereas at high operating temperature (573 K - 623 K), α ranges from 0.7 - 0.8. The syngas feed ratio (H_2/CO) has a drastic effect on α. Higher H_2 partial pressure, increases the rate of H_2 termination step compared to the chain propagation step resulting in the formation of lower chain hydrocarbons, indicating reduced chain growth probability. The effect of bed residence time has a direct consequence on the rate of product re-adsorption, affecting the extent of secondary reactions. Therefore, on increasing the space velocity, the FT products invest reduced time on the catalyst surface resulting in lower probability of re-adsorption and consequently reducing the degree of secondary reactions. This results in the formation of larger concentrations of

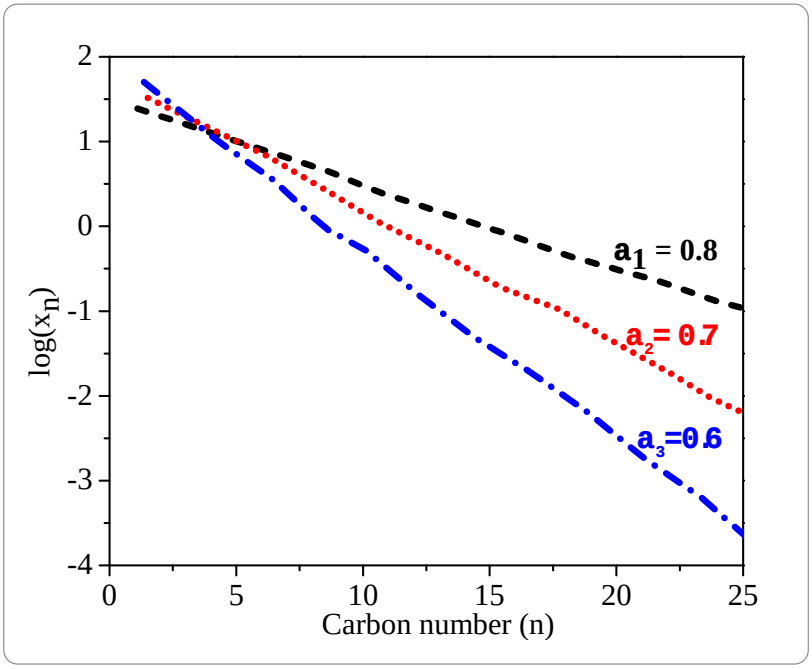

Figure 1.3: Logarithmic molar product distribution as a function of carbon number, for α=0.8, 0.7 and 0.6 [Steynberg and Dry, 2004]

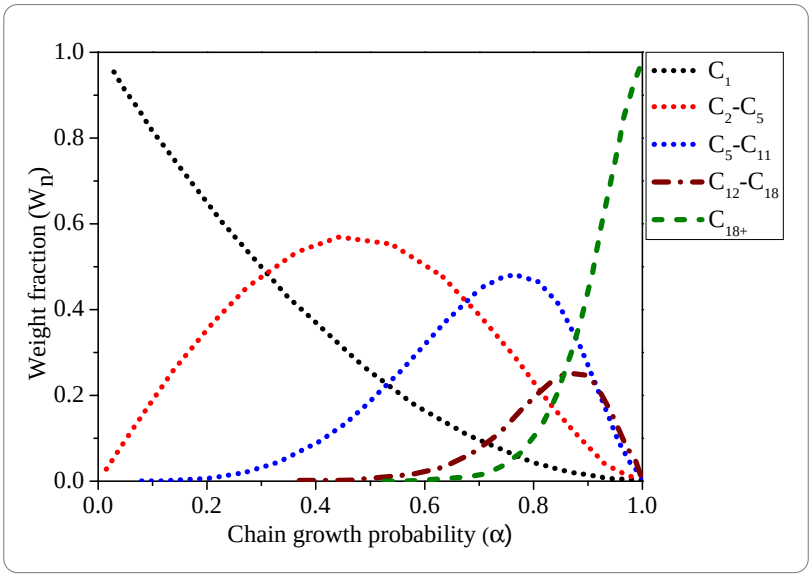

Figure 1.4: FT product composition as a function of α

branched hydrocarbons. Table 1.4 lists the operating alpha of commercial FT plants. It is evident from this table that the α values are selected from one of the two regimes: Regime-I (α = 0.7-0.8) or Regime-II (α = 0.9-0.95). The choice

of α is exclusively dependent on the nature of product spectrum desired from the FT plant. If gasoline and diesel (C_{10}-C_{20}) are the choice of product spectrum desired, the catalyst and the process conditions must be optimized to yield α in the range of 0.8-0.85. However, for higher wax production, the α must range from 0.9-0.95.

Table 1.4: Chain growth probability factor (α) for commercially operating FT plants

Plant	**Reactor**	**Catalyst**	α
Sasol 1 - Kellogg Synthol process	Circulating fluidized bed (CFB) T = 563-613 K; P = 2.2 MPa	Fused Fe	$<$ **0.7**
Arge LTFT synthesis	Multi-tubular fixed bed T = 473-523 K; P = 2.5-2.7 MPa	Precipitated Fe	**0.90**
Sasol slurry bed process (SSBP)	Catalyst suspended in liquid wax T = 518 K; P = 2.1 MPa	Precipitated Fe	**0.95**
Sasol Advanced Synthol (SAS)	Fixed fluidized bed T = 583-623 K; P = 2.5 MPa	Fused Fe	**0.7-0.8**
Mossgass facility	Circulating fluidized bed (CFB) T = 603-633 K; P = 2.5 MPa	Fused Fe	**0.7-0.8**
Shell middle distillate synthesis (SMDS)	Multi-tubular fixed bed T = 493 K; P = 2.5 MPa	Co based	**0.90-0.92**
Oryx-GTL facility	Sasol slurry phase distillate T = 503 K; P = 2.0-2.5 MPa	$Co/Pt/Al_2O_3$	**0.90-0.92**

1.2.2.2 FT reactors

Primary aim of any FT reactor is to remove the large heat of reaction resulting from the FT reaction and maintain isothermal conditions across the catalyst bed. Modern FT reactors are broadly categorized on the basis of their two operating temperatures, viz., low temperature Fischer Tropsch reactor (LTFT; operating temperature in the range of 473 - 503 K), and high temperature Fischer Tropsch reactor (HTFT; operating temperature in the range of 573 - 623 K). HTFT reactors utilize iron catalysts with product spectrum largely comprising of middle distillates and gasoline fractions, while LTFT reactors utilize mostly cobalt catalysts, yielding longer chain hydrocarbons and waxes.

The most common type of LTFT reactor is the multi-tubular fixed bed reactor with catalysts placed in the tubes and cooling medium in the shell side.

Short span between the catalyst particles and the tube walls and high gas linear velocities, significantly intensifies the heat transfer from the catalyst particles to the cooling medium, maintaining steady FT temperature range. Syngas recycling aids in improved heat transfer and also increases the overall conversion. Similarly, recycling of liquid hydrocarbon products also enhances the temperature profile in the fixed bed reactors [Steynberg et al., 2004]. The advantages of a multi tubular fixed bed reactors include easy handling and maintenance and, easy product separation, since the heavy wax products trickle down the bed and are collected in the receiver pot. Most importantly, the performance and the behaviour of large scale plants can be predicted accurately based on the performance of pilot scale plants. The major disadvantage of using fixed bed reactors arises from the constraints related to catalyst particle size. To overcome the pressure drop resistance in a fixed bed reactor, larger catalyst particles need to be employed. However, intra-particle diffusion plays a limiting factor for the overall reaction rates with particle sizes greater than 1 mm. Catalyst particle size and reactor diameter tend to be crucial parameters for a fixed bed FT process.

A detailed simulation work reported by Jess and Kern [2012] demonstrated the influence of catalyst particle size on the pressure drop across the catalyst bed and the overall heat transfer coefficient from the catalyst bed to the reactor wall for varying reactor diameter. Fig 1.5 shows the variation in the pressure drop for a 40 mm diameter and 12 m long fixed bed FT reactor. For a particle size below 1 mm diameter, the reactor operations suffer from huge pressure drop that would consequentially lead to varying reaction rates across the reactor length resulting in decreased overall conversion and the product spectrum to shift to lower hydrocarbon range. Moreover, the total energy to compress syngas for FT reaction increases proportionally. Furthermore, the catalyst particle size also influences the overall thermal transmittance ($U_{overall}$) of a wall cooled tubular reactor, as shown in Fig 1.6. For a 20 mm diameter reactor tube, the $U_{overall}$ increases from 375 W/(m^2K) to 425 W/(m^2K) as the particle size increases from 1 mm to 6 mm. Industrially, the wall cooled multi-tubular fixed bed FT reactors utilize catalyst particles with sizes $\sim$ 2 mm in a 50 mm diameter reactor to limit the pressure drop constraints and maximize the overall heat transfer coefficients.

Another type of LTFT reactor is the slurry phase bubble column reactors. Catalyst particles of sizes 10 to 200 μm are suspended in a hydrocarbon solvent.

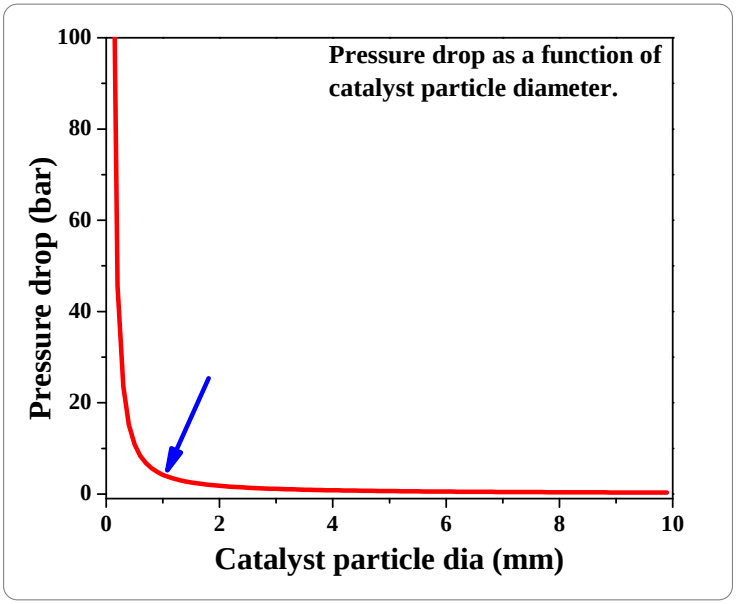

Figure 1.5: Variation in the pressure drop with varying catalyst particle size in a fixed bed FT reactor

[*Data extracted from Jess and Kern [2012]*]

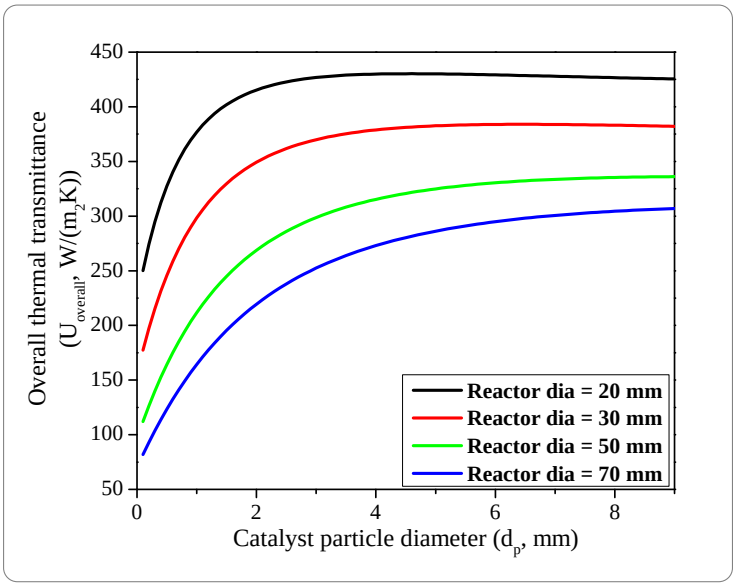

Figure 1.6: Variation in the overall thermal transmittance from the catalyst bed to the reactor wall with varying catalyst particle size

[*Data extracted from Jess and Kern [2012]*]

As a result of small catalyst particle sizes, the effect of internal mass transfer resistances are negligible resulting in optimal activity and selectivity. Above all,

the efficient heat removal system enables maintaining isothermal catalyst bed operations. Due to improved syngas utilization by the catalyst particles, the productivity in a slurry bubble column reactor is higher than in a fixed bed reactor. However, the impediment to separation of catalyst particles from the FT products results in considerable catalyst losses and has restricted wide use in commercial FT processes [Krishna and Sie, 2000].

The high temperature FT processes, which operate in the range of 573 - 623 K, utilize Fe based catalysts generating mostly, gasoline or linear olefins. The high temperatures cause all the FT products within the reactor to be in gaseous phase. The two types of reactors utilizing high temperature processes are fixed fluidized bed (FFB) and, circulating fluidized bed (CFB) reactors. The Sasol Advanced Synthol (SAS) reactor commissioned at Secunda, South Africa, employs the fixed fluidized bed technology. The syngas is introduced from the bottom and the flow rate controlled to create a fluidized bed. The catalyst particles which are carried over by the exit product gases are separated in cyclone separators and re-circulated back to the fluidized bed. Though high syngas utilization are effectively achieved, the product separation from the catalyst traces is a major challenge, resulting in considerable catalyst losses during the operational period. Fig 1.7 shows three types of commonly employed commercial FT reactors

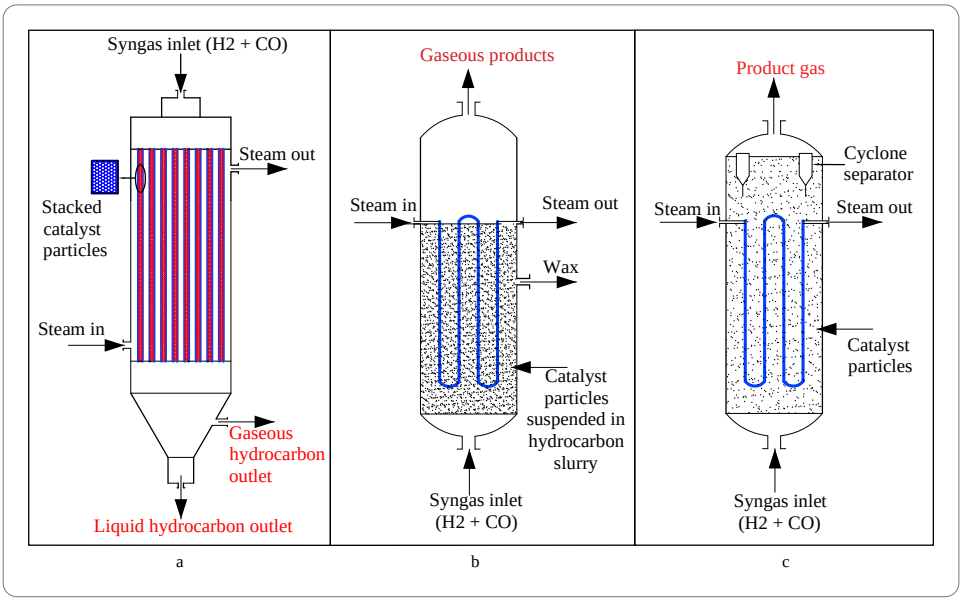

Figure 1.7: a.Multi-tubular fixed bed reactor; b.Slurry phase reactor; c.Fixed fluidized bed reactor

1.2.3 FT catalysts

FT catalysts must possess efficient activity, selectivity, stability and regeneration properties. For these reasons, iron and cobalt are the most widely used Fischer Tropsch catalysts, particularly for its high CO hydrogenation activity and high selectivity to higher hydrocarbons. Both Fe and Co catalysts are used in their metallic form, rather than their native oxide states. Therefore the metal oxide catalysts are subjected to a reduction process for use in FT reaction. Catalysts are dispersed on high surface area catalyst carriers or supports to increase the overall metal surface area available for reactants. Several supports like SiO_2, Al_2O_3, TiO_2, aluminosilicate and carbon nanotubes have been used as active support materials in FT processes.

1.2.3.1 Iron based FT catalysts

Iron catalysts have been the most common FT catalysts, owing to its low relative costs and wide availability. Iron oxide crystallites with sizes in the range of 10 nm to 50 nm, present in the from of haematite or magnetite, comprise the FT synthesis catalyst precursor. Iron oxide in the form of Fe_3O_4 catalyses the water-gas-shift reaction and is considered to be the primary phase accountable for elevated water gas shift activity of the iron based catalyst. The WGS and FT reaction are known to occur on different active sites of the iron based FT catalyst. During the prevailing reaction conditions, Fe catalyst can exist in the form of magnetite, α-Fe, or in the form of Fe-carbide. Existence of these phases during the FT reaction, have a direct consequence on the FT product distribution. The active phase of iron catalyst for the Fischer Tropsch reaction has been a subject of discussion for some time with reports detailing either iron carbide or zero-valent iron or even Fe_3O_4 to be the active FT phase [Bukur et al., 1995] [Davis, 2003]. Schulz et al. [2005] claimed that the active Fe catalyst for FT synthesis is "constructed" in several stages of "self-organization", during which conversion, selectivity, catalyst composition and structure change, concluding that Fe in its zero valent state is not the active phase. FT activity develops when iron carbide are formed. Essentially, it is necessary to reduce the Fe catalyst prior to use in the FT reactor. The need to reduce the catalyst is to develop catalysts with high active surface areas. Extent of reduction and method of reduction intensely

influences the FT selectivity. Reduction with H_2 at 573 K produces more active catalysts than reduction with syngas at the same temperature. However, the catalyst reduced with H_2 has a lower wax selectivity. Fe catalyst can be activated by reducing in an environment containing CO, syngas or H_2. Reduced activity is observed for catalysts pre-treated in syngas as compared to the catalysts that are pre-treated in CO.

Use of Fe catalysts produce broad range of hydrocarbon products including paraffins and olefins. The products vary from fractions of methane to high molecular weight waxes. Fe catalysts show varying WGS activities, and in some cases leading to rejection of 30% to 50% carbon feed as CO_2. α-olefins are the primary products formed over iron catalysts. However, olefins can undergo secondary reactions resulting in isomerization or hydrogenation. In the work reported by Soled et al. [1990], the hydrocarbon selectivity over Fe_2O_3 catalysts showed secondary product formation. It was reported that the Fe_2O_3 catalysts inhibited the chain growth probability and reduced the C_{5+} selectivity. Contrary to Fe_2O_3 catalysts, the Fe_5C_2 catalysts produced more olefinic products and higher concentrations of heavier hydrocarbons.

1.2.3.2 Cobalt based FT catalysts

Cobalt catalysts, though expensive compared to iron catalysts, are more resistant to deactivation by sintering and oxidation. At low CO conversions (χ_{CO}=30 - 40%), the activity of both the metals are comparable. However, at high CO conversions (χ_{CO}=60 - 70%), the productivity of higher hydrocarbons is more significant in cobalt catalysts. This is attributed to reduced reaction rates of Fe catalysts, due to high water concentrations. The water gas shift reaction (Eqn.1.5) is more significant on Fe catalysts than on Co catalysts. The hydrocarbon yield with Fe catalysts primarily include branched compounds (α-olefins) and oxygenates, while Co catalysts chiefly yield n-paraffins. A striking feature of Fe catalysts, is its use under wide range of process conditions. Fe catalysts yield FT products under varying pressure ranges (1.0 - 6.0 MPa), LTFT and HTFT reactors, and varying H_2/CO ratios (0.5 - 2.5). Contrastingly, Co catalysts can be used only under narrow operating ranges - H_2/CO feed ratio in the range of 2.0 to 2.2 and low operating temperature (453 - 503 K), since high temperature leads

to drastic increase in the CH_4 concentrations and also causes fouling of catalysts by carbide formation. Unlike iron carbide in iron based catalysts, the metallic form of cobalt are desirable for FT reaction. The supported Co_3O_4 precursors are reduced to Co^0 by reduction in flowing H_2, at elevated temperatures (773 K - 873 K). The reducibility of cobalt catalysts is dependent on several factors such as the Co_3O_4 crystallite size, temperature of reduction and the extent of metal support interaction. It is observed that for large cobalt metal particles the rate of FT reaction is directly proportional to the fraction of active cobalt metal sites present on the catalyst surface. Fig 1.8 shows linear variation in the rate of conversion per unit time with increasing fraction of active metal sites. However, in case of smaller cobalt crystallite sizes (< 7 nm), it has been observed that this relation is not valid since smaller crystallite sizes form different cobalt metal phases, which are not active for FT reaction [Khodakov et al., 2007].

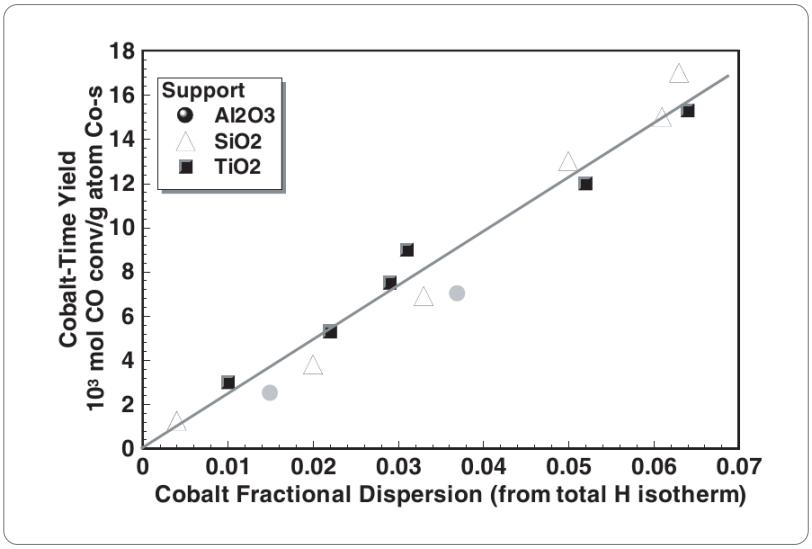

Figure 1.8: Site-time yield for cobalt catalysts supported on SiO_2 , Al_2O_3 and TiO_2 as a function of fractional metal dispersion. FT conditions : P = 2 MPa; T = 473 K

[*Image extracted from Soled et al. [2003]*]

The primary products from FT synthesis include n-paraffins with higher concentrations of heavier waxes. Since cobalt catalysts are used only at temperatures in the range of 453 - 503 K, the ASF distribution dictates the product spectrum with α in the range of 0.85 to 0.95. Despite the narrow operating ranges, supported cobalt metal are active choice of catalysts for FT reactions due to high catalyst stability, high single pass conversion and superior hydrocarbon produc-

Table 1.5: Comparison of cobalt and iron FT catalysts

Parameter	**Co Catalyst**	**Fe catalyst**
Operating Temperature	453 - 503 K. Used only in LTFT reactors. Elevated temperatures result in excessive CH_4 formation & also results in catalyst coking.	473 - 623 K. Operates both in HTFT and LTFT reactors
Feed gas	Syngas with H_2:CO ratio in the range of 2.0-2.3, due to low WGS activity	Flexible H_2:CO ratio in the range 0.5-2.5, due to high WGS activity
Activity	More active at higher CO conversions i.e., lower space velocities	Lower activity compared to cobalt catalysts
Product spectrum	Primary products are n-paraffins with marginal production of α-olefins. Higher paraffin/olefin ratio. α=0.85-0.92	Primary products are n-paraffins with considerable production of α-olefins. Lower paraffin/olefin ratio. α=0.65-0.92
Promoters	Noble metals (Ru, Rh, Pt, Pd); Oxide promoters (ZrO_2, La_2O_3, CeO_2)	Alkali metals (Li, Na, K, Rb, Ca)
Life & cost	Longer life time, more expensive	Lower life time, less expensive

tivity compared to Fe catalysts. Table 1.5 summarizes the comparison of iron and cobalt based catalysts.

1.2.4 Catalyst parameters

The structural properties of the synthesized catalysts have a direct impact on the FT activity and hydrocarbon selectivity. The literature indicates several investigations on the effect of metal crystallite size, reduction degree and metal dispersion on the overall FT activity. Overall, the synthesized cobalt catalysts should possess high surface area, high degree of metal reduction, high cobalt site density (>10 wt.%) and metal dispersion in the range of 15% - 20%. Consequently, the catalysts are dispersed over catalyst carriers like Al_2O_3, SiO_2 and TiO_2 to increase the metal surface area and also to enhance the mechanical integrity of the synthesized catalysts. Eventually, the catalysts must contribute towards high C_{5+} selectivity, low CH_4 selectivity and high hydrocarbon yield per

unit mass of syngas.

The following sections discuss the impact of critical physical properties of cobalt catalysts on the Fischer Tropsch activity. A detailed and methodical understanding of these parameters aid in designing highly active cobalt catalysts which would eventually result in outstanding syngas to liquid fuel conversion efficiencies.

1.2.4.1 Metal loading

Several researchers have investigated the impact of metal loading on the FT activity. Wang and Chen [1991] demonstrated over Co/γ-Al_2O_3 catalysts that, with increasing metal loading, the extent of metal reduction increased. An increase in the extent of reduction was primarily attributed to variation in the nature of cobalt species formed on the support surface. For high metal loading catalysts, considerable fraction of cobalt oxide are present as Co_3O_4 , which are easily reducible to metallic cobalt. Lower metal loadings result in the generation of amorphous surface cobalt aluminates, formed by the diffusion of cobalt ions into the first few outer layers of the aluminate lattice sites. Under conventional reduction temperature ranges (673 K - 973 K), cobalt aluminates are irreducible and contribute towards the formation of inactive FT catalysts. Fig 1.9 shows the effect of cobalt loading on the degree of reduction and rate of CO consumption. The trend shows an increase in reduction degree and a resultant increase in the FT activity, with increasing cobalt loading. Jacobs et al. [2002], similarly reported a reduction in the metal support interaction by increasing the cobalt loading from 15% to 33%. Here, the authors attributed the reduction in metal support interaction to the increased Co crystallite size which facilitated the reduction of Co_3O_4 to Co^0.

The metal catalysts being fairly expensive, their maximum utilization has to be ensured. In case of the FT reaction, a lower metal loading ($<$ 10 wt.%) results in the fraction of deposited caobalt oxides to be in the form of stable, irreducible cobalt-support oxide compounds, which are inactive towards FT reaction. For loading above 25 - 30 wt.% no additional increase in the FT activity is observed. An ideal catalyst for FT reaction must have cobalt loading in the range of 20-25 wt.%, enabling maximum utilization and effective overall syngas conversion.

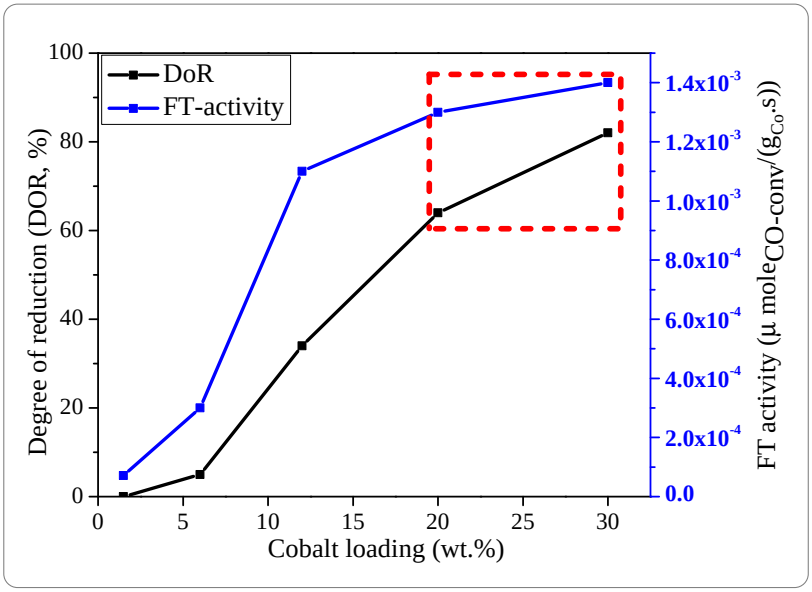

Figure 1.9: Variation in cobalt reduction temperature and the FT activity with varying metal loading

[*Data extracted from Wang and Chen [1991]*]

1.2.4.2 Impact of cobalt crystallite size

The influence of cobalt particle size on the FT activity was demonstrated by Bezemer et al. [2006] for carbon nanofiber supported cobalt catalysts with varying cobalt particle sizes in the range of 16 nm - 2.6 nm. The experiments showed that the turnover frequency (TOF) for CO hydrogenation was independent for cobalt catalysts having particle sizes larger than 8 nm. Above all, the C_{5+} selectivity decreased from 85 wt.% to 5 wt.% when the cobalt particle size reduced from 16 nm to 2.6 nm. The experiments clearly demonstrated that the minimum cobalt particle size for FT reaction is greater than 8nm. The TOF stabilized at a constant value above 6 nm while the maximum C_{5+} selectivity was observed for Co catalysts with particle size above 12 nm. The authors here suggest that the primary reason for reduced activity of catalysts with smaller particle size is attributed to larger rates of deactivation by oxidation and carbide formation, under the prevailing FT conditions. However, this reasoning is rather inadequate, since the smaller size cobalt particles also tend to form cobalt aluminates which have absolutely no activity for FT reactions. Conclusively, larger size particles (>8 nm) are adequate enough to create optimal FT active sites. Jacobs et al. [2002] in their work reported a sharp decrease in the extent of metal reduction

below 10 nm cobalt crystallite size. Fig 1.10 shows the effect of Co particle size on the reduction degree, TOF and C_{5+} selectivity. This clearly indicates the FT ineffectiveness of the smaller crystallite sized cobalt catalysts.

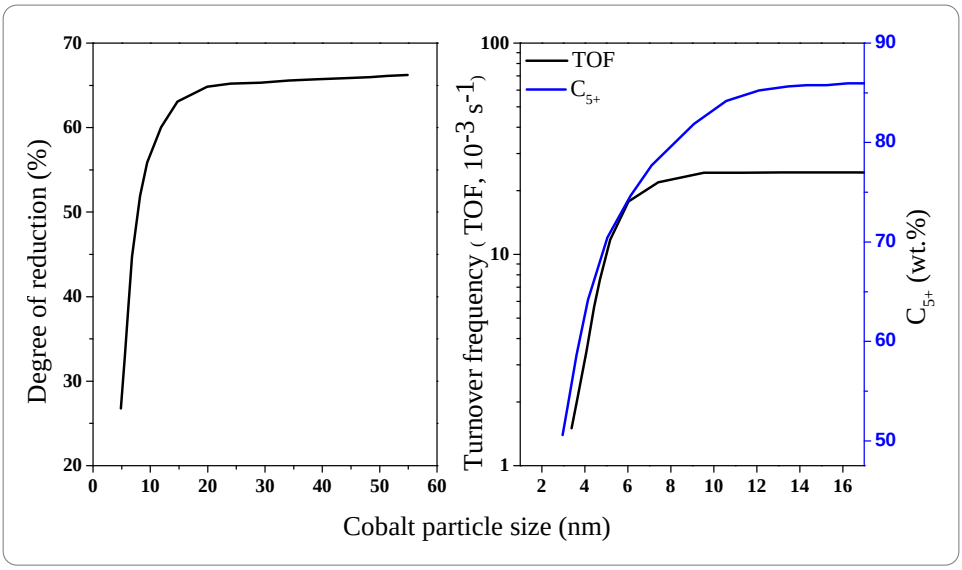

Figure 1.10: Effect of varying cobalt particle size on the reduction degree, TOF and C_{5+} selectivity
[*Data extracted from Bezemer et al. [2006] and Jacobs et al. [2002]*]

The calcination temperature has a direct impact on the cobalt crystallite size. Kababji et al. [2009] reported sintering and agglomeration of the cobalt crystallites at higher calcination temperatures, gradually decreasing the cobalt active surface area and resulting in lower FT activity. Fig 1.11 shows the effect of calcination temperature on the FT activity and selectivity. Similarly, Borg et al. [2007] reported an increasing Co crystallite size with increasing calcination temperature. The cobalt crystallite size increased from 10 nm to 11.5 nm, with an increase in the calcination temperature from 523 K to 573 K. The cobalt dispersion, at the same time, decreased from 8.2% to 7.5% clearly indicating a reduced FT activity. Higher calcination temperature is required for complete decomposition of the cobalt precursor (eg. cobalt nitrate hexahydrate) in the catalyst synthesis step, but it is crucial to maintain lower calcination temperature for higher metal dispersion, by reducing the amount of sintering. A compromise between the two is necessary for synthesizing an active high dispersion FT catalyst.

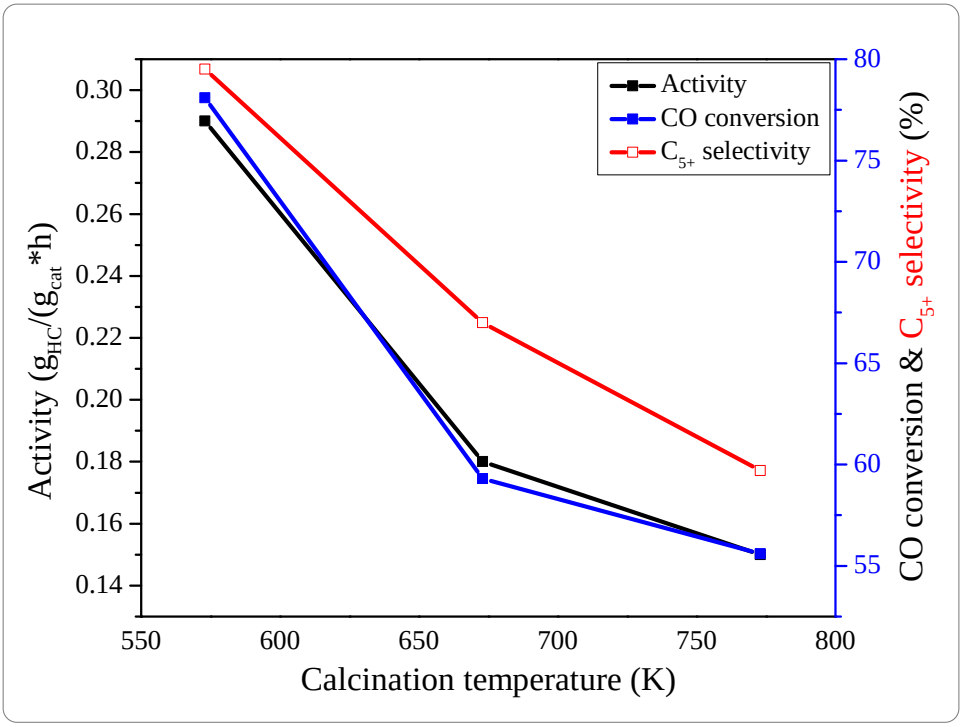

Figure 1.11: Effect of calcination temperature on the overall FT activity [*Data extracted from Kababji et al. [2009]*]

1.2.4.3 Influence of support on FT activity

The choice of FT supports have a broad impact on the FT activity and selectivity. Though the central function of catalyst support is simply of *physical nature*, i.e., to increase the amount of metal surface area available for the reactants, very often the dispersed metals show a strong affinity for the support, which influences the FT performance. In most cases, the support and the deposited metal show specific interaction which affect the extent of reduction, metal dispersion and, therefore, the overall FT activity. The strength of metal support interaction has a direct influence on the degree of cobalt reduction. The most commonly used supports for FT reaction are Al_2O_3, SiO_2 and TiO_2. Based on the metal support interaction, the degree of reduction increases in the following order : $Al_2O_3 < SiO_2 < TiO_2$. A strong interaction between the support and cobalt nano-particles exist on γ-Al_2O_3 supports, resulting in lower degree of Co_3O_4 reduction. For cobalt-alumina system, the formation of cobalt aluminate species over Al_2O_3 supports reduce the available active sites for FT synthesis. Apart from the formation of bulk aluminates over Al_2O_3 supports, the degree

of reduction, and hence the metal dispersion, reduces due to the formation of $Co^{2+}Co^{3+}_{2-x}Al_xO_4$ mixed spinels, additionally reducing the FT activity. Fig 1.12 shows the effect of support on the degree of reduction and the overall FT activity. Compared to Al_2O_3, the SiO_2 supported cobalt catalyst show higher activity, which is attributed to higher degree of metal reduction resulting from the lower metal-support activity. The temperature programmed reduction investigation of Al_2O_3 supported cobalt oxide by Arnoldy and Moulijn [1985] presents detailed insight into the various oxidation states of cobalt, which arise during the reduction process. According to Arnoldy and Moulijn [1985], four stages of alumina supported cobalt oxide reduction are observed, assigned to the four cobalt phases that reduce at different temperatures. Ideally, lower reduction temperatures (750 - 900 K) are preferred to prevent sintering and agglomeration of the cobalt crystals. However despite this drawback, alumina supported catalysts have been used widely to produce longer chain unbranched hydrocarbons primarily due to its low surface acidity and also owing to its higher site time yield.

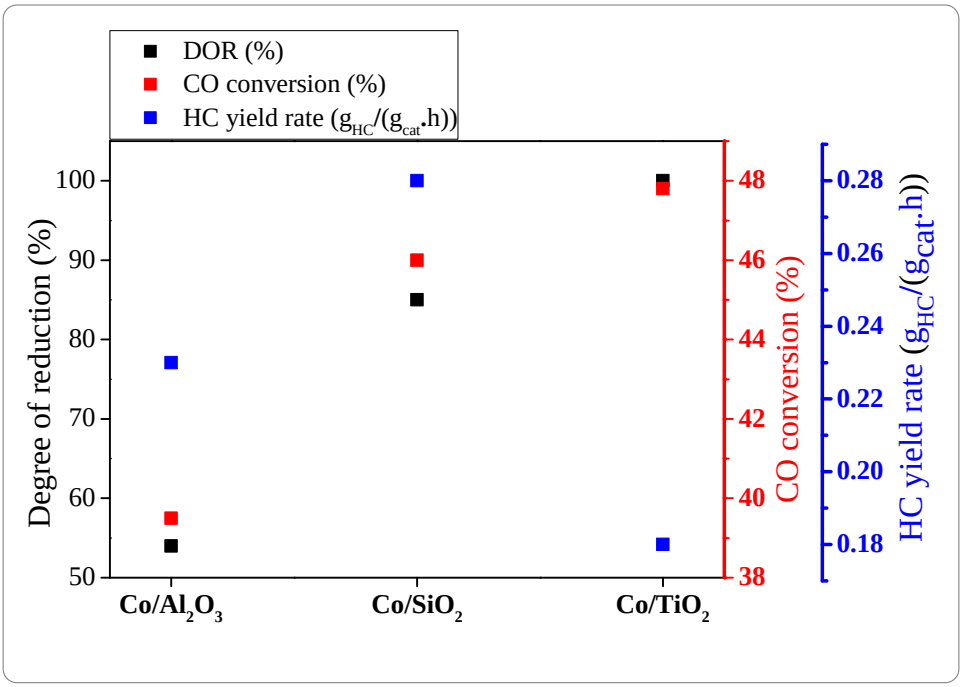

Figure 1.12: Effect of support on the extent of cobalt reduction and the FT activity [*Data extracted from Storsæter et al. [2005]. FT conditions: P = 2 MPa; T = 483 K*]

Jean-Marie et al. [2009] synthesized cobalt catalysts supported on silica-doped-alumina (SDA). The effectiveness of the silica doping into the Al_2O_3 sup-

ports were tested by comparing the extent of metal reduction and the FT activity with Al_2O_3 supported cobalt catalysts. Remarkably, the cobalt oxides reduced to metallic cobalt at 973 K for SDA supported catalysts compared to a reduction temperature of 1200 K for alumina supported catalysts. The authors in this work reported that the SiO_2 doping of Al_2O_3 support reduced the basicity of the synthesized catalysts, which hindered the formation of hardly reducible cobalt aluminates, thereby increasing the degree of reduction. A detailed study on the impact of SiO_2 doping of Al_2O_3 was conducted by Daniell et al. [2000]. In this work a series of SDA supports were synthesized by varying the SiO_2 doping from 1.6 wt.% to 90 wt.%. The doping resulted in the formation of highly acidic Lewis and Brösted acid sites. The strength and the magnitude of these sites reached a maximum for 40% SiO_2 doping, above which the sample resembled pure SiO_2.

Besides degree of metal reduction, the constitution of FT product spectrum is direct impacted by the choice of support, essentially due to the acidic nature of the support. Compared to SiO_2 supports, Al_2O_3 supports are less acidic. Al_2O_3 consists of both weak Brönsted and Lewis acidity. Brönsted acidity is due to the isolated surface hydroxyl group and, Lewis acidity is generated by the removal of Al-OH groups (partial dehydroxylation). According to the work done by Bessell [1993], low acidity supported catalysts yield FT products comprising straight chained alkanes and alkenes whereas, the cobalt catalysts deposited on the more acidic supports, produced hydrocarbons consisting mostly branched hydrocarbons and even fractions of aromatics. If gasoline products are desired from the FT reaction, acidic supports are preferred. However, for the production of longer chain paraffins, more basic supports are the ideal choice.

1.2.4.4 Impact of the catalyst synthesis procedure

The method of catalyst synthesis has a profound effect on the properties of the developed catalysts. As seen in the previous sections, any modification to the structural property of the catalyst would plainly affect the reaction rates and directly perturb the FT activity and the hydrocarbon selectivity. The catalyst synthesis procedure fundamentally involves two stages. The first step includes the incorporation of metal salt component into a high surface area support. This is achieved by well defined mechanisms, such as, incipient wetness impregnation,

adsorption from solution, co-precipitation or deposition. The second step includes the conversion of the incorporated metal salt into its corresponding oxide state or to its reduced state. This is obtained by calcining the impregnated metal salts at temperatures which leads to the metal precursor dissociation reaction resulting in the formation of metal oxides. The oxide catalysts are further reduced to its corresponding zero valent metal state in a reducing environment, producing active Fischer Tropsch catalysts.

The choice of cobalt precursors for the catalyst synthesis has shown to impact the catalyst properties, affecting the FT activity. Sun et al. [2000] synthesized silica supported cobalt catalysts using cobalt acetate and cobalt nitrate and cobalt acetate as the catalyst precursors. Highest activity was reported for the catalyst synthesized from cobalt nitrate-cobalt acetate derived metallic sites. A highest CO convesion of 42.5% was observed for nitrate-acetate derived cobalt catalyst while least CO conversion of 6.2% was derived for cobalt acetate derived metallic sites. The primary reason was ascribed to strong metal support interaction with cobalt acetate precursors, thereby reducing the reduction degree. Above all the reduction of acetate species was observed to be promoted by H_2 spillover achieved on cobalt metal from cobalt nitrate. In general, the most common and widely used metal precursor is cobalt nitrate and, the other researched cobalt precursors include cobalt carbonyl, cobalt acetate and cobalt carbonate [Khodakov et al., 2007].

As far as the method of synthesis of cobalt catalysts is concerned, incipient wetness impregnation (IWI) is the most simplest and commonly used technique for depositing cobalt metal or metal oxides on the high surface area supports. Incipient wetness occurs when the support pores are saturated with the aqueous solution containing metal precursors, and no moisture exists over and above the liquid for filling the support pores. The impregnated mixture is then dried and calcined at 623 K to decompose the metal nitrate resulting in the formation of residual cobalt oxides. In general, the time required for calcining of IWI catalysts results in the agglomeration of cobalt particles and reduced metal dispersion. This can be overcome, only to a certain limit, by impregnating the metal precursor in a rotating vessel, maintained under vacuum. Khobragade et al. [2012] synthesized Co/SiO_2 catalysts using the sol-gel method. The method included drop-wise addition of cobalt nitrate solution to a mixture of C_2H_5OH, tetra

ethyl orthosilicate and water (mixed with mass ratio of 5:1:10, respectively). The solution was stirred and heated to 323 K, resulting in the formation of a gel that was further calcined at 823 K for 3 hours to yield approximately 10 wt.% Co/SiO_2. The method propitiously enhances the molecular mixing of the active components and consequently improves the cobalt dispersion. The average cobalt crystallite size ranged from 16.4 to 18.6 nm with the metal dispersion of 0.1% and a CO conversion of 67.5%, yielding primarily paraffins (67.3%) and considerable fractions of oxygenated hydrocarbons (11.5%).

More recently, the **combustion synthesis (CS)** method of metal oxides have been utilized for synthesizing cobalt oxides for Fischer Tropsch synthesis. The combustion synthesis technique, also known as self-propagating high-temperature synthesis (SHS) is an efficient energy compensating method for developing nano-materials, mostly metal-oxides. In the CS method, once the initial exothermic mixture comprising of a *fuel* and an *oxidizer* is ignited by an external thermal source, a swift (1 - 100 mm/s) high temperature reaction wave (1000 K - 3000 K) travels across the reaction mixture in a self-sustained fashion. The inherent heat generated can be favourable utilized to generate cobalt oxides over the support surface. The redox reaction between the fuel (urea, glycine, hexamethylenetetramine) and the oxidizing metal precursor (cobalt nitrate), after preheating to a moderate temperature (423 K - 473 K), self-ignites the entire volume resulting in the formation of nano sized cobalt oxides. The most striking feature of CS includes homogeneous distribution of the metal oxide in a desired composition, since the initial reaction media being in liquid state (aqueous solution of the redox mixture), molecular level mixing of reactants is enabled. Above all the high reaction temperature can volatilize low boiling point impurities, ensuring high product purity [Mukasyan et al., 2007] [Moore and Feng, 1995].

[Shi et al., 2011] synthesized cobalt catalysts by solution combustion method. The authors employed citric acid as the fuel and cobalt nitrate hexahydrate as the metal precursor and the oxidizing compound. The authors in this work have synthesized catalysts in an inert atmosphere (Ar), producing cobalt catalysts in its reduced state (i.e., without the need for further reduction). The resulting catalysts displayed metal dispersion of 15.2% compared to 3.1% for the conventionally synthesized IWI catalysts. The FT activity for the combustion synthesized catalysts showed 47.2% CO conversion and a high CH_4 selectivity of

21.2%, which is indicative of lower C_{5+} productivity. In particular, the details relevant to the FT product distribution is lacking. Another recent work by the same group [Phienluphon et al., 2014], synthesized ruthenium promoted cobalt catalysts using the solution combustion method with citric acid and cobalt nitrate as the redox mixture. The ruthenium promoted cobalt catalysts exhibited highest FT activity with 60.4% CO conversion and a C_{5+} selectivity of 64.1%. Solution combustion synthesized cobalt catalysts in general display excellent properties with respect to crystallite size, degree of reduction and metal dispersion, leading to enhanced FT activity. Since the synthesis of supported catalyst using solution combustion method has been explored only in recent times, its application for Fischer Tropsch reaction has been limited only to a few research groups.

The operation of FT plant is dependent on the efficient utilization of syngas and above all, its conversion to desired hydrocarbon product. Catalysts play a crucial role in determining the overall performance of the FT reaction. Synthesis of highly active and stable FT catalysts is necessary for generation of long chain hydrocarbons with high yields. The use of an effective catalyst is central for economic sustainability and profitable return of the FT plant. For this reason, it is vital to understand the underlying catalytic parameters, as discussed above, and synthesize an active and practical catalyst that can produce desired range of higher hydrocarbons with high productivity.

1.2.5 Realizing the BTL process - the economic aspect

For any bio-fuel related technology to be established on a commercial scale, its economic practicability must be evaluated. Most importantly, the technical aspects of the project must be coupled to the economic evaluations providing a detailed techno-economic analysis. The BTL fuel production economy determines the optimum scale of the BTL plant and, since the hydrocarbon generation process is associated with large investment costs, large scale production is essential for achieving effective returns.

Larson et al. [2009] performed techno-economic analysis on a single pass biomass-to-liquid fuel system via Fischer Tropsch reaction. The syngas for the system is generated in a pressurized O_2 blown fluidized bed gasification system. Fischer-Tropsch reaction is achieved in a low temperature, slurry based FT

reactor. The analysis assumed a biomass input (893 MW_{th}) of and net power generation of 228 MW_e using a steam and gas turbine. The liquid hydrocarbons were produced at a rate of 736 kl/day and the total efficiency (based on the energy output to energy input) of the plant was evaluated to be 57.3%. The total overnight capital cost was estimated at 541 million US$ and, based on the annual levelized fuel production cost, the break-even FT oil production cost was estimated at 0.48 $/l (assuming a biomass cost of $ 50.9/t). Similar work was reported by Tock et al. [2010], who estimated the BTL efficiency of 59.8% and a FT crude oil production cost of 0.9 €/L. The economic development of the established plant, by improved gasification systems, gas cleaning, cooling and purification sections and, the use of advanced high performance catalysts would increase the economic competitiveness in the market for BTL fuels.

At present there are a few BTL plants on commercial scale. These are still small compared to the coal or natural gas based FT plants as established by SASOL in South Africa or by SHELL in Malaysia. A principal factor to be considered for the establishment of large scale BTL plant is the availability of biomass, which is a limiting factor for the scale up of biomass gasification unit. If a choice has to be made for the construction of large scale FT plants, options for converting agricultural residue and waste to syngas have to considered, along with remotely obtained syngas. Resources such as municipal solid wastes (MSW), agricultural residues and plantation residues can be converted to liquid hydrocarbons effectively, economically and with favourable environmental returns if wide range of input feed and output products are handled using a beneficial technique. Such a conversion can be achieved in a bio-refinery which can handle these wide range of feedstocks and output products including special chemicals. Most importantly, if the tail gas from FT reactor is not recycled, again, the residual gases can be converted to electricity, which serves as a propitious co-product from the FT reactor.

1.3 Summarizing the motivation for this work

Conversion of biomass derived syngas to liquid transportation fuel via FT synthesis is a promising technique and attaining importance in recent years - to meet the ever-increasing energy demands and conform to stricter environmental

regulations. Since catalysts play a major role in dictating the overall syngas to liquid fuel conversion efficiencies, synthesis of active catalysts and analysing the effect of the catalyst properties on the FT reaction is crucial for development of the process. To establish a scaled-up BTL process, fundamental understanding of the catalyst effect, process conditions and the conversion and productivity ranges have to be analysed at a micro-scale. Investigations related to the economic viability of a BTL process are crucial and demand fundamental conversion factors that can lead to a sustainable development of a BTL plant.

1.4 Thesis layout

The work involved in this thesis, includes synthesis of novel catalysts for fixed bed Fischer Tropsch reaction. The method of catalyst synthesis developed and employed in this work has a positive effect on the FT productivity, increasing the product yield to considerably large volumes compared to conventionally synthesized catalysts. In the process of synthesizing prolific FT catalysts, the impact of metal support interaction was explored. Understanding of this particular component of supported heterogeneous catalysts has proved to be crucial in achieving increased reactant conversion and superior FT activity. Further, the overall FT economics have been addressed with respect to biomass gasification systems.

Fig 1.13 shows the schematic of the thesis organization. Chapter 2 includes the experimental materials used, catalyst characterization techniques and analysis procedures, fixed bed FT reactor configuration and the FT hydrocarbon product analysis methods.

Chapter 3 deals with the synthesis of cobalt catalysts supported over Al_2O_3 spheres using single step IWI method and the combustion synthesis (CS) method. The CS catalysts are further synthesized under fuel rich conditions with equivalence ratio of 1.2 and 1.5. The properties of the synthesized catalysts are characterized with respect to their crystallite sizes, degree of reduction, cobalt dispersion and metal support interaction. The variation of the cobalt crystallite size with the synthesis procedure and the equivalence ratio is presented. This chapter explains the various phases of cobalt oxides formed on the CS catalysts using H_2 temperature programmed reduction experiments. The effect of catalyst synthesis

procedure on the metal support interaction is explored using X-ray photoelectron spectroscopy. Post catalyst characterization results, the chapter ends with the impact of the CS and IWI catalysts on the FT activity and selectivity. The CS catalysts have a profound effect on the the hydrocarbon product spectrum with large fraction of FT products consisting waxes (C_{24+}).

Chapter 4 covers the impact of support on the Fischer Tropsch reaction. Properties of cobalt catalysts supported over silica-doped-alumina (SDA) are compared with the Al_2O_3 supported catalysts. The catalysts are synthesized with IWI and CS method. The effect of silica doping in alumina support results in reduced cobalt-aluminate formation, that reduces the metal support interaction leading to higher extent of cobalt reduction and higher formation of active metal sites on the support surface. Crucially, this chapter demonstrates the effect of the surface acidity of the SDA supported catalyst and its impact on the syngas conversion rates and the FT product spectrum. Al_2O_3 supported catalysts, owing to its higher surface basicity in comparison to the SDA supported catalysts, result in the formation of waxes (C_{24+}), whereas the middle-distillate paraffinic hydrocarbons (C_{10} -C_{20}) are formed as the primary product for SDA supported catalysts.

Chapter 5 provides a comparison of the catalyst properties synthesized in this work, with respect to their crystallite sizes, degrees of reduction, cobalt dispersion and the metal support interaction. Further, the CO conversion and the overall hydrocarbon yield of the synthesized catalysts are compared with the related cobalt catalysts in the literature.

Chapter 6 deals with the techno-economic analysis of the biomass to liquid (BTL) fuel process, that includes a fixed bed oxy-steam gasification system and a fixed bed FT reactor. The cost of the liquid fuel output is assessed using the annualized life cycle of the systems involved. The global conversions that include conversion of biomass to syngas (developed in CGPL, IISc [Sandeep and Dasappa, 2014]), FT activity and the hydrocarbon yield of cobalt based catalysts, comprise of the BTL building block. The techno-economic analysis is evaluated for a 1000 kg/h fixed-bed, biomass gasification system. Sensitivity analysis is made for the effect of varying costs of biomass, grid electricity cost and the weight hourly space velocity on the liquid fuel cost. The costs of various components utilized in this analysis is assumed exclusively for an Indian scenario.

Chapter 7 provides an overview of the thesis and adds concluding remarks.

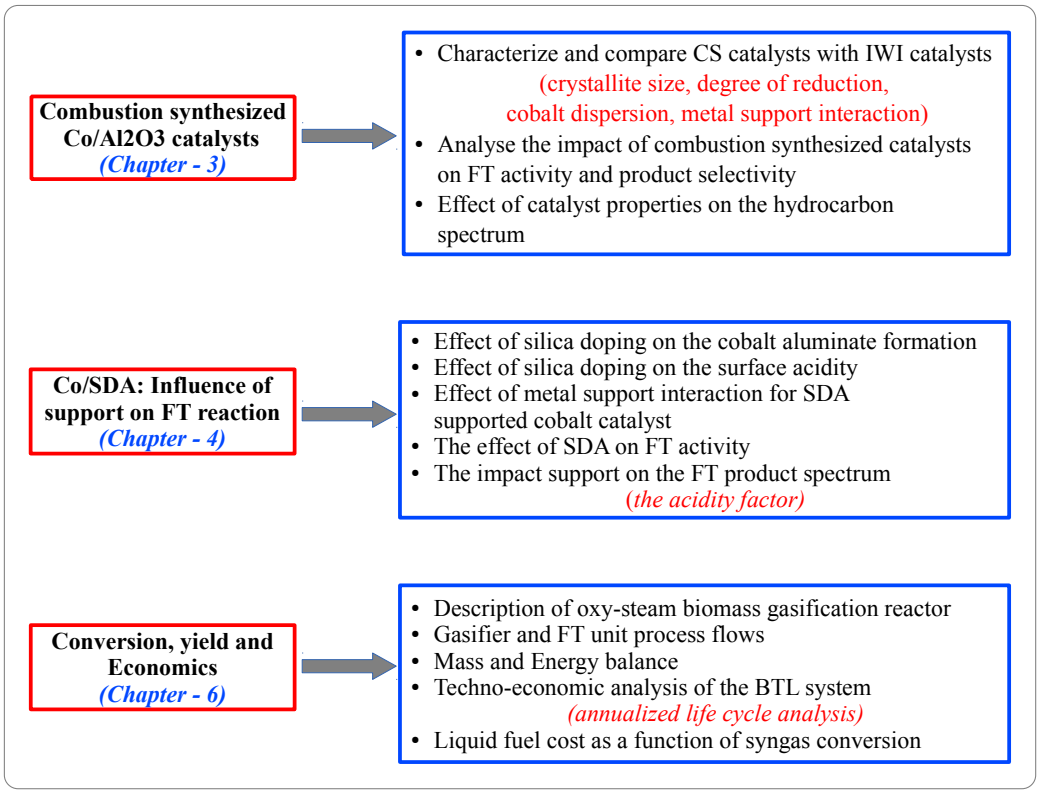

Figure 1.13: The thesis organization

Chapter 2

Experimental materials and methodology

This chapter describes various experimental techniques used in the synthesis and characterization of catalysts for Fischer Tropsch reaction. Details of the FT process conditions and analysis of syngas conversions, catalyst activity and selectivity, and product spectrum analysis procedures are presented. Table 2.1 lists the all the measurement tools and equipments used along with the corresponding measured quantities.

Table 2.1: Measured quantities and corresponding equipments

Measured quantity	**Equipment used**
CS reaction exothermicity	DT-TGA analyzer
CS reaction temperature	Accurate PID controlled muffle furnace 0.3 mm R-type thermocouple
Redox reaction mechanism	FT-IR
BET surface area	Micrometrics Autochem 2920
Catalyst reduction temperature, degree of reduction, metal dispersion	Micrometrics Autochem 2920
Co_3O_4 , CoO & Co^0 detection, crystallite size	Rigaku Smartlab XRD
Cobalt oxidation states, nature of metal support interaction	Axis Ultra XPS
Fischer Tropsch reaction	Fixed bed high pressure reactor
Syngas and gaseous hydrocarbon analysis	Perkin Elmer Clarus-680 GC (*FID TCD*)
Liquid hydrocarbon analysis	Perkin Elmer SQ8 GC-FID

2.1 Catalyst synthesis

The FT reactions were carried out over supported cobalt catalysts in a fixed bed reactor. Cobalt catalysts were deposited over high surface area γ-Al_2O_3 spheres (BET surface area = 158 m^2/g, diameter = 0.8-1.1 mm). Catalyst synthesis conditions have a prominent effect on the catalyst properties which in turn have a direct consequence on the FT activity and the hydrocarbon selectivity. The effect of catalyst properties such as crystallite size, metal dispersion, cobalt reducibility have been discussed in Chapter 1.

The Al_2O_3 supported cobalt catalysts were synthesized by the novel combustion synthesis (CS) method and the properties of combustion synthesized catalysts were compared with the characteristics of catalysts synthesized by conventional incipient wetness impregnation (IWI) method. Cobalt nitrate hexahydrate ($Co(NO_3)_2.6H_2O$) is used as the metal precursor for all cobalt synthesis. In the combustion synthesis (CS) of catalysts an aqueous solution of metal precursor (*oxidizing specie*) and a fuel (*reducing specie*) is impregnated into the support pores. The redox mixture impregnated support is ignited by an external heating source. Once ignited, a swift high temperature (1000 K - 2000 K) reaction front propagates across the support volume, resulting in the rapid decomposition of metal precursors and simultaneous formation of metal oxides. The redox reaction after ignition, does not demand an additional energy for its completion. The CS reactions are identified by large rates of heat release, high temperature rise rates ($\sim$ 200 - 500 K/min), and rapid rates of product formation. These extreme reaction dynamics limit the synthesis of catalysts with metal loading greater than 7% - 8%. For higher metal loadings, the combustion products form with uncontrolled *explosion*, resulting in powdering of the catalysts and in most cases, mass loss of the active material. This particular constraint prevented the use of combustion synthesized catalysts for use in FT reactions, where the metal loading is generally preferred to be >15% [Medina et al., 2010] [Jacobs et al., 2002]. Also, the use of these catalysts in a fixed bed reactors necessitates the re-pelletization of the powdered catalysts, which is an unpropitious route. Majority of the CS catalysts reported in the literature with high metal loading exist in powdered form, that can only be used in a fluidized bed or a slurry phase reactor [Zhao et al., 2012] [Mukasyan and Dinka, 2007] Patil et al. [2008]. Series of combustion synthesized cobalt catalysts by Shi et al. [2011] and Phienluphon

et al. [2014], for Fischer Tropsch reaction, have been discussed earlier (Chapter 1, Section 1.2.4.4). The authors in that work synthesized the catalysts in powdered form for use in a slurry phase reactor with a temperature of 513 K and pressure of 1 MPa. The combustion synthesized catalysts, under those conditions displayed high methane selectivity (S_{CH4} = 21.2%, α=0.73). Strikingly, the catalysts synthesized by conventional IWI method showed superior FT activity compared to CS catalysts (S_{CH4} = 11.6%, α=0.80). However, the lesser performance of the CS catalysts could be attributed to the improper reaction conditions (higher catalyst activity results in higher rates of exothermic reaction and, could lead to higher reaction temperature if the effective heat transfer rates are not enhanced). LeViness et al. [2014] reported the use of silica supported cobalt catalyst, synthesized by *organic matrix combustion* process and, used in a microchannel reactor. Though the cobalt loading, or the synthesis procedure is not evident in the reported work, the authors reported an average conversion of 70%, CH_4 selectivity of 7%, and C_{5+} selectivity of 88%. The productive reaction performance was achieved by improved catalyst properties and efficient reactor performance.

The following sections describe the two catalyst synthesis procedure employed in this thesis, for use in fixed bed Fischer Tropsch reaction.

2.1.1 Catalysts synthesis by IWI method

IWI method involves the immersion of a high surface area support into an aqueous solution of dissolved metal precursor [Regalbuto, 2006], in this case $Co(NO_3)_2.6H_2O$. The governing driving force for filling of support pores is the capillary pressure. Catalysts were synthesized with metal loading (L) of 20 wt.%. The mass of $Co(NO_3)_2.6H_2O$ required for the catalyst synthesis is determined by Eqn.2.1. Here, m_{pc} is the mass of metal precursor, MW_{pc} and MW_{Co} are the molecular weight of the metal precursor and metallic cobalt respectively, m_{cat} is the mass of catalyst synthesised and L is the metal loading. Since cobalt nitrate hexahydrate is used as the metal precursor for all catalyst synthesis in this work, MW_{pc} is 291.03 g/mol.

$$m_{pc} = \frac{MW_{pc}}{MW_{Co}} \cdot \frac{m_{cat} \cdot L}{100} \tag{2.1}$$

The support and the aqueous solution of cobalt nitrate are stirred and impregnated in a single step. The impregnated mixture was then calcined in a muffle furnace at 673 K for a duration of 4 hours. Fig 2.1 provides a pictorial representation of the IWI synthesis method.

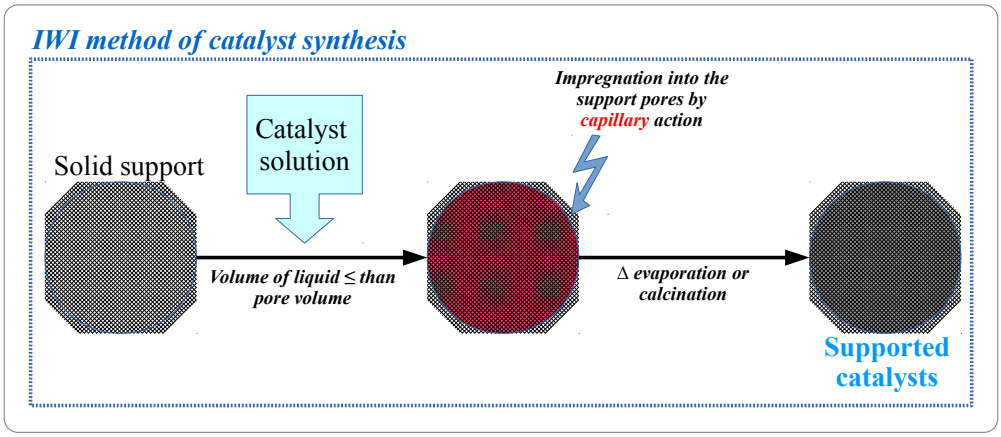

Figure 2.1: Incipient wetness impregnation method of catalyst synthesis

2.1.2 Catalyst synthesis by combustion synthesis method

For CS catalysts, the heat required for synthesizing cobalt oxide from the metal precursor is generated from the self-sustaining chemical reaction of $Co(NO_3)_2.6H_2O$ and a fuel. The fuel used in this work is hexamethylenetetramine, which is a heterocyclic organic compound with the formula $C_6H_{12}N_4$. The stoichiometry for this redox reaction is selected with the equivalence of one, to achieve maximum heat release. From the reaction stoichiometry, as described in Eqn.2.2, the metal nitrate to fuel molar ratio is 3.86. The redox mixture are impregnated into the supports similar to the IWI synthesis method. Calcination of the CS catalysts are achieved by maintaining the furnace at the redox mixture ignition temperature. The method of synthesizing cobalt catalysts has been applied for patent. (*"Metal catalysts and process for the preparation of catalysts thereof" - patent application number- 6490/CHE/2015*)

$$27Co(NO_3)_2.6H_2O + 7C_6H_{12}N_4 \longrightarrow 9Co_3O_4 + 41N_2 + 204H_2O + 42CO_2 \quad (2.2)$$

2.2 Catalyst Characterization

The properties of the synthesized catalysts have a profound effect on the catalyst activity and selectivity. The synthesised catalysts were characterized using techniques that are listed and described in the following sections.

2.2.1 BET surface area

The BET surface area analysis is performed using a Micrometrics Autochem 2920 analyser, to evaluate the total surface area (m^2/g) of the catalyst support and the synthesized catalyst samples. Prior to the experiment, the powdered samples were outgassed at 573 K. After outgassing the sample, a mixture of nitrogen and helium (15% N_2), was flown over the sample, which was immersed in liquid nitrogen bath (77 K). The adsorption and desorption of the nitrogen were recorded, and the magnitude of N_2 desorbed at 77 K and sample weight were used to evaluate the total specific surface area.

The surface area was calculated from the Brunauer-Emmett-Teller (BET) equation. The monolayer capacity, V_m, was obtained from the plot of $P/(V \cdot (P_\circ - P))$ versus $P/P_\circ$ in the pressure range of $0 < P/P_\circ < 0.30$.

2.2.2 Simultaneous thermal analysis (DTA-TGA)

The combustion thermal events are characterized with Perkin Elmer STA-6000 analyser for differential thermal analysis (DTA) and thermogravimetric analysis, to obtain the real-time measurements and analysis of sample weight change and heat flow. The analysis indicates a precise temperature at which the combustion reaction initiates. The sample is heated at the rate of 5 K/min in static air starting from initial temperature of 313 K to a maximum temperature until no weight loss is observed (dm/dt=0), indicating completion of the combustion reaction. The temperature calibration of the analyser was performed with the standard alumel alloy, which has a curie point of 425 K.

Further, to measure the combustion reaction temperature, a known mass of the redox-mixture impregnated support is placed in a beaker and heated in a muffle furnace. An R-type (1 mm diameter) thermocouple is inserted into this beaker which contains the impregnated support. The reaction temperature is

recorded using a P-Daq data acquisition system. The redox mixture is heated by increasing the furnace temperature at the rate of 10 K/min using a PID controller. Once the reaction gets initiated, a reaction wave spans throughout the support volume forming cobalt oxide.

2.2.3 Fourier transform infra red (FT-IR) spectroscopy

The FT-IR spectra of the impregnated supports and calcined catalysts are examined to investigate the nature of the redox complex and most importantly, to probe if the completeness of the redox reaction. The spectrum also evidences the presence of any combustion residues on the catalyst surface. The FT-IR spectra are obtained using a Perkin Elmer 100 FT-IR spectrometer coupled with an Attenuated total reflection (ATR) accessory. ATR sampling technique when used simultaneously with the infra-red spectroscopy, enables the samples to be examined directly in solid or liquid state without the need for any further preparation. The samples are scanned in mid-infrared region, from 4000 cm^{-1} - 400 cm^{-1}. The instrument consists of a diamond ATR-crystal and the the detector is Lithium Tantalate ($LiTaO_3$). The samples are scanned in the mid-IR region to obtain a FT-IR spectra of 64 scans with a resolution of 4 cm^{-1}.

2.2.4 Temperature programmed reduction and desorption (TPR-TPD)

The temperature programmed reduction and desorption (TPX, X = reduction/desorption) experiments were conducted to determine the catalyst reduction temperature, the degree of reduction and the metal dispersion. The TPX results also provide an useful insight into the metal support interaction of the synthesized catalysts. The TPX studies are performed in a Micrometrics Autochem 2920 TPX system. A known mass of sample ($\sim$ 50 - 100 mg) is weighed and placed in a U-shaped quartz sample tube and fixed in a tubular furnace. The furnace temperature is measured using a 2 mm K-type thermocouple and controlled using a PID controller. The Micrometrics Autochem 2920 TPX sample block is shown in Fig 2.2. Prior to TPR analysis, the sample is conditioned by heating in Ar at 473 K for two hours, to remove any traces of moisture. Thereafter, the quartz cell is cooled to 323 K and the TPR analysis begins by flowing

analysis gas (10% H_2 in Ar), over the sample with a flow rate of 10ml/min. As the gas flows, the sample temperature is increased linearly from 323 K to 1273 K at a rate of 10 K/min. Changes in the concentration of the gas mixture are determined by a thermal conductivity detector (TCD), and this information yields the H_2 uptake volume. The TCD is made up of a highly accurate, gold plated filaments that detect minute changes in the thermal conductivity of gases. The TCD block is maintained at 473 K all through the analysis. To determine to amount of chemisorbed H_2, approximately 30 mg of catalyst sample is reduced in pure H_2 (purity >99.995%) for 16 hours at the reduction temperature and cooled to 373 K. At this temperature, the gas flow is switched to Ar, and the flow is maintained at this temperature for one hour to remove physisorbed H_2. The catalyst cell is then ramped to 773 K at a rate of 20 K/min in Ar flow to desorb the chemisorbed H_2. The degree of metal reduction (DoR), which is the fraction of cobalt oxide reduced to metallic cobalt is evaluated by Eqn.2.3. Here, N_{H2-ads} is the H_2 uptake from the TPR spectra, L is the percentage metal loading, SF is the Co^0 reduction stoichiometric factor (1.33), m_{cat} is the mass of catalyst used for the TPR and TPD process. The metal dispersion, which is the non-dimensional number representing the fraction of free metal atoms over the total number of metal atoms in the catalyst, is calculated using the formula stated in Eqn.2.4. The dispersion calculation assumed dissociative H_2 chemisorption with stoichiometry factor of 0.5.

$$DoR(\%) = \frac{N_{H2-ads} * 58.93}{m_{cat} * L * SF} * 100 \tag{2.3}$$

$$D(\%) = \frac{N_{H2-des} * 2 * 58.93 * 10^6}{L * m_{cat} * DoR} \tag{2.4}$$

Temperature programmed desorption of ammonia (NH_3-TPD), which is an extensively used technique for characterizing the acid sites on catalyst surfaces, was employed to determine the surface acidity and the magnitude of active sites on the supports and the synthesized catalysts [Camiloti et al., 1999]. Around 30 mg of sample is placed in the quartz sample holder and saturated with NH_3 at 373 K for two hours. The gas flow is then switched to Ar with a flow rate of 50 ml/min at the same temperature for an hour to remove physisorbed NH_3. The sample temperature was then increased to 700 K at 20 K/min. The amount of

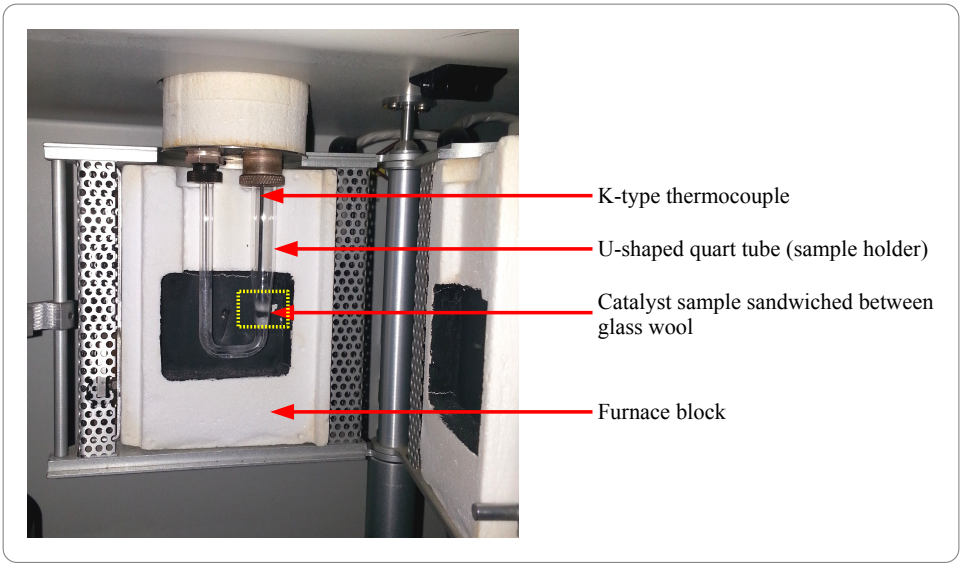

Figure 2.2: TPX unit consisting of the sample holder and the furnace section

desorbed NH_3 is recorded to determine the number of acidic sites.

2.2.5 X-ray diffraction (XRD)

The X-ray diffraction pattern of all the catalyst samples were obtained at room temperature in a Rigaku Smartlab XRD diffractometer with Bragg-Brentano parafocusing geometry. The instrument is equipped with CuKα x-ray source with an average wavelength of 1.542 $\mathring{A}$ obtained by setting the copper target x-ray tube to 40 kV and 30 mA. In order to reduce the unwanted radiation from the X-Ray source and to eradicate maximum possible Kβ radiation, curved graphite single crystal monochromator was used. The incident beam optics included a Soller slit of 5° and a Bragg-Brentano (BB) selection slit. The diffracted beam optics included a Soller slit of 5° and parallel slit analyser (PSA) open as the receiving optical device. The powdered samples spread on a rectangular glass slide and placed on a flat plate stationary holder. The 2-θ values were scanned at a rate of 0.2°/min from 30° to 70°.

The cobalt and cobalt oxide crystallite size were evaluated using the Scherrer equation, shown in Eqn.2.5. Here, L is the crystallite size in nano meter, k is the Scherrer constant (0.9), λ is the Cu Kα wavelength (1.542 $\mathring{A}$), β_e is the effective peak broadening at full width half maxima, after subtracting the instrumental

line broadening and, θ is the half angle of the peak. Integral breadth method for the x-ray line profile analysis was performed using the Voigt model for intrinsic, as well as the instrumentation diffraction peak shapes. The contribution of the instrument to the peak broadening and evaluate the β_e was determined by method shown in appendix A.

$$L = \frac{k \cdot \lambda}{\beta_e \cdot cos(\theta)} \tag{2.5}$$

2.2.6 X-ray Photoelectron Spectroscopy (XPS)

XPS tool was used to determine the various oxidation state of the synthesized catalysts. A constant energy X-ray beam, such as that of Al-K_α (1486.6 eV), or Mg-K_α, is irradiated on the sample surface. Consequently, the photon energy absorbed by the atom is conserved as a sum of the binding energy of the core electron and the kinetic energy of the escaping electron. Kinetic energy (E_k) of the photo-electron is given by Eqn.2.6. Here, hν is the energy associated with the exciting radiation, E_B is the binding energy (B.E.) of the electron in the solid and ϕ is the work function.

$$E_k = h\nu - E_B - \phi \tag{2.6}$$

During the XPS analysis, Siegbahn et al. [1967] reported the sample contamination by carbon, which originated from the pump oil vapours. Conveniently, the occurrence of B.E peak due to carbon contamination is used as an internal calibration standard for the shift in B.E. peaks. The C 1s peak at 284.8, as obtained from the graphite, is taken as a standard. The information about the valence state of an atom in the solid sample can be determined from the shift in the binding energy values of the core level electron with respect to a neutral atom, which is referred to as the core-level chemical shift [Axelson et al., 1967]. The core-level chemical shift in an atom is dependent on the effective charge which is in turn influenced by factors such as valence state, coordination number, bond distance etc. This influence is described by the charge potential model, and described in Eqn.2.7. In this equation, E_i is the B.E. of a particular core level electron of atom i, E_i^o is an energy reference in the element, q_i is the charge on atom i, and the last term sums the potential at atom due to point charges on

the surrounding atoms. Therefore, even though cobalt atom exists in +2 and +3 oxidation state, over Al_2O_3 supports, a difference in the net effective charge on the cobalt atom would alter the binding energy. Generally, the binding energy of $Co2p_{3/2}$ increases with effective charge, q, on Co.

$$E_i = E_i^o + kq_i + \sum_{i \neq j} \frac{q_i}{r_{ij}} \tag{2.7}$$

XPS spectra of all the samples were recorded in Axis Ultra system with Al Kα radiation (hν = 1486.6 eV), operated at 15 kV, 10 mA and at ambient temperature. The sample for analysis were powdered, suspended in ethanol solution and then drop cast on a double sided carbon tape and placed on silicon wafer. The prepared samples were dried for 24 hours and then placed into the ultra high vacuum preparation chamber at 10^{-8} Torr for 6 hours, and then transferred to the analysis chamber at 10^{-9} Torr housing the analyser. The narrow region of core level spectra of the calcined and reduced catalysts are analyzed to obtain information on the cobalt oxidation state. The XPS spectrum peak shift is corrected using the B.E. of C-1s spectra observed at 284.8 eV. The raw XPS data are deconvoluted using CasaXPS software to separate the contributions from various oxide phases, after subtracting the linear background.

2.3 Fischer Tropsch reaction

The synthesized catalysts are reduced in flowing hydrogen, and tested for its FT activity in a high pressure, fixed bed FT reactor. The performance of the catalysts are analyzed with respect to the syngas conversion, and selectivity to gas phase and higher hydrocarbons.

2.3.1 Bulk catalyst reduction

The CS and IWI catalysts, prior to FT reactions, are reduced in a tubular furnace in flowing H_2 (purity > 99.995%), with a flow rate of 100 ml/min. The reduction temperature of the catalysts are selected based on the temperatures obtained from the TPR experiments. 25 g of catalyst is weighed into a quartz tube of 8 mm diameter. H_2 is circulated over the catalyst and the temperature

is increased linearly from 323 K to the reduction temperature at the rate of 10 K/min. The catalyst is reduced for a duration of 16 hours. Fig 2.3 shows the tubular furnace for the reduction of bulk catalysts. After 16 hours, the furnace temperature is reduced to ambient temperature, and the flow of hydrogen is stopped. The reduced catalysts are the carefully transferred to FT reactor.

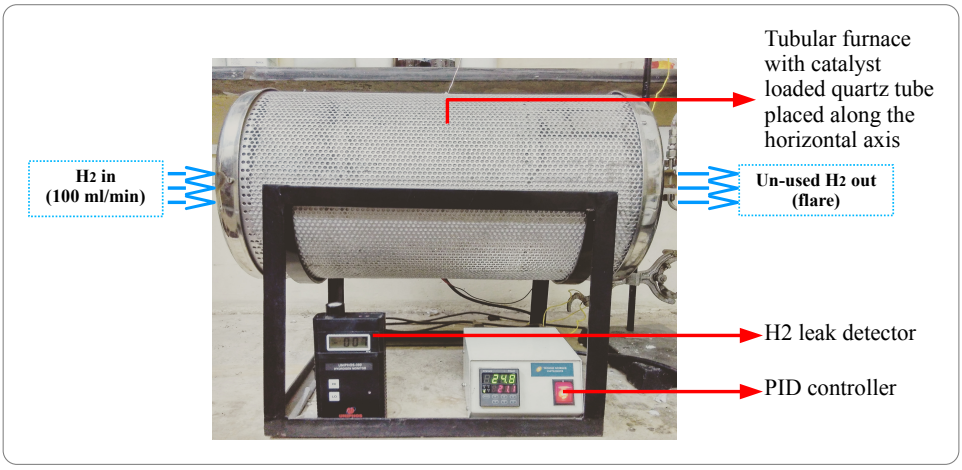

Figure 2.3: Bulk catalyst reduction setup

2.3.2 Fixed bed FT reactor

FT reactions were performed in a high pressure, fixed bed reactor, constructed of SS-316 material. The syngas feed was obtained from pressurized cylinders consisting of 70% (vol%) H_2 and 30% (vol%) CO, corresponding to a H_2/CO ratio 2.3:1. The catalyst cell comprised of a 30 ml cuboid shaped section whose dimensions are shown in Fig 2.4. Six grams of reduced cobalt catalysts are loaded into the catalyst bed for every FT reaction. To maintain isothermal conditions in the reactor bed, the catalyst is mixed with β-SiC with a mass ratio of 5:1. The catalyst bed is placed in a cylindrical heating chamber and is heated to the reaction temperature of 503 K and a pressure of 3 MPa. The bed temperature is increased linearly from ambient temperature to 503 K at the rate of 2 K/min. A RTD Pt-100 sensor coupled with a *PPI* make self-tune 8-segment precision PID controller is used to monitor and control the bed temperature. The RTD is inserted into an axially located thermowell. Fig 2.5 shows the catalyst bed temperature during the FT reaction, as observed for a duration of 2 h.

The reactor pressure is controlled by TESCOM ER-5000 back pressure reg-

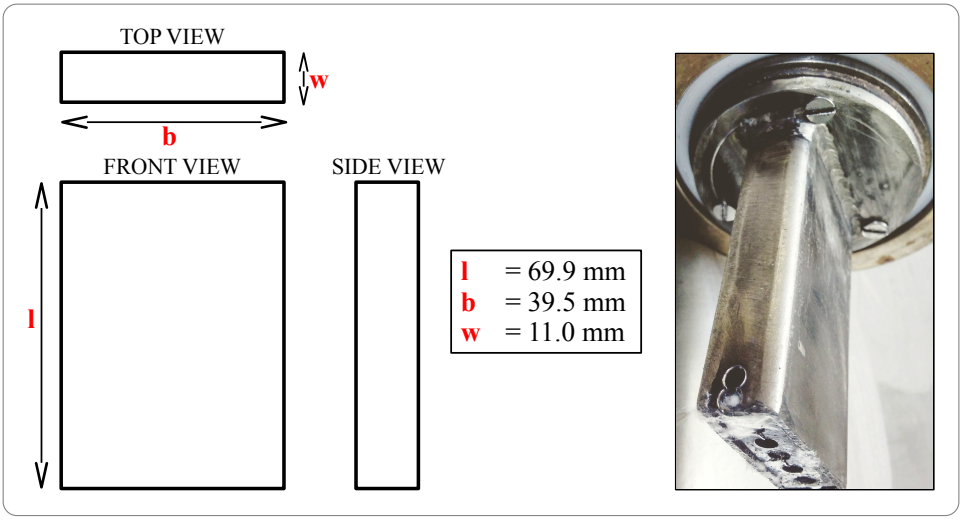

Figure 2.4: Catalyst cell with the dimensions

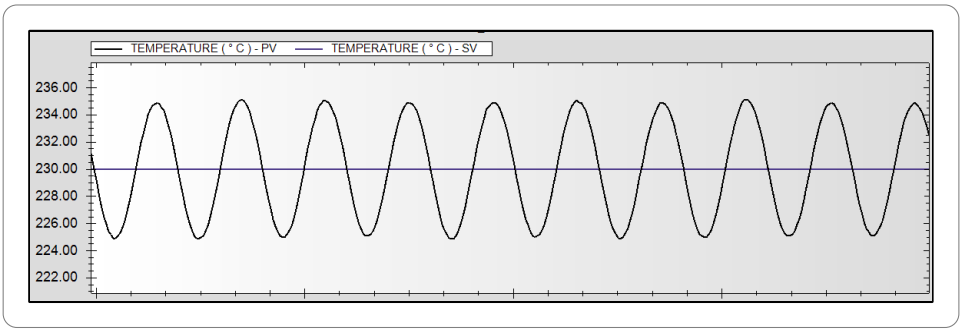

Figure 2.5: Catalyst bed temperature during the FT reaction

ulator. The pressure signal from the reactor bed is transmitted to the BPR by a pre-calibrated WIKA S-20 pressure transmitter. Simultaneously, the reactor pressure is monitored using a Neuro 100ac pressure indicator, as well as an analog pressure gauge. The flow to the reactor is controlled using a flow-mode operating BROOKS digital mass flow controller. The mass flow controller was calibrated using a bubble flow meter, in the desired flow range. Fig 2.6 shows the calibration profile for the mass flow controller. Subsequently, the actual syngas flow rate is evaluated as a linear function of the set flow rate. For the FT experiments conducted in this work, the syngas flow rates are varied such that the weight hourly space velocity ranges from 873.3 ml/(h·g_{cat}) to 2610 ml/(h·g_{cat}).

The products of FT reaction consist of lighter gas phase hydrocarbons and heavy liquid phase paraffins. The liquid products from the hot gas are separated

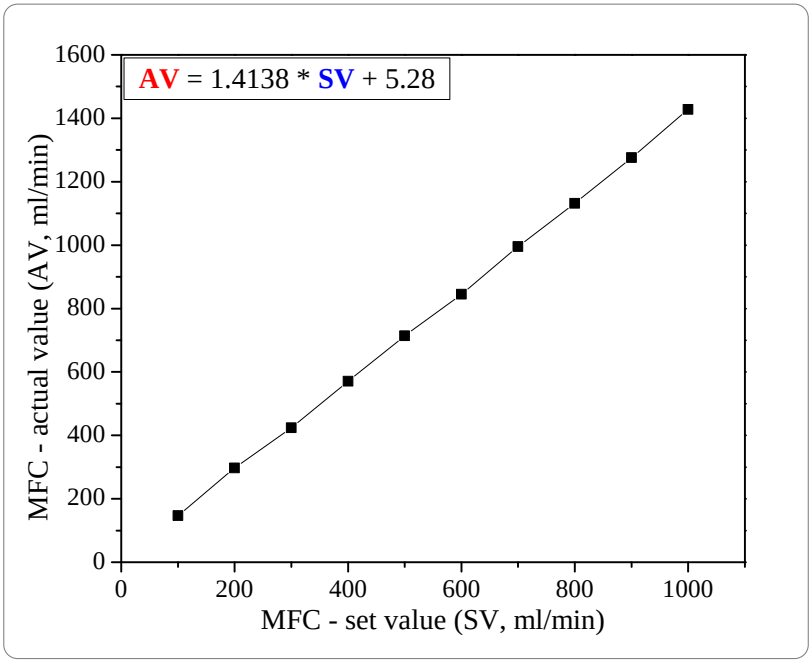

Figure 2.6: BROOKS mass flow controller calibration chart

in a single pass water jacketed condenser which is maintained at 268 K using a MC3i IKA chiller. The gas phase hydrocarbons are analyzed using an online gas chromatograph and the liquid hydrocarbons, collected in the condenser, are analyzed using a GC-MS. Fig 2.7 shows the integrated FT reactor configuration and Fig 2.8 shows the detailed layout of the FT synthesis section.

2.3.3 Product analysis

The products from the FT reactor that include the gas phase hydrocarbons, liquid hydrocarbons, unconverted syngas and fractions of CO_2 were analysed using gas chromatograph. CO, H_2 and CO_2 are analysed using TCD detector in the *Mayura Anaytical GC-1100* system and the gas phase hydrocarbons were analysed using the FID detector in the *Perkin Elmer Clarus 680* gas chromatograph. Helium was used as a GC carrier gas. H_2, CO and CO_2 were analyzed using a mol-sieve and haysep-A packed columns while the gas phase hydrocarbons were separated in an Elite-Alumina column. The GC conditions and the method of analysis are explained in appendix B

The oven temperature is maintained at 403 K with the carrier gas flow rate

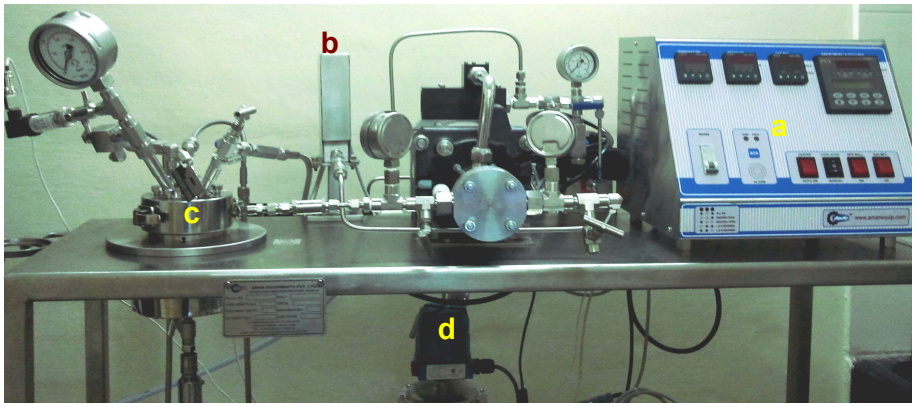

a = Instrumentation pannel

b = Mass flow controller

c = Reactor with safety valves, RTD, pressure transmitter, and pressure gauge

d = Back pressure regulator

Figure 2.7: FT reactor configuration indicating major components

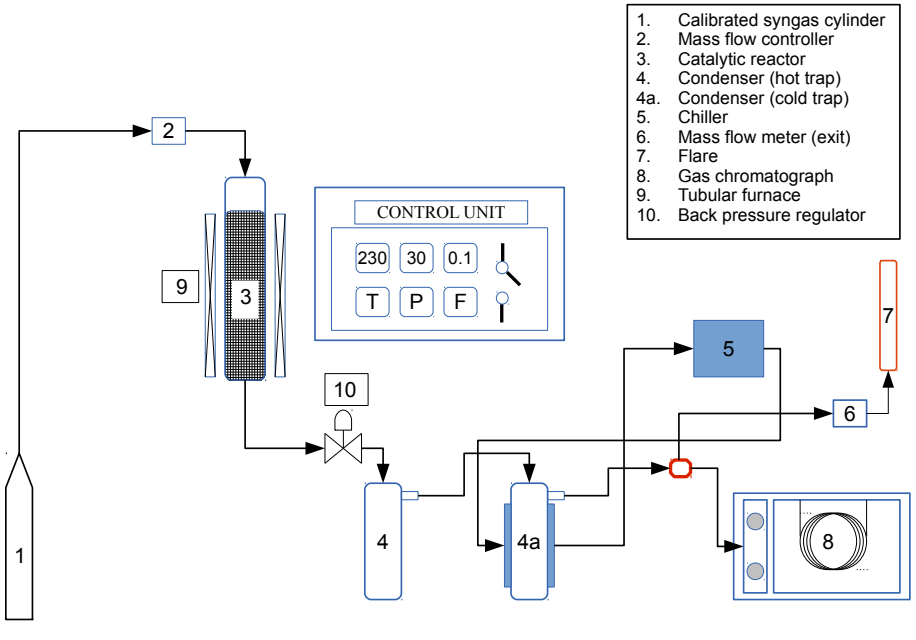

Figure 2.8: Layout of the FT synthesis unit

of 30 ml/min. The gas sample to be analyzed, was injected into the GC via a gas auto-sampler and a PSS injector which was maintained at 473 K. Various gas

species were identified and quantified using TCD and FID detectors. The FID is calibrated using standard gas mixture, as listed in Table B.2.

Liquid products were analyzed separately by a Clarus SQ8 GC-MS system, that consisted of an Elite 5MS column (length = 30 m; internal diameter = 0.25 mm). Helium is used as a carrier gas with a flow rate of 1 ml/min. The analysis method included injection of 5μl sample and heating the GC oven from 313 K to 573 K at a ramp rate of 5 K/min, and holding the temperature at 573 K for 20 minutes. The sample preparation included dilution of the hydrocarbon sample with 2-propanol solvent. The liquid hydrocarbon sample was dissolved in the solvent with a sample to solvent volumetric ratio of 1:100. The hydrocarbon fractions were quantified by calibrating the GC-MS, which included injecting known fraction of Supelco paraffin standards. The calibration constants for the hydrocarbon standard are shown in Table B.3.

The concentrations of the liquid hydrocarbon products from the FT reactor were obtained by multiplying the GC-MS chromatogram area with the calibration factor. The product composition and the exit flow rates are recorded for a duration of 160 h, after a catalyst stabilization period of 24 h.

As explained in the previous chapter, the FT reaction is a surface polymerization reaction and the generation of higher hydrocarbons is characterized by the carbon chain growth and the subsequent chain termination on the catalyst surface. The work reported by [Schulz, 2003] showed that catalyst activation lasts for about 3-4 days. Schulz's work further showed that under the FT reaction conditions the cobalt surfaces segregate leading to disproportionation of sited for higher and lower coordination, which develops the activity for the reactions within FT mechanisms. As shown in Fig 2.9, the FT regime develops in 3 episodes. Episode 1 is the first syngas adsorption regime. During episode 2, the catalyst activity increases and selectivity changes are observed. Finally, the steady state FT synthesis are observed during episode 3 (after about 50 h). This observation was explained by the *corrosive chemisorption* phenomena of metal surfaces, wherein the cobalt crystals are roughened and respectively segregated. This change in surface structure is an essential feature of FT synthesis with cobalt catalysts [Schulz, 2003].

For the FT experiments performed in this thesis similar phenomena was observed, and the steady state FT activity was recorded only after 24 hours.

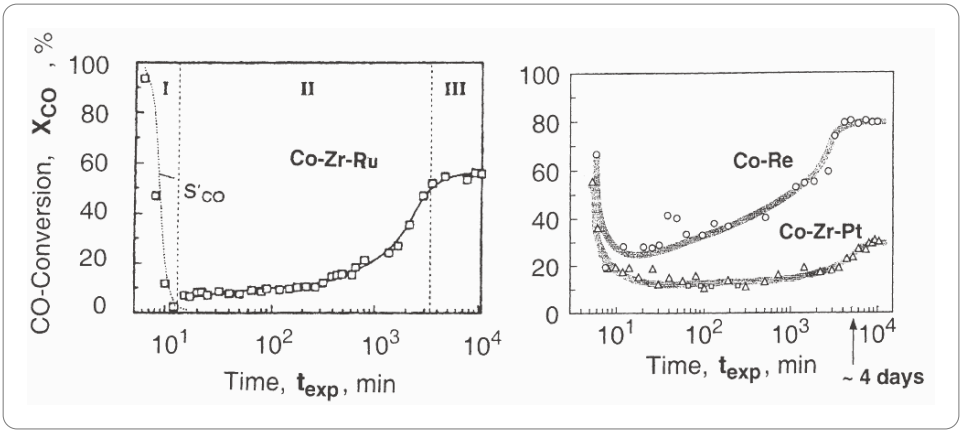

Figure 2.9: Cobalt catalyst activation regime
[*Figure from [Schulz, 2003]. Steady state FT activity achieved in 3 regimes of catalyst "formation", explained by the corrosive chemisorption phenomena*]

The CH_4 selectivity during the transient conditions remained predominantly high (S_{CH4} = 30 - 35%), after which the selectivity gradually dropped. Therefore, all the activity and selectivity measurements were recorded after 24-30 hours of catalyst stabilization.

The percentage CO conversion and hydrocarbon product selectivity are evaluated according to Eqn.2.8 and Eqn.2.9. Here, $\dot{m}_{CO-in}$, $\dot{m}_{CO-out}$ are the mass flow rates of CO entering and leaving the system and $\dot{m}_{CH*}$ is the mass flow rate of the hydrocarbon product specie. The mass flow rate and the yield of of hydrocarbon product (g-$_{HC}$/g-$_{syngas}$) is evaluated according to Eqn.2.10 Eqn.2.11 respectively. Here, $\dot{m}_{CH*}$ and $\dot{m}_{syngas}$ are the mass flow rate of the hydrocarbon fraction and the syngas mass flow rate, measured in g/h respectively. Y_{CH*} is the yield of the hydrocarbon fraction evaluated as the mass of hydrocarbon fraction generated per unit mass of syngas. Most importantly, identical process conditions, especially the weight hourly space velocity (WHSV), were considered for comparing yields of various catalysts, including other catalysts from the literature.

$$\chi_{CO}(\%) = \frac{\dot{m}_{CO-in} - \dot{m}_{CO-out}}{\dot{m}_{CO-in}} \cdot 100 \tag{2.8}$$

$$S_{CH*}(\%) = \frac{\dot{m}_{CH*}}{\dot{m}_{CO-in} - \dot{m}_{CO-out}} \cdot 100 \tag{2.9}$$

$$\dot{m}_{CH*} = S_{CH*} \cdot \frac{\dot{m}_{CO-in} - \dot{m}_{CO-out}}{100} \tag{2.10}$$

$$Y_{CH*} = \frac{\dot{m}_{CH*}}{\dot{m}_{syngas}} \tag{2.11}$$

2.4 Summary

The experimental tools used for the synthesis and activation of catalysts, characterization of redox mixtures, and the spectroscopy instruments (XRD, XPS, SEM-EDS) are shown in Fig 2.10 and Fig 2.11. This chapter presented the quantification instruments and the experimental methodology used for synthesizing and characterizing catalysts, Fischer-Tropsch reactions and product analysis.

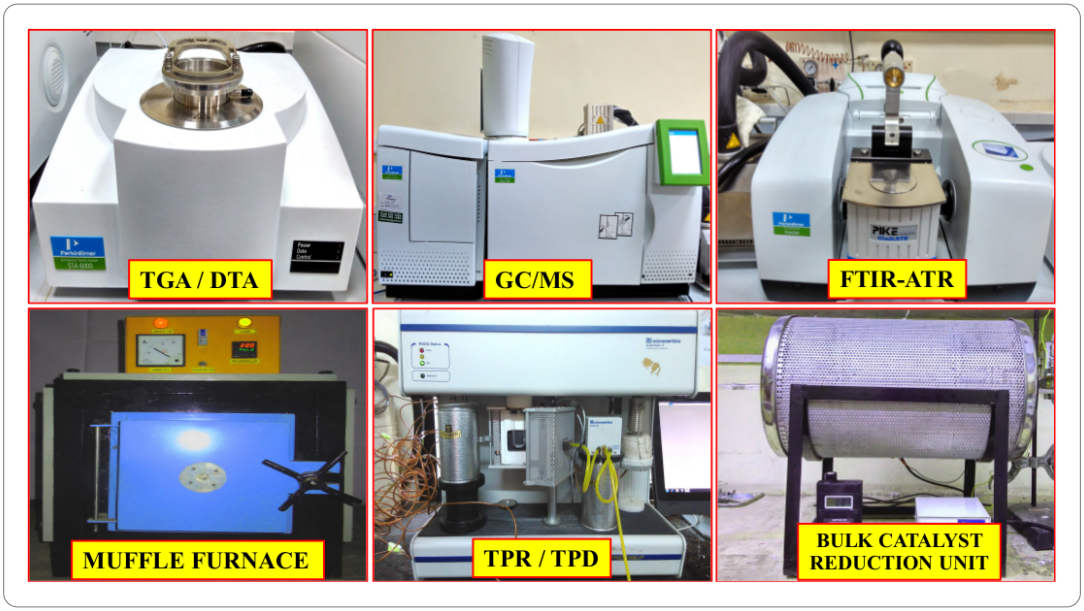

Figure 2.10: TGA-DTA ; GC-MS ; FT-IR ; muffle furnace; TPR-H_2 chemisorption; bulk catalyst reduction

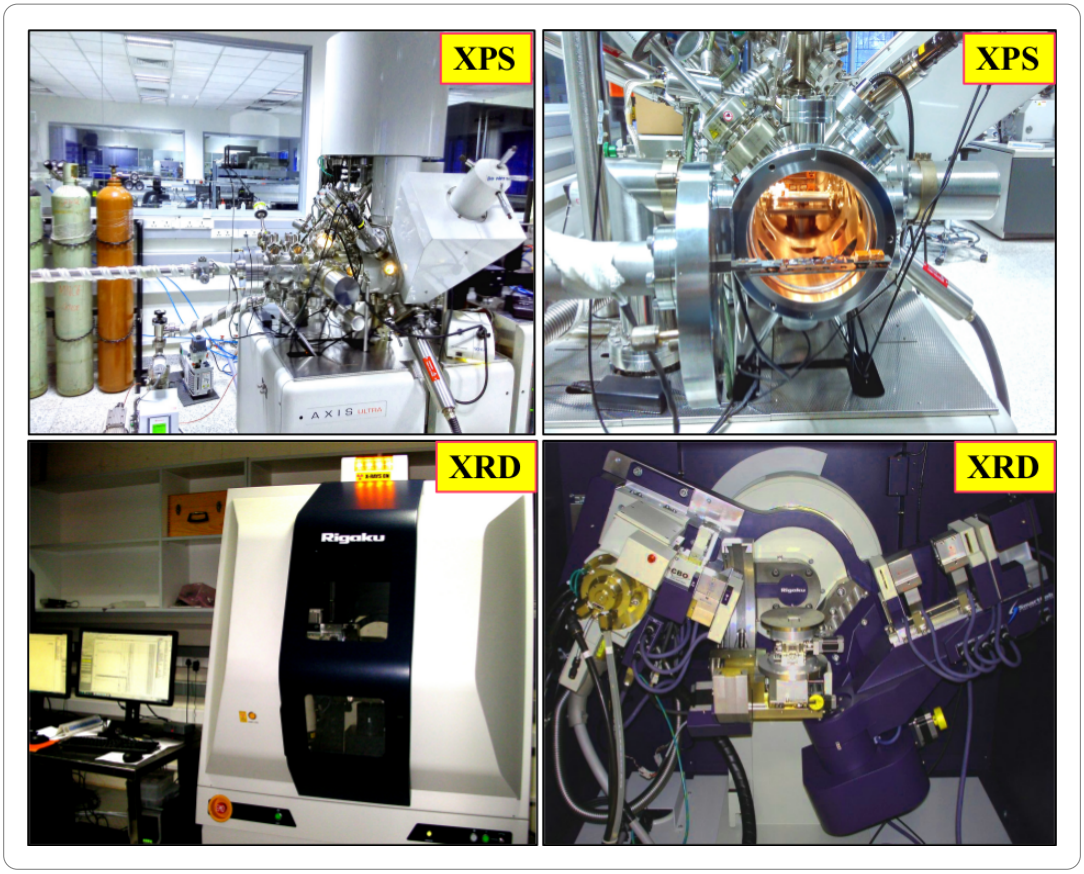

Figure 2.11: X-ray photoelectron spectroscopy (XPS) & X-ray diffraction (XRD)

Chapter 3

Combustion synthesised γ-Al_2O_3 supported cobalt catalysts

The present chapter is concerned with the synthesis, characterization and the FT activity of Al_2O_3 supported cobalt catalysts. The catalysts were synthesized by incipient wetness impregnation (IWI) method and the novel combustion synthesis (CS) method, as described in the previous chapter. The properties and the performance of the combustion synthesized catalysts are compared with the conventional IWI method. Additionally, the chapter shows the effect of the combustion reaction stoichiometry (the fuel to oxidizer ratio) on the catalyst properties and its consequent effect on the FT reaction performance. The combustion synthesized catalysts were synthesized with equivalence ratio of 1, 1.2 and 1.5. Particularly, the impact of the synthesis procedure and, the effect of the fuel to oxidizer ratio on the cobalt-support interaction has been investigated. FT active metals deposited over oxide support show a distinct metal support interaction (MSI) and, depending on the nature of this MSI, the FT activity is shown to be dynamically affected.

3.1 Catalyst characterization

The catalyst synthesis conditions display pronounced effect on the catalyst properties, which include crystallite size, degree of reduction and metal dispersion. These properties directly affect the FT activity, hydrocarbon selectivity and the product distribution.

3.1.1 Combustion reaction dynamics

CS catalysts are synthesized with a reaction stoichiometry such that the impregnated redox mixture react over the support surface without any residual traces of carbonaceous products or un-burnt fuel and metal precursors, resulting exclusively in the formation of Co_3O_4 . Therefore, the fuel-to-oxidizer ratio should be such that, adequate energy is generated in a self sustained fashion for the absolute decomposition of the fuel and metal precursor into cobalt oxide and gaseous products. The gaseous products of combustion include, CO_2, N_2 and water vapour. The maximum theoretical temperature achieved for Eqn.3.1 is evaluated from the thermodynamic properties of the reactants and the products, as listed in Table 3.1. If all the heat generated during the combustion reaction is utilized to heat the products without exchange of heat with its surroundings, the adiabatic flame temperature (T_{ad}), can be evaluated using Eqn.3.2, where n is the number of moles of species participating in the reaction, ΔH_f° is the enthalpy of formation, C_p is the heat capacity of products at constant pressure. In Eqn.3.2, room temperature is considered as the reference temperature ($T_\circ$=298 K). Consequently, a maximum adiabatic temperature of 1457 K is obtained for the combustion reaction of hexamethylenetetramine (HMTA) and $Co(NO_3)_2.6H_2O$.

$$27Co(NO_3)_2.6H_2O + 7C_6H_{12}N_4 \longrightarrow 9Co_3O_4 + 41N_2 + 204H_2O + 42CO_2 \quad (3.1)$$

$$-[\sum n(\Delta H_f^\circ)_{products} - \sum n(\Delta H_f^\circ)_{reactants}] = \int_{T_\circ}^{T_{ad}} (\sum nC_p)_{products} dT \quad (3.2)$$

Experimental determination of the maximum combustion temperature attained by the redox reaction resulted in 571 K, which is sufficient for complete decomposition of the metal precursor. The temperature-time profile for the HMTA and cobalt-nitrate redox reaction with an oxidizer to fuel molar ratio of 3.86 is shown in Fig 3.1. Clearly, two stages of combustion are observed. The first stage, observed from the reaction initiation at 421 K to 480 K, with a slope of 15 K/min, is due to the initiation of surface combustion reaction. The second stage, as observed from 480 K to a maximum temperature of 571 K, is accounted

Table 3.1: Thermodynamic data for evaluating adiabatic flame temperature

Compound	ΔH_f° **(kJ/mol)**	C_p **(kJ/(mol·K))** [a]
$Co(NO_3)_2.6H_2O$	-2212.26	-
$C_6H_{12}N_4$	120.56	-
Co_3O_4	891.0	0.123
H_2O	-241.76	0.034
N_2	0	0.021
CO_2	-393.51	0.037

[a]average C_p value

for the redox reaction of bulk NO^{3-} and the fuel. The temperature rises in this stage at a rate of 180 - 200 K/min. The entire combustion reaction resulting in the formation of cobalt oxides is completed in a short span of 10 minutes, as indicated by the hatched region in Fig 3.1.

The thermal events occurring in the course of the combustion reaction were recorded using a differential thermal and thermogravimetry analyser (DT-TGA). The DT-TGA curves for IWI and CS impregnated supports are shown in Fig 3.2. The redox reactions occur in the temperature range of 430 K - 520 K, where a total weight loss of 25% is observed. Region I for CS catalysts, as seen from 430 K to 455 K, shows 4.5% sample weight loss. The exothermic reactions that occur in this region correspond to the surface combustion of NO^{3-} and HMTA. In region II, observed from 455 K - 475 K, the sharp exothermic peak corresponds to the redox reaction of bulk NO^{3-} and HMTA. A maximum weight loss of 16% is observed in this region. The weight loss observed in region III is due to the redox reaction of residual fuel-oxidizer mixture, as observed from 476 K to 521 K, accounting for 5% sample weight loss. The thermal behaviour observed for IWI catalysts shows a broad weight loss region with an endothermic decomposition of $Co(NO_3)_2.6H_2O$, resulting in the formation of Co_3O_4. The weight loss curve for CS catalysts shows clearly that the selected stoichiometry produces enough heat for decomposition of cobalt nitrate resulting in the formation of supported

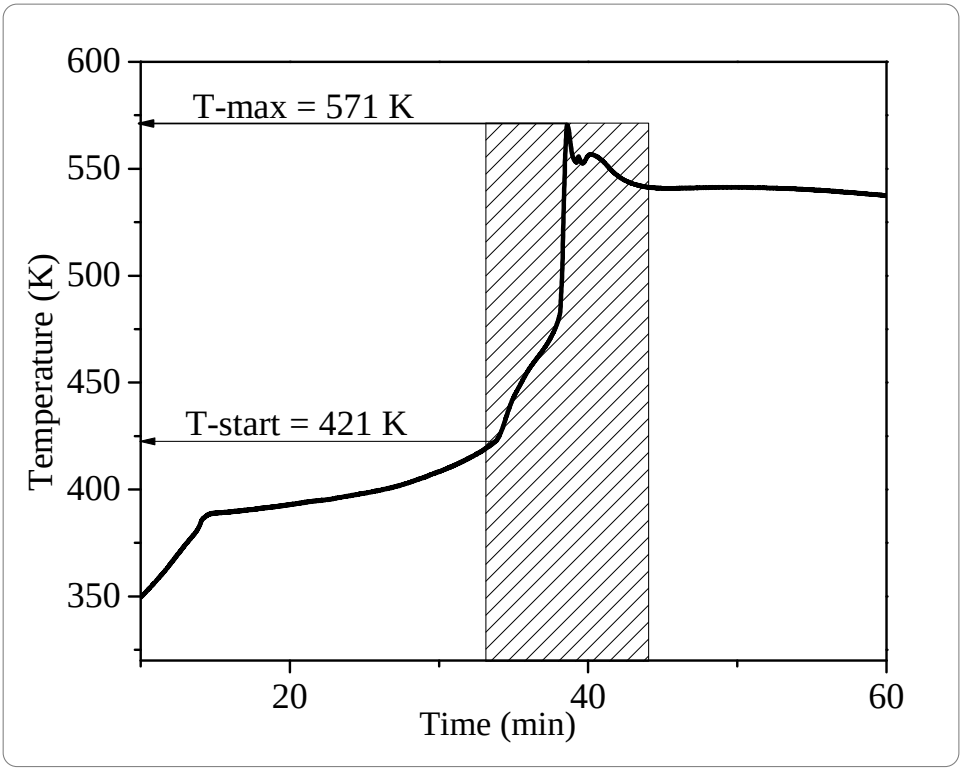

Figure 3.1: Temperature time profile for $C_6H_{12}N_4$-$Co(NO_3)_2.6H_2O$ reaction

Co_3O_4.

The Fourier transform infrared spectroscopy of the HMTA-cobalt nitrate mixture and the calcined CS catalysts were analyzed to investigate the nature of the redox complex and to examine the completion of the combustion reaction. The FT-IR spectra of the impregnated redox mixture and the calcined CS catalysts are shown in Fig 3.3. The FT-IR spectrum here, is a plot of percentage transmittance (%T) and wavenumber (cm^{-1}). As seen in Fig 3.3, the broad peak observed at 3352 cm^{-1} implies the presence of moisture, due to the O-H stretching mode [Gerakines et al., 1994]. The sharp peak observed at 1360 cm^{-1}, corresponds to the symmetric stretching of monodentate NO^{3-} ion. Further observation reveals the splitting of this band 1313 cm^{-1} and 1296 cm^{-1}. The split band spectra evidences the coordination of HMTA to the cobalt ion [Agwara et al., 2011]. Combustion synthesized metal oxides by Prakash et al. [2002], reported a HMTA is a tetradentate ligand, that forms complexes with metal ions and act as combustion precursors to complex metal oxides. The medium intensity peak identified at 819 cm^{-1} corresponds to the vibration spectra occurring due

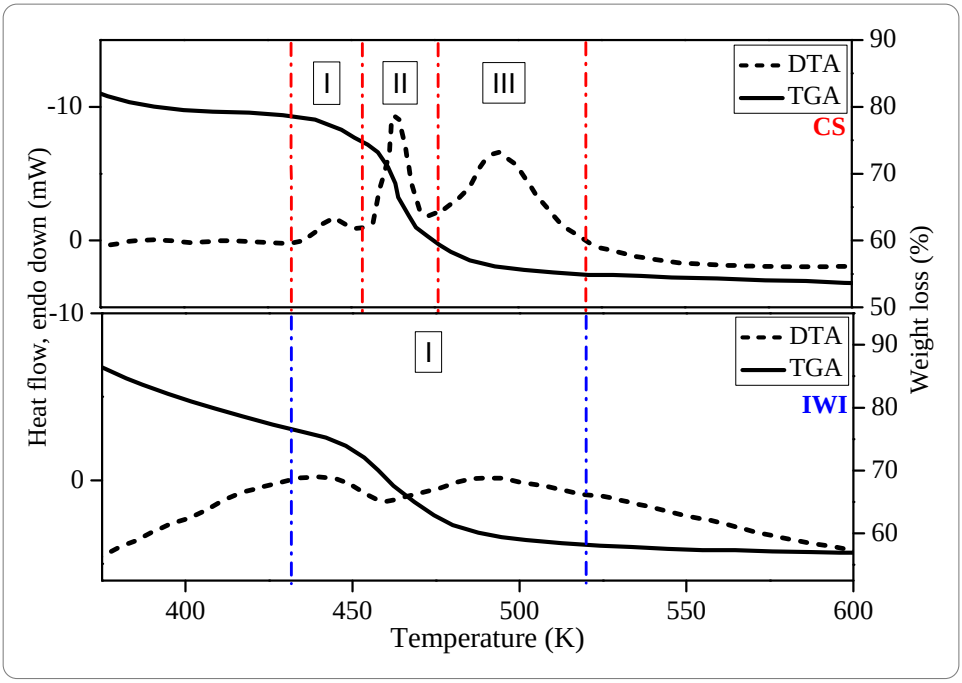

Figure 3.2: Simultaneous thermogravimetric and differential thermal analysis for CS and IWI catalysts

to the rocking vibrations of the CH_2 group. The FT-IR spectrum of CS calcined catalysts, the absence of the cobalt precursor and the HMTA functional groups, indicate the completion of redox reaction, further supporting the complete combustion for the selected stoichiometry without the presence of any combustion residues.

Table 3.2 shows the surface area of the synthesized alumina catalysts. Cobalt loading reduces the active surface area due to the fraction of support pores occupied by the cobalt oxide crystals. The catalysts synthesized with equivalence ratio of ϕ=1.2 and ϕ=1.5 show slightly lower surface area. The reduced surface area could be attributed to the carbon coverage of the support pores under fuel rich conditions.

3.1.2 Temperature programmed reduction and desorption (TPR/D)

The TPR experiments provide the reduction temperatures for the synthesized catalysts. Simultaneously, the concentration of H_2 consumed during the

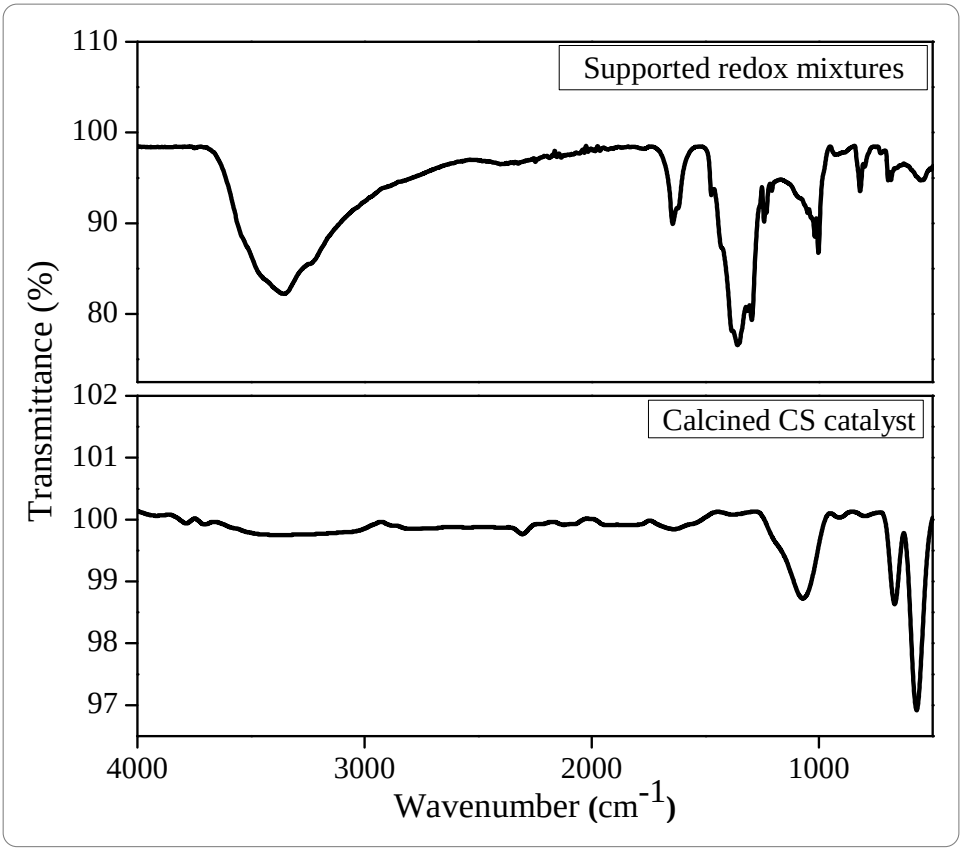

Figure 3.3: FT-IR spectra of the supported redox precursors and calcined CS catalysts

Table 3.2: Surface area of the synthesized catalysts

Catalyst	**BET surface area (m^2/g)**
Al_2O_3	158
Al_2O_3 - IWI	124
Al_2O_3 - CS (ϕ=1.0)	127
Al_2O_3 - CS (ϕ=1.2)	120
Al_2O_3 - CS (ϕ=1.5)	116

reduction process is obtained as a function of the recorded TCD signal, using a level calibration. As a result, the area under the concentration-temperature curve generates the hydrogen consumed, yielding fraction of cobalt oxide converted to

zero valent cobalt. Fig 3.4 shows the reduction profile for the synthesized catalysts. It is evident from the figure that the combustion synthesized catalysts result in elevated reduction temperatures, compared to IWI catalysts. For IWI supported catalysts, the H_2 reduction peaks are observed at 581 K and 804 K. The two peaks correspond to the twin step reduction of Co_3O_4 to Co^0 ($Co_3O_4 \longrightarrow CoO \longrightarrow Co^0$). In the case of combustion synthesized catalysts, the reduction peaks obtained at higher temperatures correspond to the reduction of different phases of cobalt oxides at varying temperatures.

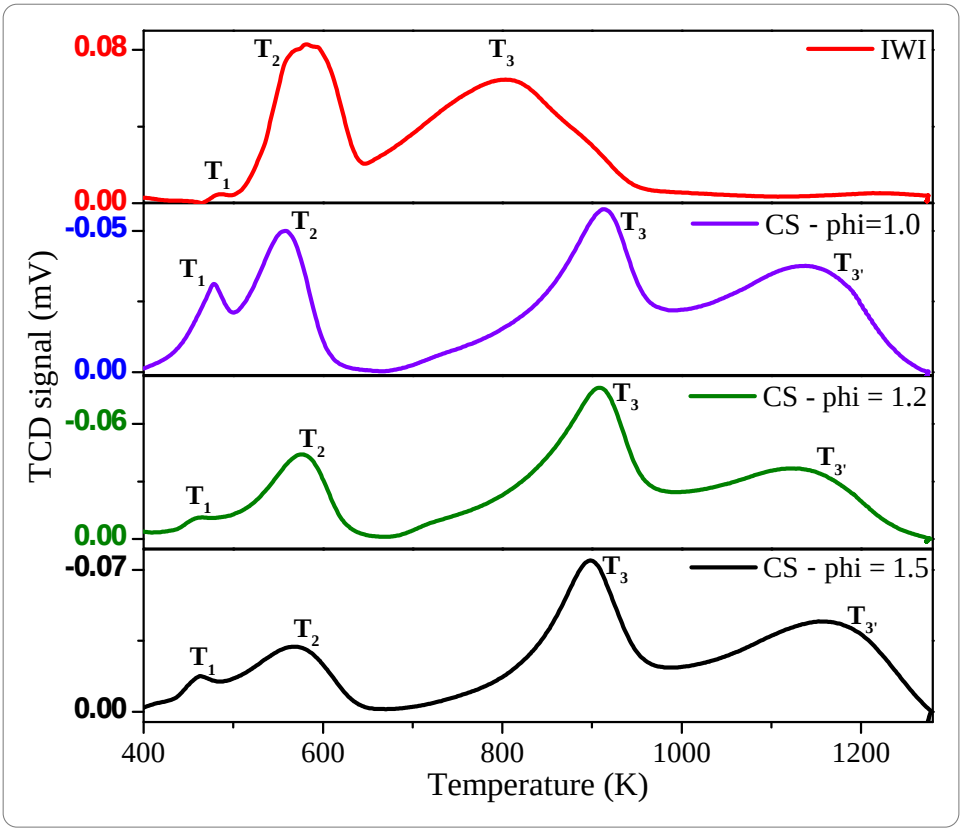

Figure 3.4: TPR spectra of IWI and CS catalysts
[*phi=1.2 and phi=1.5 are the catalysts synthesized by CS method in fuel rich conditions, with equivalence ratio of 1.2 and 1.5 respectively*]

The reduction of distinct phases of cobalt oxides formed on the surface of γ-Al_2O_3 supports were explained by Arnoldy and Moulijn [1985], where four stages of reduction temperatures were recorded corresponding to the four different phases of cobalt oxides formed on the alumina surface. The reduction temperatures for these phases were identified using their bulk standards. Fig

3.6 shows the TPR patterns for bulk cobalt-alumina compounds [Arnoldy and Moulijn, 1985]. A detailed comparison of Fig 3.4 with Fig 3.6 and Fig 3.5 gives an useful insight into the oxidation states of cobalt and cobalt alumina compounds formed on the catalyst surface. Phase-1 comprises of the twin step reduction of Co_3O_4 as explained earlier. This phase is marked in Fig 3.4 with T_1 and T_2, occurring similarly for all synthesized catalysts. Phase-2, as described by Arnoldy and Moulijn [1985], constitutes the reduction of Co^{3+} ions in the Co_3AlO_6 crystallites. This reduction peak occurs at 750K and, minimal H_2 uptake is observed at this temperature for CS catalysts, though some fraction of reduction degree is observed for IWI catalysts. Phase-3 is marked by the reduction of surface Co^{2+} ions, as observed at 900 K. A strong peak is seen at this temperature for the combustion synthesized catalysts (T_3 = 900 K - 915 K) indicating the the presence of surface Co^{2+} species. Further, for the combustion synthesized catalysts, the broad peak observed in the temperature range of 1120 K to 1160 K (marked $T_{3'}$) includes the reduction of surface or subsurface Co^{2+} ions in the Co^{2+}-Al^{3+} spinel structure. From the TPR profile observed in Fig 3.4, it is evident that the spinel structures continue to get reduced at temperature ranging from 1100 K to 1200 K. Form Fig 3.4 it is evident that H_2 consumption does not occur at temperatures above 950 K. However, the irreducible cobalt oxide species that reduce at temperatures above 1200 K have been described by Arnoldy and Moulijn [1985] and Schanke et al. [1995]. It is quite likely that the irreducible cobalt aluminate compounds are present in IWI synthesized catalysts, since these species exist in a stable form at low calcination temperatures [Patil et al., 2008].

The combustion synthesized catalysts, which include the catalysts synthesized with equivalence ratio of 1, 1.2 and 1.5 have similar TPR profiles, except that the H_2 consumption varies with the equivalence. This is a strong indication of varying degrees of reduction for the combustion synthesized catalysts. The reduction temperatures, the degree of reduction (DOR) and the metal dispersion (D) are shown in Table 3.3. As seen from the table, the degree of cobalt reduction and the metal dispersion are higher for combustion synthesized catalysts compared to IWI catalysts. DOR increases from 63.8% for IWI catalyst to 68.7% for CS catalysts synthesized with ϕ=1. Above all, the CS catalysts synthesized with ϕ=1.2 and ϕ=1.5, show an additional increase in DOR by 18% and 20% respectively. For equivalence ratio above 1.2, the fuel rich conditions most

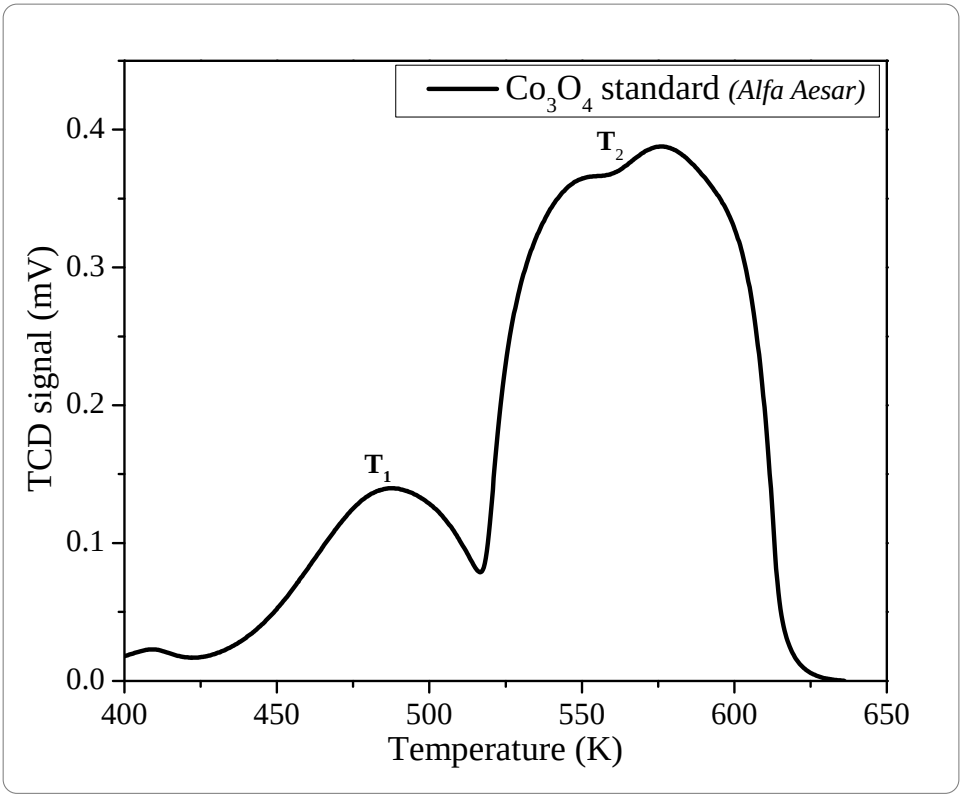

Figure 3.5: TPR profile of the standard Co_3O_4 sample
[*Co_3O_4 standard sample obtained from* Alfa Aesar, *subjected to TPR tests, under similar conditions are the IWI and CS catalysts*]

likely result in the formation of residual carbon which is likely to affect the FT reaction rates. The highest degree of reduction is attained for equivalence ratio of 1.5. Simultaneously, the metal dispersion, which is indicative of the fraction of active cobalt sites present on the catalyst surface is least for IWI catalysts (9.3%) and highest for CS catalysts with ϕ=1.5 (13.2%). Strikingly, higher degree of reduction and cobalt dispersion for CS catalysts is also attributed to the near to complete reduction of cobalt alumina species occurring on the catalyst surface, which exist in stable form over IWI catalysts.

3.1.3 X-ray diffraction

X-ray diffraction patterns for the calcined catalysts showed distinct peaks corresponding to Co_3O_4. Fig 3.7 shows the xrd spectra for the calcined and reduced IWI catalyst and CS catalyst synthesized with equivalence ratio 1. Sim-

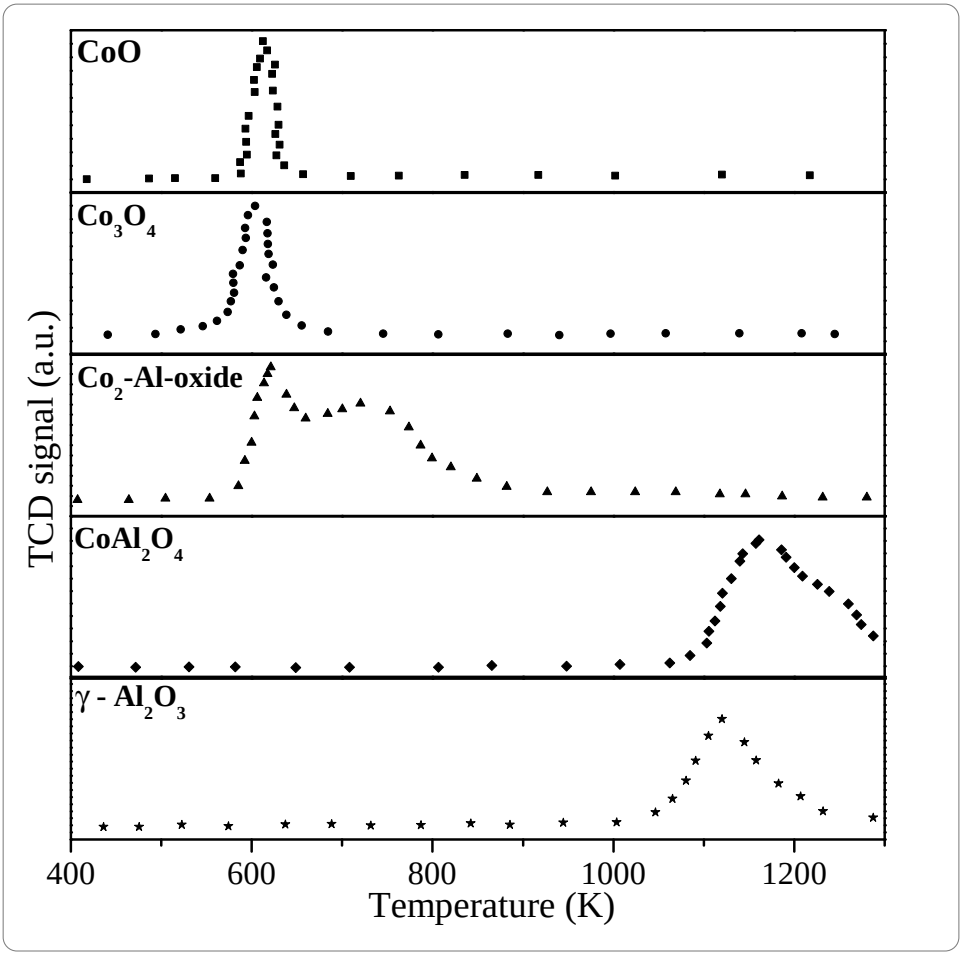

Figure 3.6: TPR patterns of the reference materials to correlate with the Co-alumina phases

[*Data extracted from Arnoldy and Moulijn [1985]*]

ilarly, Fig 3.8 shows the XRD spectra for combustion synthesized catalysts synthesized with equivalence ratio of 1.2 and 1.5. The 2-θ peaks recorded at 31.2°, 36.94°, 44.86°, 55.82°, 59.24° and 65.16° agree with the spectra of Co_3O_4 . Moreover, the peaks observed at 32.9°, 38.6° and 66.9° reveal the XRD spectrum of cobalt aluminate and alumina. The XRD spectrum of cobalt aluminate and alumina confirm with the spectrum recorded by O'NEILL [1994] *(ICSD-40029)* and Gutiérrez et al. [2001] *(ICSD-95302)*. The XRD spectra of reduced catalysts show sharp 2θ peaks at 44.2° and 51.5°, which correspond to metallic cobalt. In analysing the XRD spectra of cobalt-alumina support framework, it is found from the literature that, the 2θ peaks for Co_3O_4 and $CoAl_2O_4$ almost overlap. As a result, a conclusive claim for the presence of $CoAl_2O_4$ in the synthesized catalysts

Table 3.3: TPR-TPD summary

Catalyst	**Reduction temperatures**			**DOR**	**D**
	T_1 (K)	**T_2 (K)**	**T_3 (K)**	**(%)**[a]	**(%)**[b]
Co/Al_2O_3 - IWI	484	586	800	63.8	8.6
Co/Al_2O_3 - CS(ϕ=1)	480	554	915 ; 1140	68.7	10.9
Co/Al_2O_3 - CS(ϕ=1.2)	458	575	910 ; 1131	75.0	12.8
Co/Al_2O_3 - CS(ϕ=1.5)	458	566	898 ; 1160	76.8	13.2
Co_3O_4 Standard	512	574	-	-	

[a]from TPR H_2 uptake; [b]from H_2 TPD of reduced catalysts

is not reasonably attained by XRD analysis alone. Nevertheless, the presence of metallic cobalt is clear to indicate the formation of FT active metallic sites after the reduction process.

Table 3.4 shows the cobalt crystallite size for the synthesized catalysts. As seen from the table, the combustion synthesized cobalt catalysts have smaller crystallite size compared to the IWI catalysts. The crystallite size decreases from 15 nm to 10.5 nm for CS catalysts synthesized with ϕ=1, indicating a 43% reduction in the crystallite size for CS catalysts. Further, the catalysts synthesized with fuel rich conditions show even smaller Co_3O_4 crystallite sizes. The CS catalyst synthesized with ϕ=1.2, contains 7.3 nm sized cobalt oxides, and CS catalyst synthesized with ϕ=1.5 results in cobalt oxides with 6.6 nm. As mentioned earlier, any further increase in the equivalence ratio, results in the powdering of cobalt oxides, with considerable fraction of residual fuel and carbon deposits on the catalyst surface. The reduced crystallite sizes for CS catalysts, furthermore support the increased metal dispersion.

A possible reason to support the reduced crystallite size of combustion synthesized catalysts, is the time of calcination. As seen from Fig 3.1, the CS reactions are completed in a short span of 10 minutes. Above all, the molecular mixing of redox reactants throughout the support volume results in homogeneous distribution of metal-oxide across the support matrix. Contrastingly, the IWI catalysts need to be calcined for a duration of 3.5 to four hours for the complete decomposition of metal precursor and the consequent formation of Co_3O_4. IWI

catalysts have agglomerated metal-oxide formation on the support surface leading to non-homogeneity in the particle distribution, and hence larger crystallite size and reduced metal dispersion.

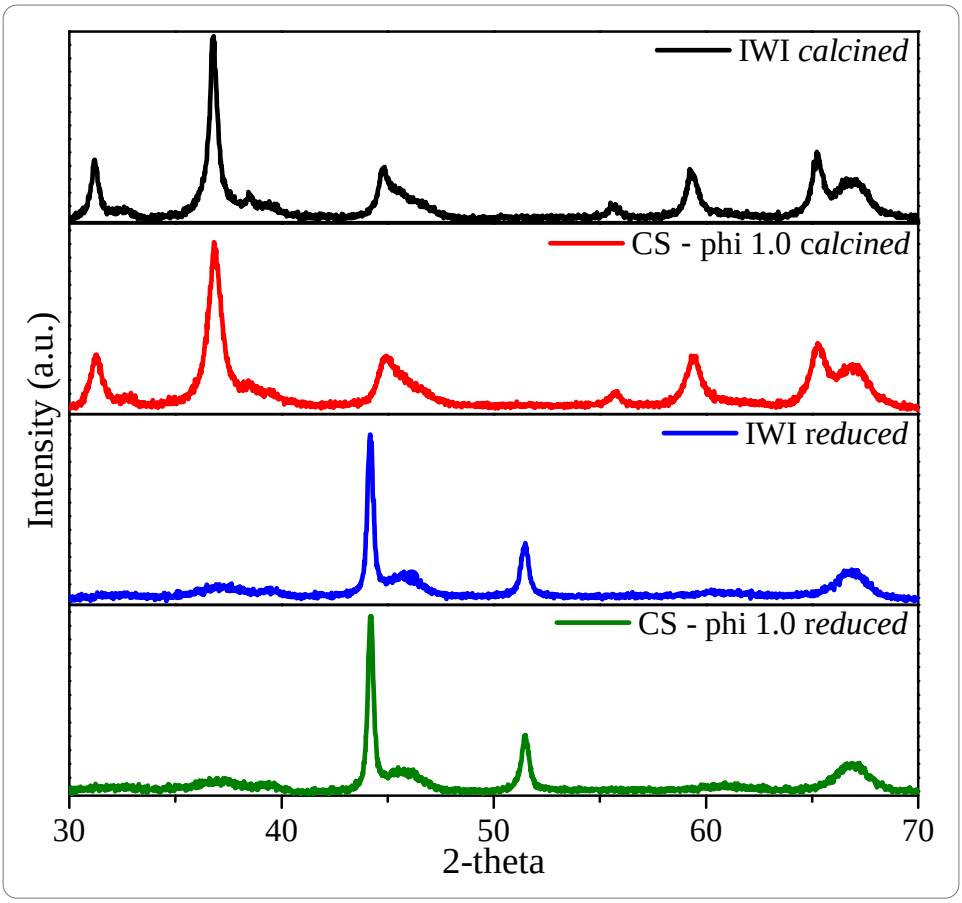

Figure 3.7: XRD spectra of Al_2O_3 supported cobalt catalysts synthesized by IWI method and CS method with equivalence ratio of 1

3.1.4 X-ray photoelectron spectroscopy

XPS spectra of the Co_3O_4 powder, as shown in Fig 3.9, was used to distinctly identify the binding energy of the Co^{+3} and Co^{+2} oxidation states, since Co_3O_4 is a mixed valence compound containing both Co(II) and Co(III) oxidation states. Deconvolution of the XPS spectra enables the identification and quantification of the cobalt oxide phases occurring on the catalyst surface. The spectral mapping of the high resolution elemental spectra is obtained by Gaussian curve fitting routine, and the corresponding binding energy reference was obtained from the

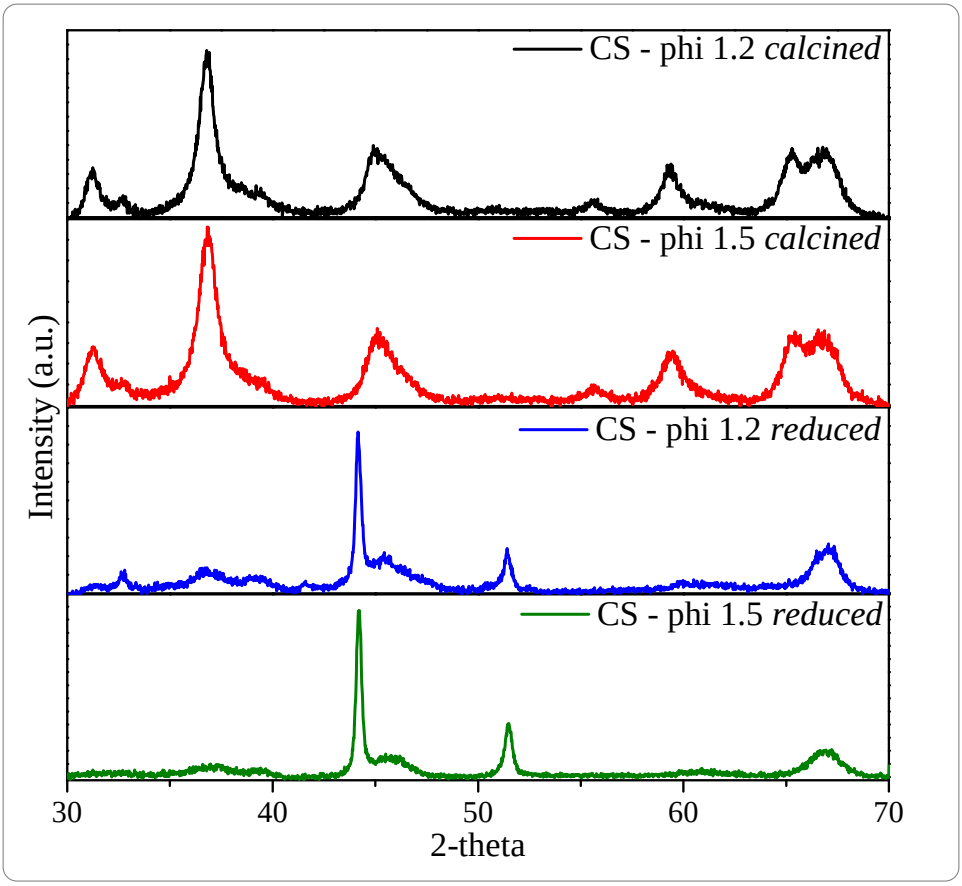

Figure 3.8: XRD spectra of Al_2O_3 supported cobalt catalysts synthesized by CS method with equivalence ratio of 1.2 and 1.5

Table 3.4: Crystallite sizes of the calcined Al_2O_3 supported catalysts

Catalyst	**Crystallite size (nm)**
Al_2O_3 - IWI	15.0
Al_2O_3 - CS (ϕ=1.0)	10.5
Al_2O_3 - CS (ϕ=1.2)	7.3
Al_2O_3 - CS (ϕ=1.5)	6.6

NIST database [Naumkin et al., 2008]. The component at 779.9 eV, for the deconvoluted spectra is referenced to Co_3O_4 and the second low intensity peak

at at 781.8 eV corresponds to CoO. The satellite peak observed at 785.8 eV are indicative of CoO, and occur due to the charge transfer band structure, assigned to the late 3d transition metal oxides [Carson et al., 1996]. Fig 3.10 and Fig 3.11 show the XPS spectra of the calcined catalysts. A comparison of the deconvoluted XPS spectra of the calcined catalysts with the standard powder reveals the occurrence of Co_3O_4 as the most dominant phase in the IWI and CS catalysts. XRD of the synthesized catalysts too reveal Co_3O_4 as the dominant phase.

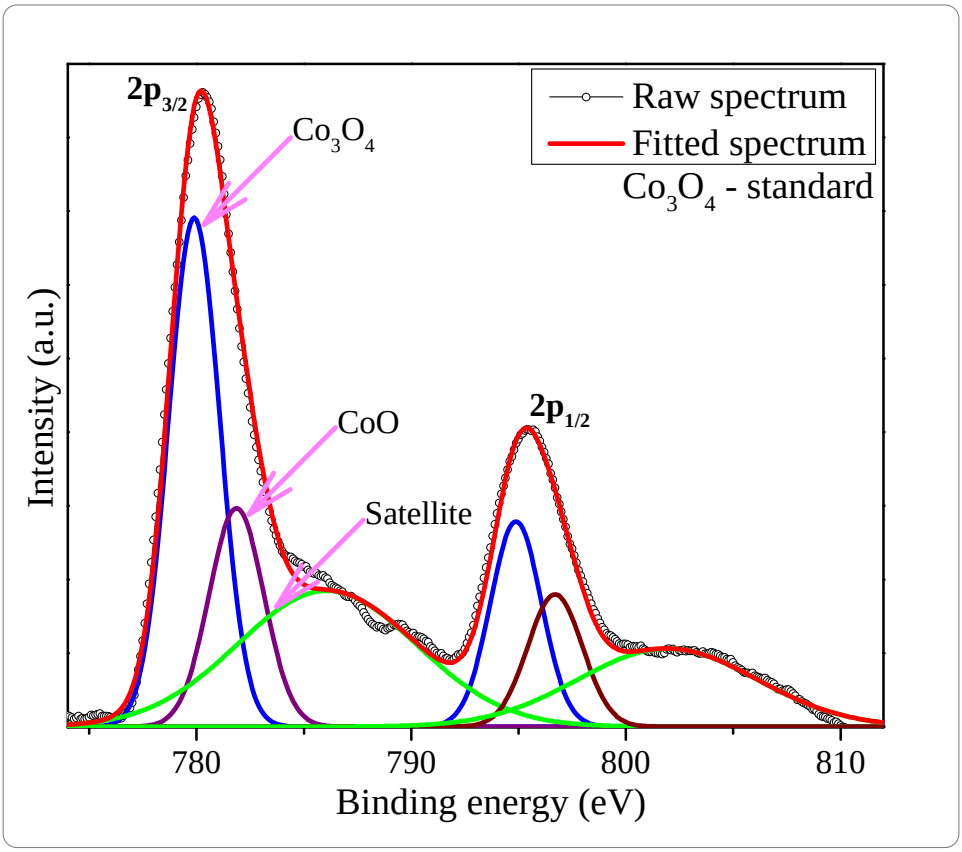

Figure 3.9: De-convoluted XPS spectrum of standard Co_3O_4 standard

The nature of the metal support interaction can be substantially obtained from the intensities and the binding energy values of the satellite peaks. A higher concentration of the cobalt aluminates is indicated by the higher intensity of the shake-up satellites. This is because, $CoAl_2O_4$ has characteristics of strong shake-up satellites and has binding energies 6 - 7 eV higher than the main peak. Ji et al. [2000] and Zsoldos et al. [1991] reported stronger satellite intensities, arising due to CoO and $CoAl_2O_4$ and thus specifying a stronger metal support

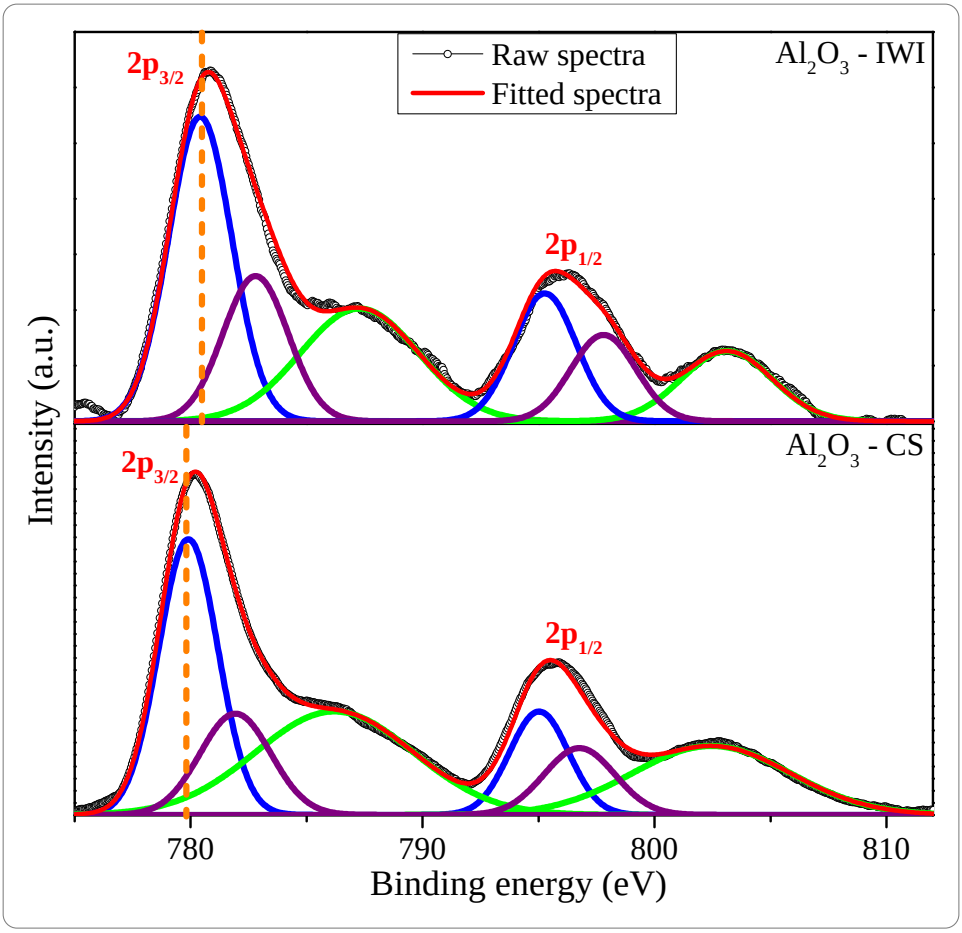

Figure 3.10: XPS spectrum of Al_2O_3 supported cobalt catalysts synthesized by IWI and CS method

interaction. The Co_3O_4 is the most dominant cobalt surface phase for weak metal support interaction and for strong metal support interaction, CoO and $CoAl_2O_4$ are the most dominant cobalt surface phase. Moreover, the reducibility of the synthesized catalysts decrease with the increased concentrations of CoO and $CoAl_2O_4$. Table 3.5 summarizes the binding energy of the cobalt oxides and the ratio of the intensities of the Co_3O_4 and the satellite peak. Combustion synthesized catalysts reveal reduced metal support interaction compared to IWI catalysts. Furthermore, the catalysts synthesized with equivalence ratio of 1.2 and 1.5 indicate additionally reduced formation of cobalt aluminates. This is evident from the higher degree of reduction of the CS catalysts in comparison to IWI catalysts. The measure of the cobalt dispersion is obtained from the Al and Co peak intensity ratios. Increasing intensity ratios indicate higher cobalt

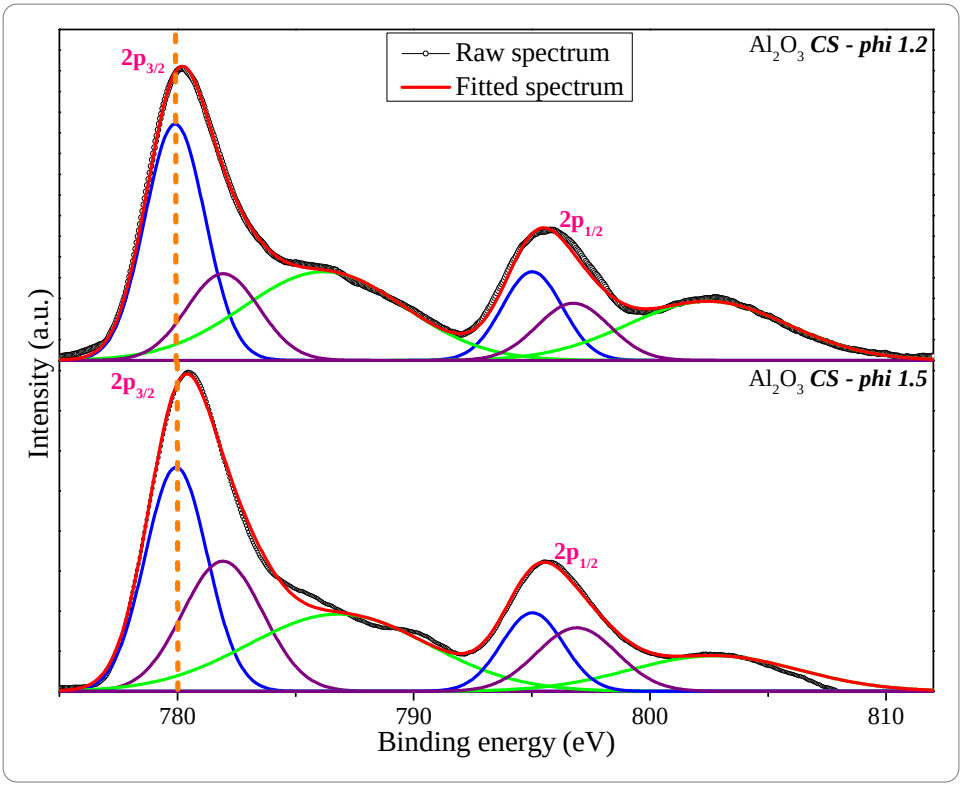

Figure 3.11: XPS spectrum of Al_2O_3 supported cobalt catalysts synthesized by CS method with equivalence ratio of 1.2 and 1.5

dispersion, revealing lower metal agglomeration. As seen in Table 3.5, a highest dispersion is obtained for CS catalysts synthesized with equivalence ratio of 1.5. The percentage metal dispersion obtained from H_2 TPR-TPD experiments agrees with the value obtained from XPS analysis for this catalyst, evidencing the lowest metal support interaction for CS catalysts synthesized under fuel rich conditions with ER equal to 1.5. The metal dispersion, as observed from XPS spectral analysis, decreases in the following order, Co-Al_2O_3 -CS ($\phi = 1.5$) > Co-Al_2O_3 -CS ($\phi = 1.2$) > Co-Al_2O_3 -CS ($\phi = 1.0$) > Co-Al_2O_3 -IWI, further signifying that the combustion synthesized catalysts result in higher degree of reduction, higher metal dispersion and consequently, larger number of active metal sites for the FT reaction.

Table 3.5: XPS summary

Catalyst	B.E. Co-$2p_{3/2}$ (eV)	spin-orbital splitting (eV)	$I_{Co2p3/2}/I_{sat}$	$\mathbf{I_{Co}/I_{Al}}$
Al_2O_3 - IWI	780.4	15.2	0.7	**0.2**
Al_2O_3 - CS (ϕ=1.0)	779.9	15.2	0.9	**1.1**
Al_2O_3 - CS (ϕ=1.2)	779.9	15.2	1.1	**1.2**
Al_2O_3 - CS (ϕ=1.5)	780.0	15.1	1.2	**1.8**
Co_3O_4-std	*779.9*	*15.0*	*1.8*	-

3.2 Fischer Tropsch reaction

The effect of synthesized catalysts on the FT reactions is shown in Fig 3.12, where the activity and selectivity measurements were averaged over a duration of 160 hours of operation. Fig 3.13 shows the variation of FT activity measured as as the rate of CO consumption per unit mass of catalyst. Combustion synthesized catalysts greatly enhance the FT activity and hydrocarbon selectivity, resulting in higher CO conversion and C_{5+} selectivity compared to IWI catalysts. Highest CO conversion is recorded for catalysts synthesized with equivalence ratio of 1.2. A two fold increase in the CO conversion is seen for CS(ϕ=1.2) catalysts as compared to IWI catalysts. However, only a marginal variation in recorded in the C_{5+} and CH_4 selectivity for the four catalysts. The selectivity for C_2-C_5 hydrocarbons is higher for CS catalysts synthesized with ER of 1.2 and 1.5. The increased performance of CS catalysts is attributed to its reduced cobalt crystallite size, increased degree of reduction and higher metal dispersion.

More importantly, the higher fraction of active sites over the CS catalysts are indicative of reduced fraction of cobalt aluminates that are inactive to the FT reaction. The metal dispersion for IWI synthesized catalysts are 48% lower than CS catalysts resulting in reduced active metal sites for syngas adsorption. Varying the equivalence ratio from 1 to 1.5, reduced the cobalt crystallite size 10.5 nm to 6.6 nm and increased the metal dispersion from 10.9% to 13.2%. Despite higher dispersion and reduction degree for CS(ϕ=1.5) catalysts, the CO conversion and the FT activity were lower compared to CS(ϕ=1.2) catalysts. The CO conversion rates reduced from 3.75 $mol_{CO}/(g_{cat}\cdot s)$ for CS(ϕ=1.2) to 2.87 $mol_{CO}/(g_{cat}\cdot s)$ for CS(ϕ=1.5) catalysts, indicating a 31% reduction with an

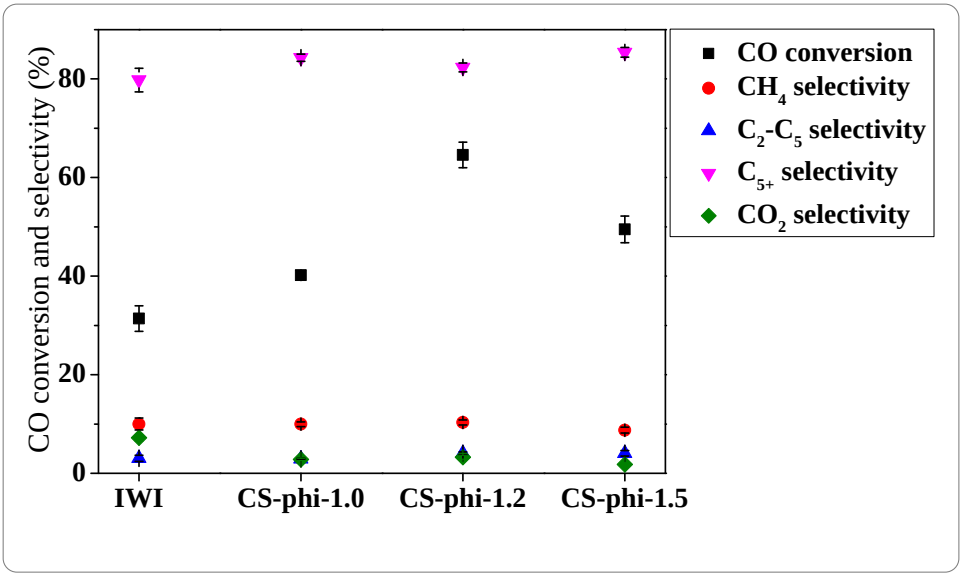

Figure 3.12: CO conversion and selectivity for the synthesized Al_2O_3 supported catalysts

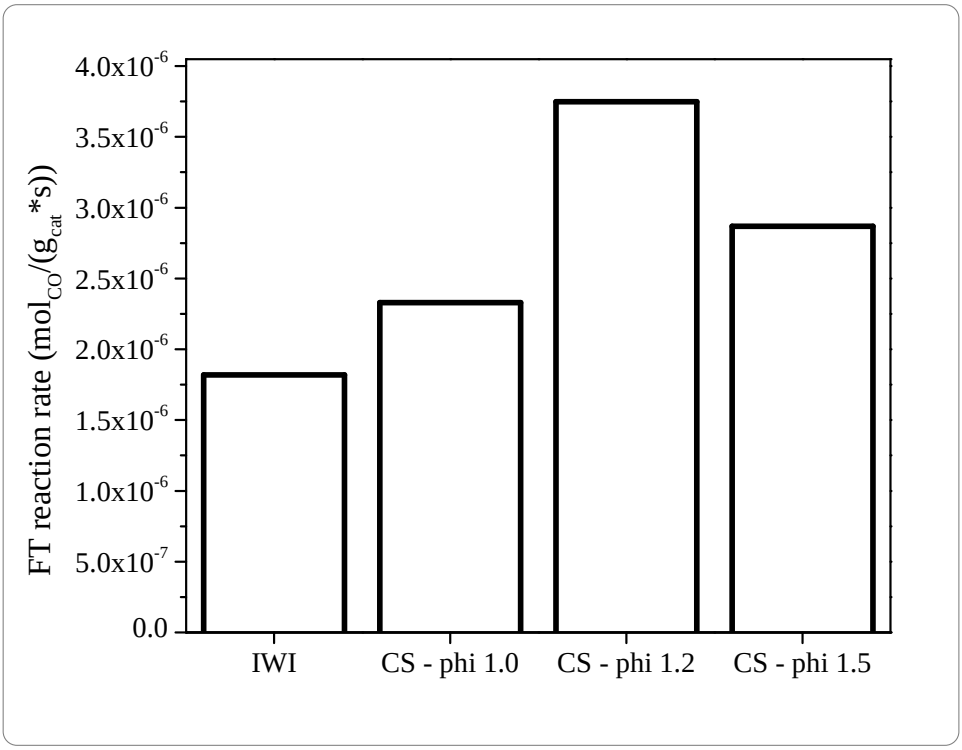

Figure 3.13: Measured FT reaction rate over IWI and CS catalysts

increasing equivalence ratio. A possible reason that may explain such a reduction in the FT activity is the accumulation of carbonic residues on the surface of the CS(ϕ=1.5) catalysts. Subsequently, the residual surface carbon species increase the resistance to syngas diffusion by blocking the support pores and reducing the overall active surface area. This lowers the apparent CO conversion rates, despite smaller crystallite size and reduced metal dispersion. The variation in CO conversion and the hydrocarbon selectivity with time on stream (TOS) is shown in Fig 3.14 and Fig 3.15. The FT activity and selectivity were measured after a stabilization period of 24 hours. The initial FT activity remained steady for a duration of 60 hours. Thereafter, a reduction in the FT activity was observed for CS(ϕ=1.2) and CS(ϕ=1.5) catalysts, though the CO conversions sustain at 61% and 43% respectively. The IWI catalysts, display a wide range of stabilization period with the CO conversion increasing from 23% to 34% over 160 hours of operation. For CS(ϕ=1.5) catalysts, the CO conversions remain steady at 40% over the entire span of operation.

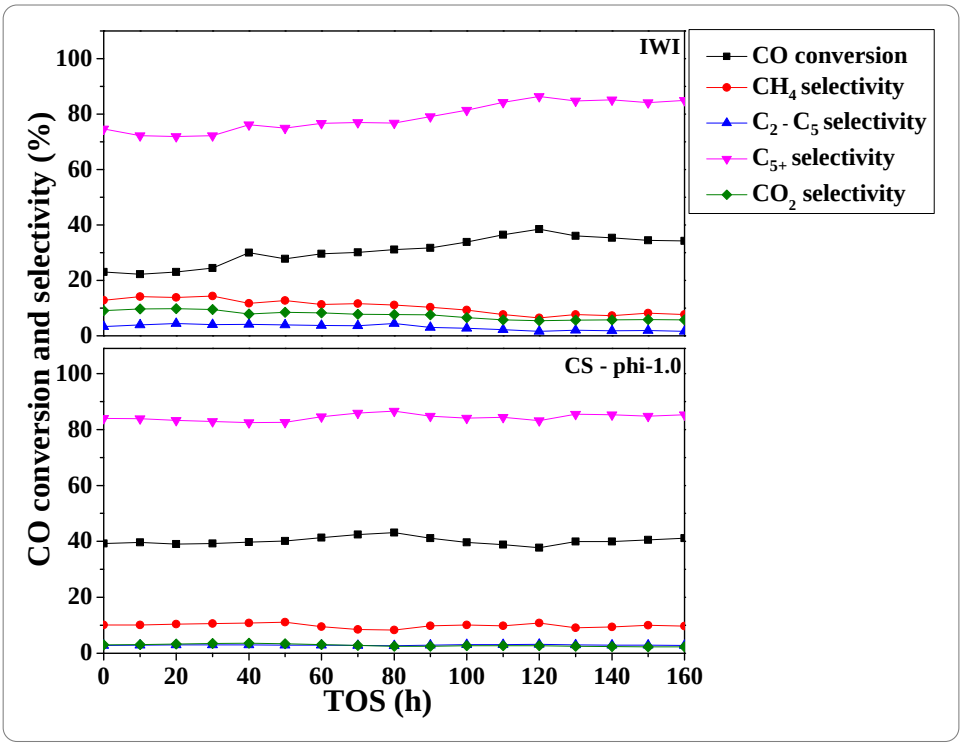

Figure 3.14: Variation in the FT activity for IWI and CS(ϕ=1.0) catalysts

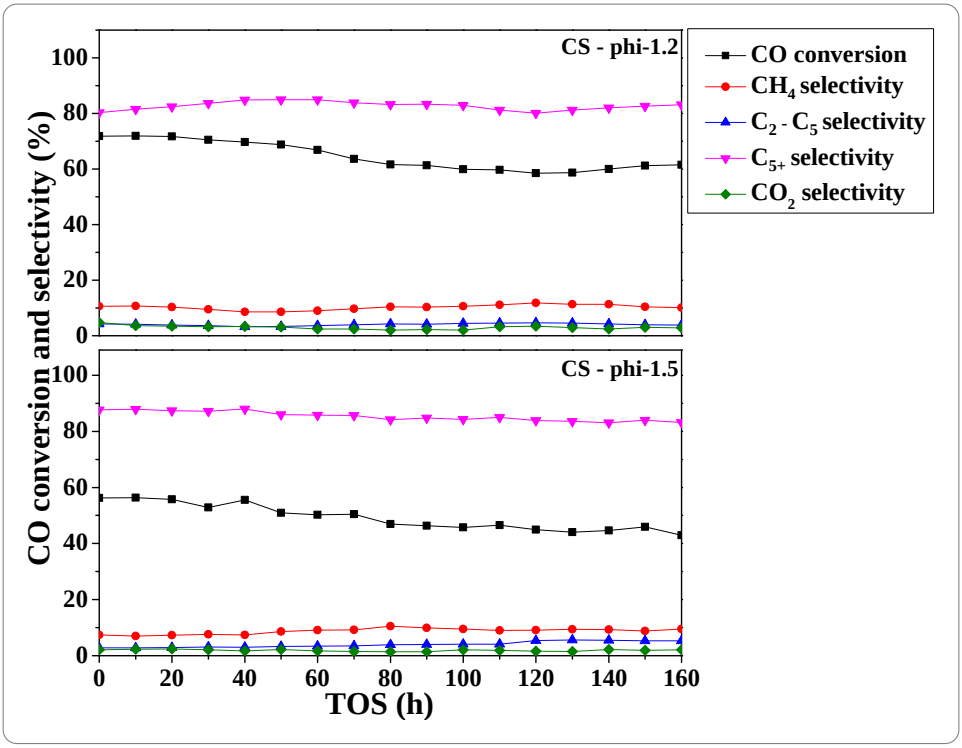

Figure 3.15: Variation in the FT activity for CS(ϕ=1.2) and CS(ϕ=1.5) catalysts

3.2.1 Product spectrum

The catalyst synthesis method has a considerable effect on the FT product spectrum. Fig 3.16 and Fig 3.17 show the variation in the liquid hydrocarbons (C_{10}-C_{24}) and heavier waxes (C_{24+}). The hydrocarbon products with CS(ϕ=1) catalysts predominantly yield heavier waxes compared to liquid hydrocarbons. The magnitude of active sites deposited over the supported catalysts and the degree of reduction are crucial factors that dictate the catalyst response for FT reaction. The product distribution spectrum indicates that the hydrocarbon chain growth probability is highest for CS(ϕ=1) catalyst, essentially due to the increased metal dispersion and higher catalyst reducibility. However, despite the increased reduction degree, reduced crystallite size and higher metal dispersion, the formation of waxes with CS(ϕ=1.2) and CS(ϕ=1.5) catalysts is considerably lower. A possible explanation for this is that the cobalt crystallite sizes for these catalysts are considerably smaller for longer chain growth propagation, resulting in the formation of middle distillates. Another possible reason can be attributed to the presence of carbon on the catalyst surface for catalysts synthesized under

fuel rich conditions. The carbon residues can alter the rate of syngas adsorption and the rate of re-adsorption of the products that can affect the extent of secondary reactions or the chain growth probability. The C_{24+} weight fraction for CS(ϕ=1.2) and CS(ϕ=1.5) catalysts are 69% and 77% lower than CS(ϕ=1) catalysts. Further, the weight fraction hydrocarbons in the range of C_6-C_{24} are almost negligible (0.01 wt.%) for CS(ϕ=1) catalysts. Fig 3.18, shows the collected wax and middle-distillates with the CS(ϕ=1) catalysts.

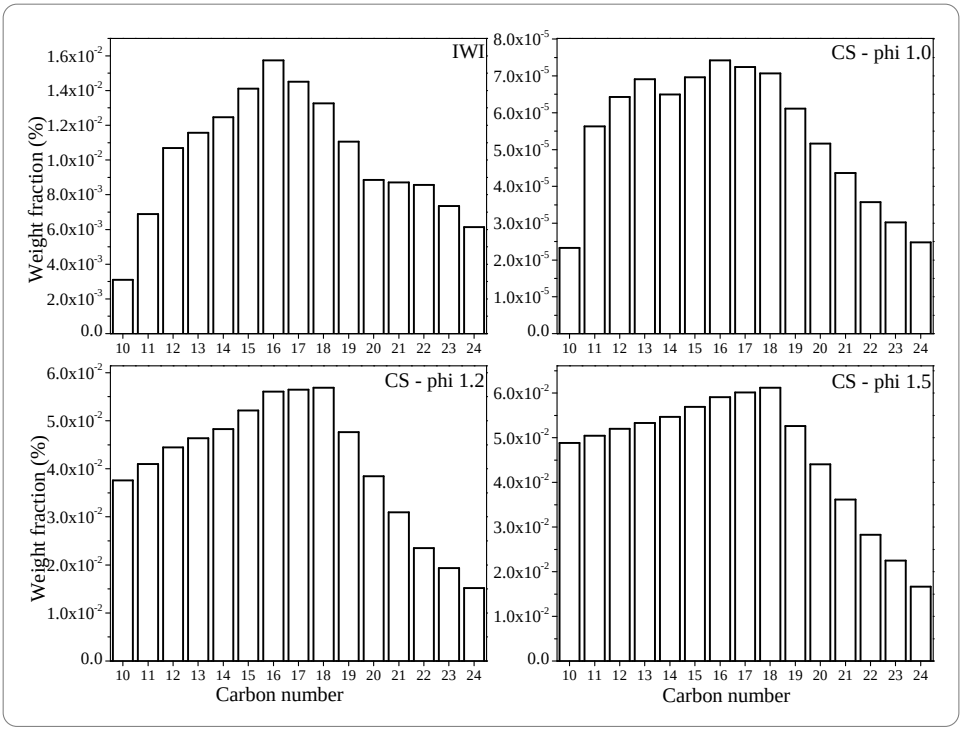

Figure 3.16: C_{10}-C_{24} hydrocarbons weight fraction for the synthesized catalysts

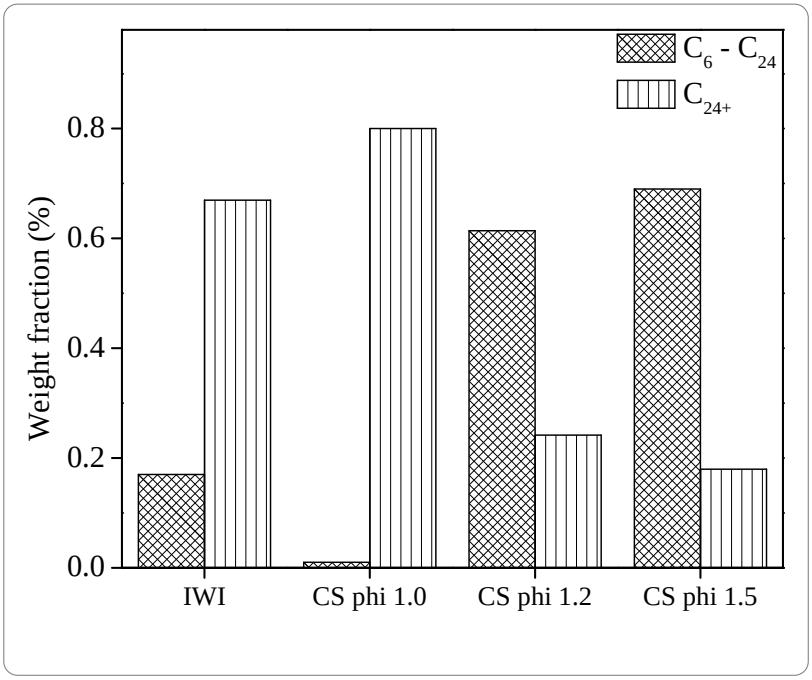

Figure 3.17: Variation in the liquid hydrocarbon and waxes weight fraction

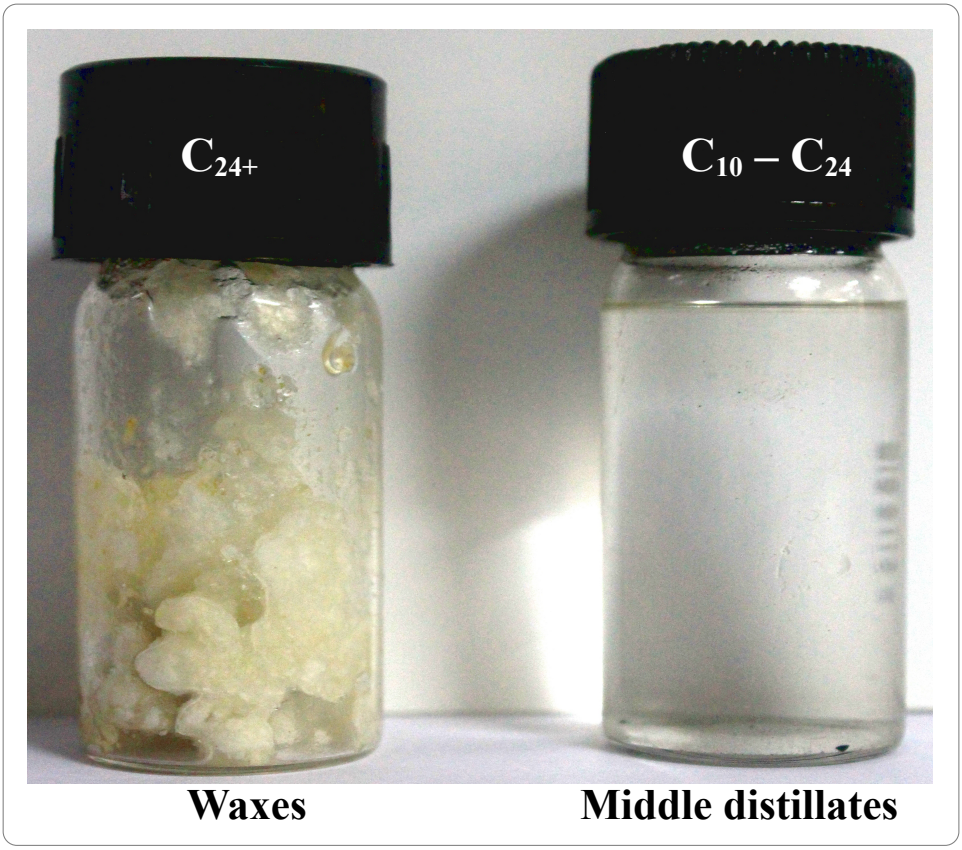

Figure 3.18: The collected wax and C_{10}-C_{24} fractions

3.3 Summary

This chapter has presented the utilization of an effective method to develop combustion synthesized cobalt catalysts for Fischer Tropsch reaction. The properties of the combustion synthesized (CS) catalysts are compared with the conventionally synthesized incipient wetness impregnation (IWI) catalysts. The synthesis method described in this chapter can be used for any metal support framework, with any metal loading and over support extrudes of varying size and shapes (pellets, spheres, monoliths, powders). In this chapter combustion synthesized supported cobalt catalysts were developed with metal loading of 20%, deposited over Al_2O_3 shperes, without affecting the structural integrity of the support material.

Hexamethylenetetramine (HMTA) was used as the fuel for the synthesis of Co_3O_4 on alumina spheres and cobalt nitrate hexahydrate was used as the metal precursor. Stoichiometry of the redox mixture was determined. The composition of redox solution required for combustion synthesis of cobalt oxide was derived from the oxidizing and reducing valencies of oxidizer and fuel. The reducing species included C, H and Co with valencies of +4, +1 and +2 respectively, and the oxidizing specie included O_2 with a valency of -2. To obtain maximum reaction temperature, the stoichiometry is selected such that the equivalence ratio (ER) is unity (ϕ_e=1). An insight into the nature of redox complex, indicated the coordination of HMTA to the cobalt ion. The FTIR spectra of the redox mixture revealed that HMTA, which is a tetradentate ligand, complexes with metal ions and acts as a combustion precursor for the complex metal ions. Simultaneously, catalysts were synthesized under fuel rich conditions with ER = 1.2 and ER = 1.5. The fuel rich synthesis conditions were adapted to obtain catalysts with cobalt catalysts in zero valent state rather than its oxide state. For ER > 1.5, powdering of catalysts were observed.

XRD analysis of the synthesized catalysts showed the presence of Co_3O_4 as the dominant phase. This was true even for catalysts synthesized with equivalence ratio of 1.2 and 1.5. Strikingly, the CS catalysts had reduced Co_3O_4 crystallite size that decreased in the following order : IWI > CS(ϕ=1) > CS(ϕ=1.2) > CS(ϕ=1.5). The H_2 chemisorption experiments evidenced higher reduction temperatures for the CS catalysts compared to IWI catalysts. A comparison of the TPR profiles of the synthesized catalysts with the Co-Al_2O_3 standards in the

literature showed the presence of surface or subsurface Co^{2+} ions in the Co^{2+}-Al^{3+} spinel structure, which continue to get reduced at temperatures above 1000 K. However, it is evident from the literature that, the irreducible cobalt species occur in cobalt-alumina framework which occur in a stable form at low synthesis temperatures. The degree of cobalt reduction and the metal dispersion increase in the following order IWI < CS(ϕ=1) < CS(ϕ=1.2) < CS(ϕ=1.5)

The FT activity of the synthesized catalysts showed highest activity for CS catalysts. Moreover, for CS(ϕ=1) catalysts, the FT product spectrum revealed a maximum weight fraction of wax hydrocarbons (C_{24+}), indicating higher degree of surface polymerization for this catalyst. Though highest syngas conversion was achieved for CS(ϕ=1.2) catalyst, the formation of waxes reduced with the increasing ER. The reduced degree of surface polymerization for these catalysts could be attributed to the reduced formation of cobalt crystallites which do not favour the formation of longer chain hydrocarbons and also to the presence of surface carbon species which hinder the secondary reaction rates.

Chapter 4

Silica-doped-alumina supported cobalt catalysts : Influence of support on FT reaction

In the earlier chapter it was observed that for alumina supported cobalt catalysts the formation of cobalt-alumina compounds, notably cobalt aluminates, resulted in the strong metal support interaction which reduce the degree of reduction to metallic cobalt. The reduced reduction degree decreases the FT activity. In this chapter, catalysts are synthesised on silica-doped-alumina supports. The effect of metal support interaction and its consequent effect on the FT activity and hydrocarbon selectivity are investigated.

4.1 Earlier literature

Several catalyst supports like Al_2, SiO_2, TiO_2 and carbon nanotubes have been investigated in the literature for its effect on FT activity. Though the primary purpose of a catalyst support is to increase the total active surface area available for the adsorbing reactants, the dispersed metal usually display varied degree of affinity for the support. γ-Al_2O_3 have been used exclusively for dispersing FT active metals. Jacobs et al. [2002] in their work reported that though γ-Al_2O_3 supported cobalt catalysts are more difficult to reduce compared to SiO_2 or TiO_2 supported Co catalysts, the availability of active surface sites is much higher for Al_2O_3 supported catalysts, particularly due to the stabilization of small cobalt cluster size.

More recently, several researchers have investigated the properties of FT

active metals supported over silica-doped-alumina (SDA). The catalysts characterized by Jean-Marie et al. [2009] revealed that the addition of 5 wt.% SiO_2 in Al_2O_3 increases the degree of cobalt reduction by decreasing the formation of hardly reducible cobalt aluminate species. Reportedly, the CO conversion increased from 22% for Al_2O_3 supported cobalt catalysts to 26% for SDA supported cobalt catalysts. Keyvanloo et al. [2014] synthesized SDA supported Fe catalysts that resulted in high FT activity and excellent stability for FT synthesis. It was shown that addition of silica to Al_2O_3, enhances the thermal stability by suppressing the phase transformation of γ-Al_2O_3 to α-Al_2O_3, further enabling effective dehydroxylation of the Al_2O_3 surface at high temperatures. A major advantage of removing the hydroxyl groups is the reduction in the acidic sites and a consequential reduction of cracking of higher hydrocarbons to lighter hydrocarbons.

Daniell et al. [2000] investigated the variation in the surface acidity with the addition of SiO_2 to Al_2O_3 supports through the FTIR spectroscopy of adsorbed CO probed molecules. The surface acidity was investigated initially for pure γ-Al_2O_3 and then for silica doped alumina, with the silica concentration varying from 1.5 to 90 wt.%. The progressive addition of SiO_2 to Al_2O_3 resulted initially in the formation of mixed aluminosilicate phase consisting of both lewis and bronsted acidic sites. Addition of 30 wt.% SiO_2 resulted in the Al_2O_3 particles' encapsulation by SiO_2, indicating a silica enriched surface containing only phases of SiO_2 and aluminosilicates. With 40 wt.% SiO_2 doping in Al_2O_3, the fraction of exposed aluminosilicate sites reaches a maximum. Any further addition of SiO_2 resulted in zero lewis acidity and bronsted acidity equal to that of silica itself. Therefore, incorporation of SiO_2 (upto 40 wt.%) into the Al_2O_3 supports results in the formation of strong Lewis acid sites and a small quantity of highly acidic bronsted acid sites. Lewis acid sites are formed through the isomorphous substitution of tetrahedral Si^{4+} by Al^{3+} ions. The bronsted acid sites are similar to the ones formed in zeolite supports.

The SDA supported cobalt catalysts are synthesized by IWI and CS method, and the properties are compared Al_2O_3 supported cobalt catalysts. More importantly, the impact of support on the FT product spectrum is investigated and presented in the following sections.

4.2 Support characterization

The commercially obtained catalyst supports were characterized using FTIR, XRD and XPS. To draw a correlation of the nature of metal support interaction and the effect of support on the catalyst activity and selectivity, it is crucial to obtain the chemical information of the oxide supports.

4.2.1 Fourier transform infrared spectroscopy

The FT-IR spectrum of the SDA support is shown in Fig 4.1. The spectrum is typical of IR spectra of aluminosilicates. A sharp high intensity peak observed at 1063 cm^{-1} is assigned to the intense asymmetric stretching vibrations of Al-O-Al or Si-O-Si bonds Sharma et al. [2012]. The sharp band at 453.2 cm^{-1} is due to the Si-O bending vibrations. A sharp band at about 560 cm^{-1} and a comparably lower intensity band at 800 cm^{-1} are due to the Al-O-Si vibrations. The FT-IR spectrum also shows the Al-O stretching vibrations at 915 cm^{-1} Gangwar et al. [2015]. Overall, the FT-IR spectrum of SDA supports indicated an aluminosilicate type framework.

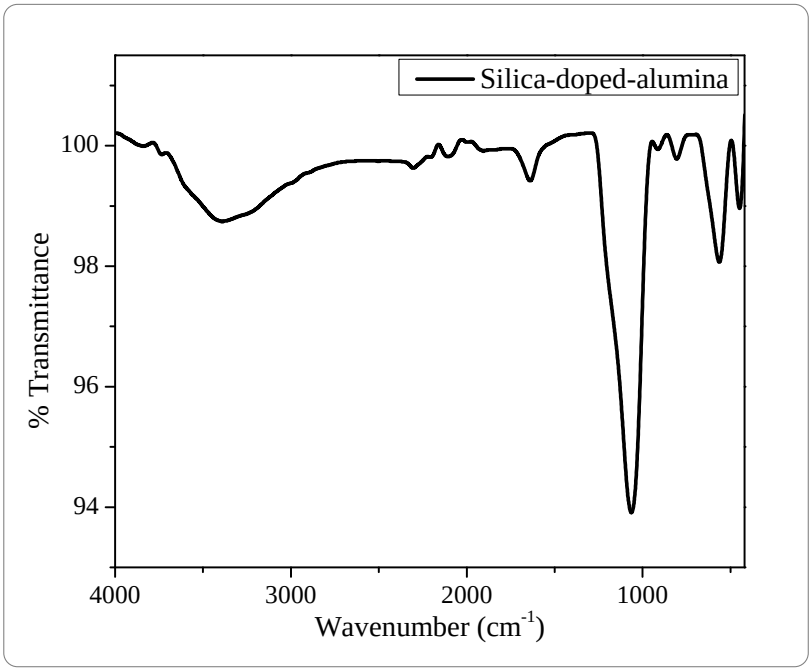

Figure 4.1: FT-IR spectrum of the silica-doped-alumina support

The FT-IR spectrum of SDA support is compared with the standard SiO_2

(*Alfa Aesar*) and γAl_2O_3 (similar to the support used in chapter three) supports. The FT-IR spectra of SiO_2 standard, as shown in Fig 4.2 shows the usual peaks of the SiO_2 framework [Pereira et al., 2011]. The high intensity peak at 1084.5 cm^{-1}, with a shoulder at 1225 cm^{-1} corresponds to the Si-O-Si asymmetric stretching. The low intensity band at 804 cm^{-1} is due to the Si-O-Si symmetric stretching, and the sharp band at 463 cm^{-1} corresponds to the Si-O-Si bending vibrations. Similarly, the FT-IR spectra for the alumina support, used in chapter three and shown in Fig 4.3, distinctly indicates γ-Al_2O_3 structure. The adsorption band at 825.62 cm^{-1} and 555 cm^{-1} are attributed to the Al-O-Al bending more and to Al-O stretching mode respectively [Gangwar et al., 2015]. The band at 1691 cm^{-1} corresponds to the H-O-H angle bending vibration band of weakly bound molecular water. A comparison the FT-IR spectra of the SDA supports with the SiO_2 and Al_2O_3 supports strongly indicates aluminosilicate type framework for the SDA supports.

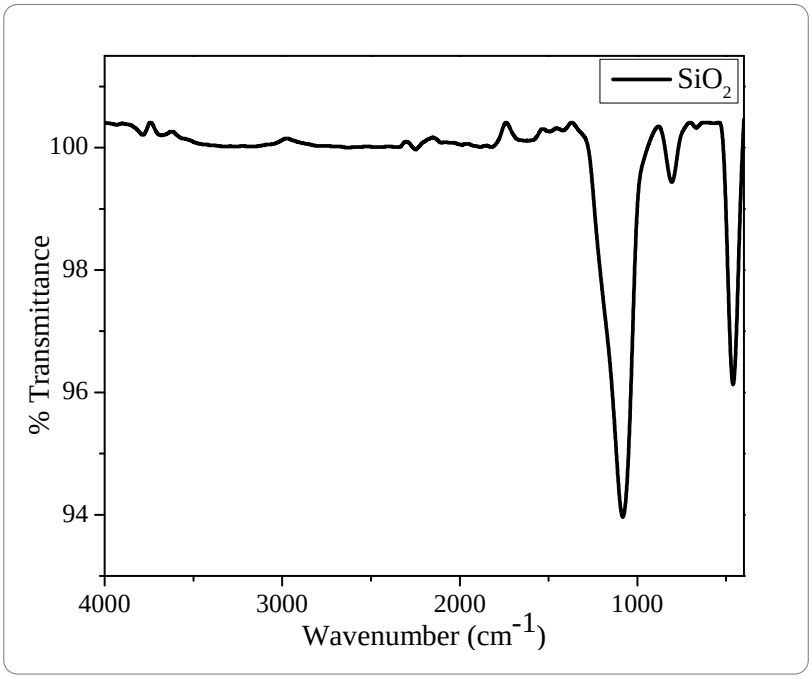

Figure 4.2: FT-IR spectrum of the SiO_2 support

4.2.2 X-ray diffraction

The x-ray diffraction spectrum of SDA support is shown in Fig 4.4, with a comparison to the Al_2O_3 and SiO_2 supports. The XRD spectrum of the Al_2O_3

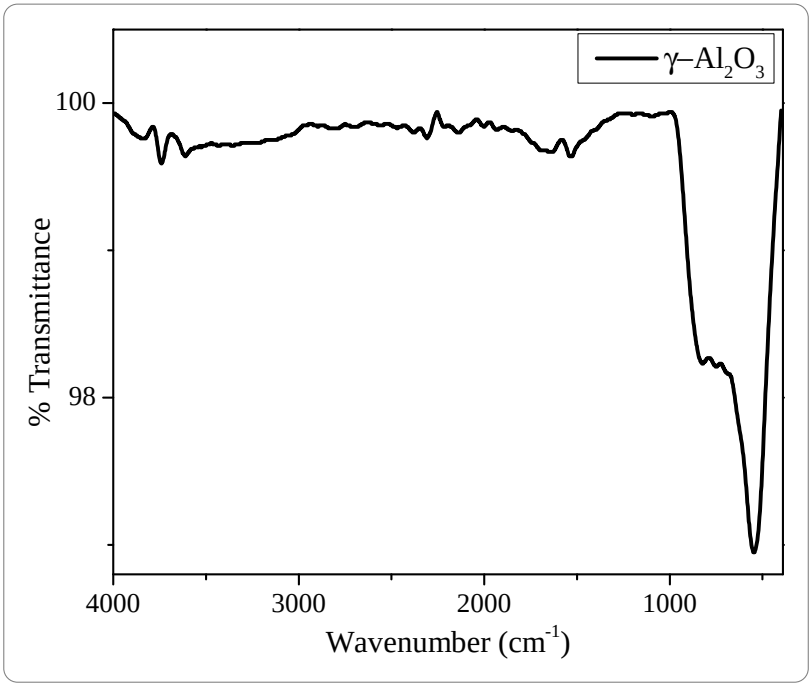

Figure 4.3: FT-IR spectrum of the Al_2O_3 support

support shows the gamma phase of alumina, with distinct 2-theta diffraction peaks observed at 66.9°, 60.61°, 45.7° and 36.8° [Gutiérrez et al., 2001]. The SiO_2 catalyst support, shows a broad diffraction peak 22.2°, indicating the amorphous nature of the SiO_2 supports. The diffraction pattern for SDA support is almost a combination of the XRD spectra of γ-Al_2O_3 and SiO_2. Despite the amorphous nature of SiO_2, the γ-Al_2O_3 shows crystalline nature in the SDA supports. Published data in the literature report higher concentrations of bronsted acid sites on amorphous SDA materials compared to crystallite SDA supports Mardkhe et al. [2014], though the total acidity greatly varies with the concentration of SiO_2 doped into the Al_2O_3 structure.

4.2.3 X-ray photoelectron spectroscopy

The deconvoluted XPS spectra of the Al2p, Si2p and O1s core level peaks for the SDA support are shown in Fig 4.5. The binding energy values of the Al2p (74.3 eV) and Si2p (102.5 eV) correspond to their oxide state. The surface concentration of SiO_2 is determined using Eqn.4.1, as described by Powell and Larson [1978]. The terms X_i, I_i, σ_i, λ_i and $D_E(i)$ are the surface concentration,

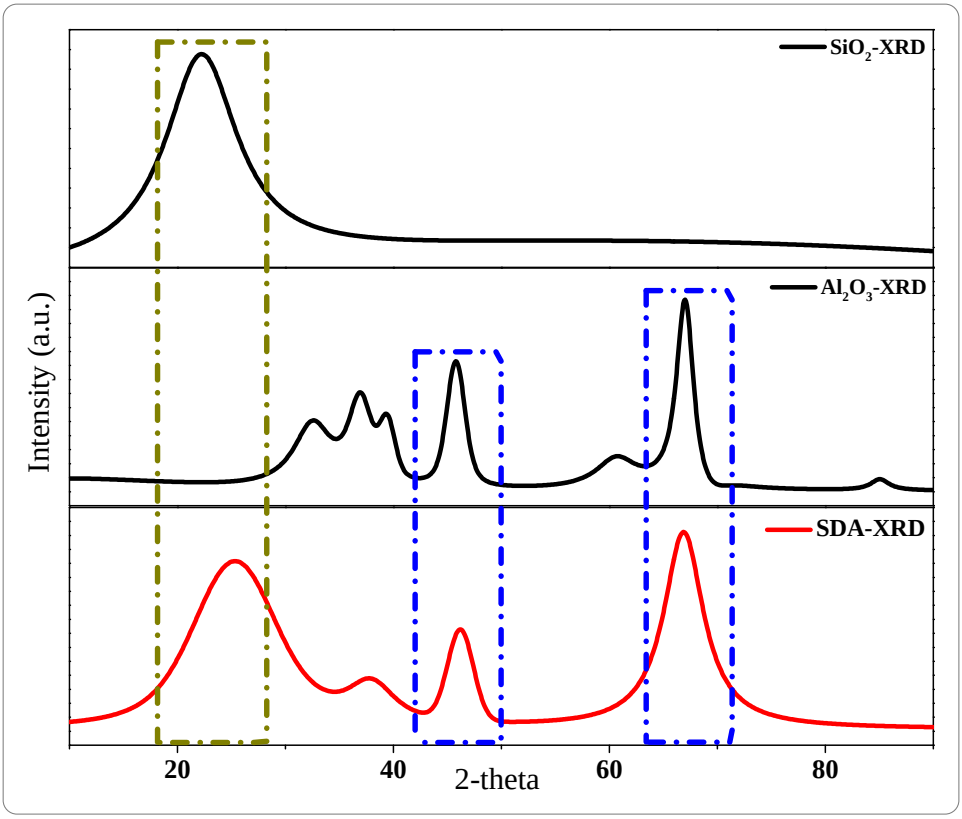

Figure 4.4: Comparison of XRD spectrum of SDA supports with the Al_2O_3 and SiO_2 spectra

intensity, photoionization cross-section, mean escape depth and geometric factors respectively.

$$\frac{X_{Si}}{X_{Al}} = \frac{I_{Si} \cdot \sigma_{Al} \cdot \lambda_{Al} \cdot D_E(Al)}{I_{Al} \cdot \sigma_{Si} \cdot \lambda_{Si} \cdot D_E(Si)} \tag{4.1}$$

The photoionization cross-section and mean escape depth values were obtained from Scofield [1976] and Penn [1976], respectively, for 1486.6 eV X-ray beam. The relative surface concentration of SiO_2 for the SDA support was 45 wt%, which is higher than the reported surface concentration of 40 wt%.

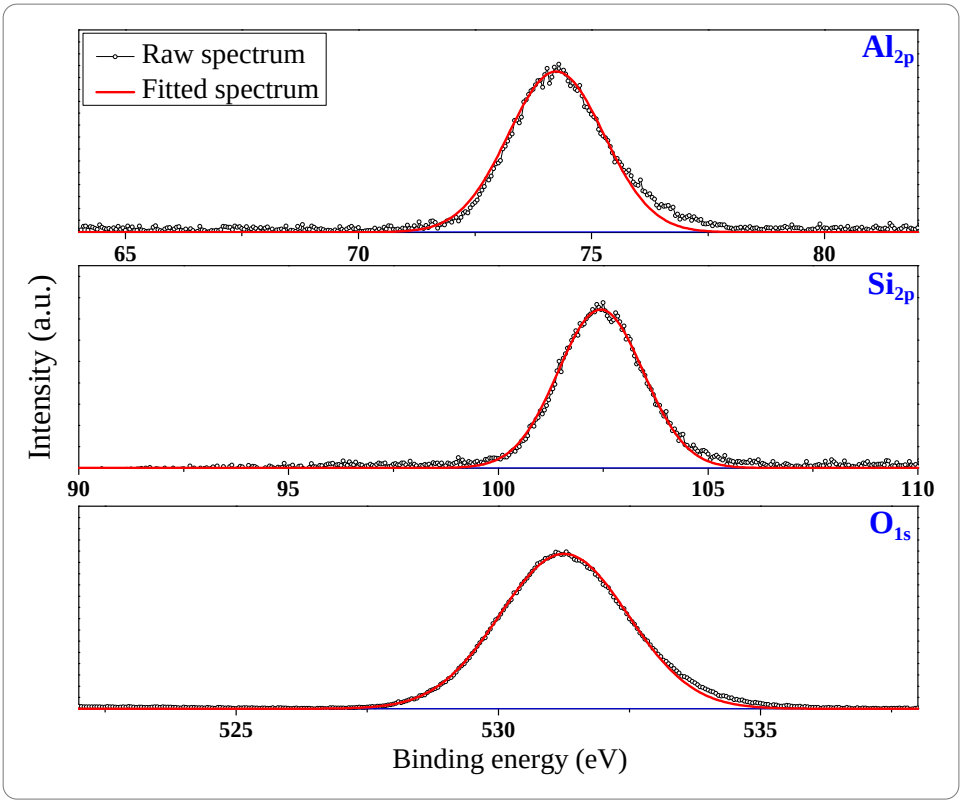

Figure 4.5: XPS spectra of the silica-doped-alumina support

4.3 Catalyst synthesis and characterization

The catalysts were developed using the combustion synthesis procedure and the incipient wetness impregnation method, as described in chapter 3. The CS catalysts were synthesized using hexamethylenetetramine as the fuel. The reaction stoichiometry was selected such that the metal nitrate to fuel molar ratio is 3.86, maintaining the equivalence ratio of one. To maintain the structural integrity of the synthesized catalysts (preventing powdering of the catalysts), the CS catalysts were synthesized in multiple steps that involved sequential impregnation and calcination. However, IWI catalysts were synthesized in a single step.

4.3.1 H_2 temperature programmed reduction - desorption

The reduction temperatures of the SDA supported catalysts were obtained using H_2 temperature programmed reduction. Fig 4.6 shows the TPR profiles of the SDA supported catalysts, and are compared with the TPR profiles of the

Al_2O_3 supported IWI and CS catalysts. The SDA supported cobalt catalysts reduce over wide temperature ranges. For the SDA-IWI catalysts the reduction temperatures extend upto 1080 K. Whereas the Al_2O_3 -IWI catalyst, the H_2 consumption peaks are limited to 950 K. However, for CS catalysts, the reduction temperatures extend to 1200 K. As reported earlier, the varying reduction temperatures are due to the different phases of cobalt oxides present on the supported catalyst (see Section 3.1.2). Three distinct reduction temperature ranges are observed. The first H_2 consumption peak at $T_1 = 550$ K, corresponds to the reduction of Co_3O_4 to CoO. A broad hydrogen consumption plateau is observed starting from 610 K (T_2) to 910 K (T_3). This wide reduction regime is attributed to the reduction of Co^{3+} ions in Co_3AlO_6 crystallites and also due to the reduction of surface or subsurface Co^{2+} ions in the Co^{2+}-Al^{3+} spinel framework. Normally, the Al_2O_3 supported IWI catalysts do not display reduction of cobalt-alumina compounds at these temperature. The doping of silica into the alumina reduces the formation of aluminates, resulting in the formation of relatively weakly bound cobalt-support species which are easily reduced below 1200 K. Similar observations were reported by Jean-Marie et al. [2009] for 5 wt.% SiO_2 doping of Al_2O_3. For SDA-CS catalysts, only marginal H_2 consumption observed in the temperature range of 600 - 700 K, unlike SDA-IWI catalysts, indicating the absence of the corresponding cobalt surface species. Similar observation is recorded for Al_2O_3 -CS catalysts. However, the CS catalysts show H_2 consumption upto 1200 K, implying continued reduction of the cobalt alumina spinel structures.

The degree of cobalt reduction obtained from the H_2 TPR curves and the average metal dispersion evaluated from the H_2-TPD curves are tabulated in Table 4.1. As seen from the table, the degree of reduction for IWI synthesized, silica doped alumina catalysts is higher than Al_2O_3 supported catalysts by 27%. The higher degree of reduction for SDA supported cobalt catalysts is due to the reduced formation of cobalt aluminates. Alteration of the Al_2O_3 support surface by the addition of SiO_2 results in the formation of alumino-silicates that impede the formation of barely reducible cobalt aluminates. It is evident from Table 4.1 that the total fraction of active Co^0 sites increases to 12.1% for IWI-SDA supported catalysts from 8.1% for Al_2O_3 -IWI catalysts, indicating a 41% increase in the metal dispersion. In case of SDA supported catalysts, the dispersion increases

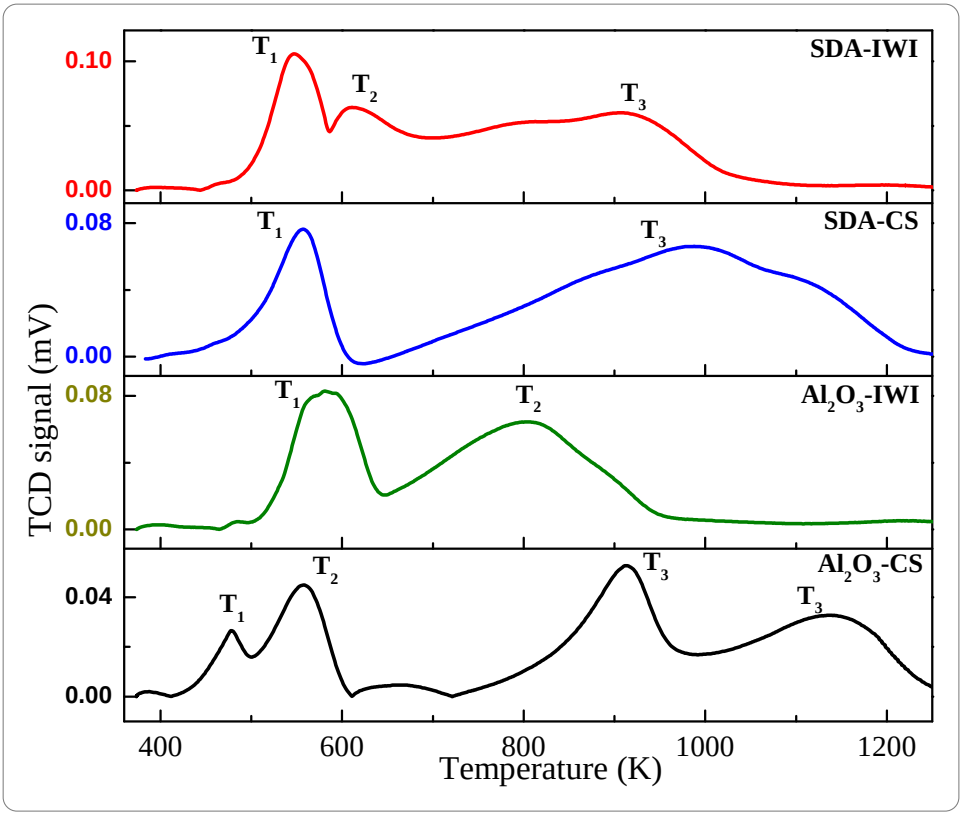

Figure 4.6: TPR spectra of the SDA supported cobalt catalysts

from 12.1% for IWI catalysts to 16.1% for CS catalysts and, for Al_2O_3 supported catalysts, the dispersion increases from 8.6% for IWI catalysts to 10.9% for CS catalysts. These results evidence higher fraction of active Co^0 over combustion synthesized catalysts. Combustion synthesized Co/SiO_2 catalysts reported by Shi et al. [2011], showed increased reduction temperatures with the degree of reduction of 89% and an improved metal dispersion of 16.6% compared to a degree of reduction of 82% and metal dispersion of 3.1% for IWI synthesized catalysts.

4.3.2 NH_3 temperature programmed desorption

The NH_3-TPD curves for the SA and Al_2O_3 supports are shown in Fig 4.7. For SDA support, the NH_3 TPD curves contain two peaks that can be categorized as low-temperature desorption peak (< 700 K) and high-temperature desorption peak (> 700 K). The peaks in the high temperature region are attributed to the desorption of NH_3 from strong Bronsted and Lewis acid sites. The peak in the low temperature region (485 K) is either due to the presence of weak Lewis

Table 4.1: TPR-TPD summary of SDA supported cobalt catalysts and compared to Al_2O_3 supported cobalt catalysts

Catalyst	**Reduction temperatures**			**DOR**	**D**
	T_1 (K)	**T_2 (K)**	**T_3 (K)**	**(%)**[a]	**(%)**[b]
Co/SDA - IWI	550	610	910	81	12.1
Co/SDA - CS	557	-	986	92	16.1
Co/Al_2O_3 - IWI	484	586	800	63.8	8.6
Co/Al_2O_3 - CS	480	554	915 ; 1140	68.7	10.9

[a]from TPR H_2 uptake; [b]from H_2 TPD of reduced catalysts

acid or due to the desorption from weakly acidic silanol group [Lónyi and Valyon, 2001]. From Fig 4.7, it is clear that the γ-Al_2O_3 supports do no possess the strong acid sites, that are evident on the SDA support surface. Addition of silica to the alumina support increases the surface acidity. Fig 4.8 shows the NH_3 TPD profile for the synthesized catalysts. Higher surface acidity is observed for CS catalysts compared to IWI catalysts. Anyhow, the alumina supported cobalt catalysts display lower surface acidity compared to SDA supported cobalt catalysts. Table 4.2 gives the magnitude of acid sites expressed as mmol NH_3/g_{cat} . As seen in the table, the SDA supported catalysts exhibit higher surface acidity compared to the Al_2O_3 supported catalysts.

Table 4.2: Surface acidity measured by NH_3-TPD

Sample	**Acid strength (mmol/g_{cat})**
SDA	0.711
Al_2O_3	0.371
SDA - IWI	1.080
SDA - CS	1.230
Al_2O_3 - IWI	0.576
Al_2O_3 - CS	0.727

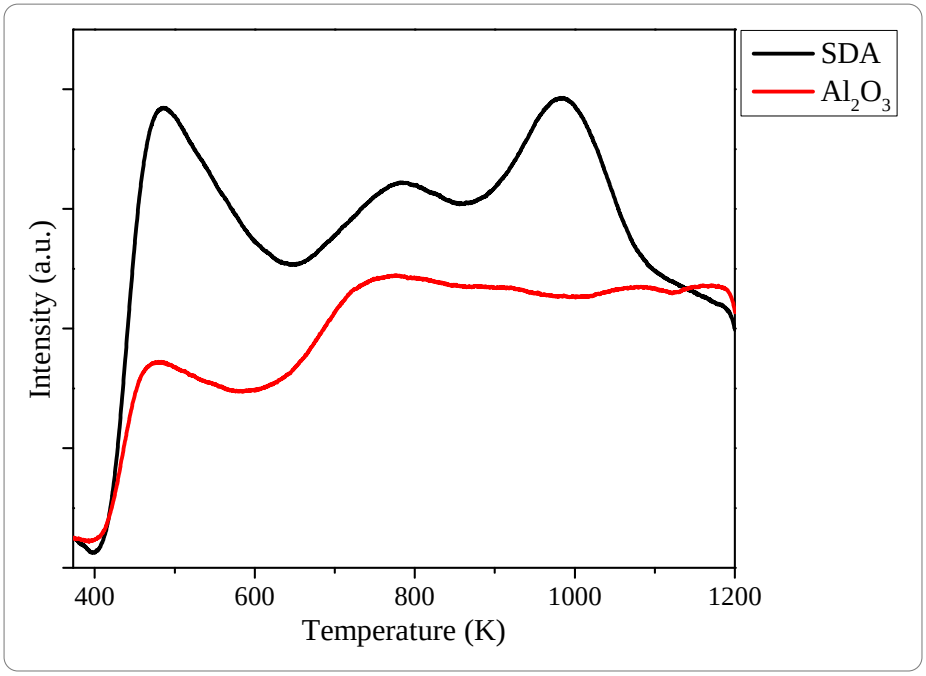

Figure 4.7: NH3-TPD of SDA and Al_2O_3 support

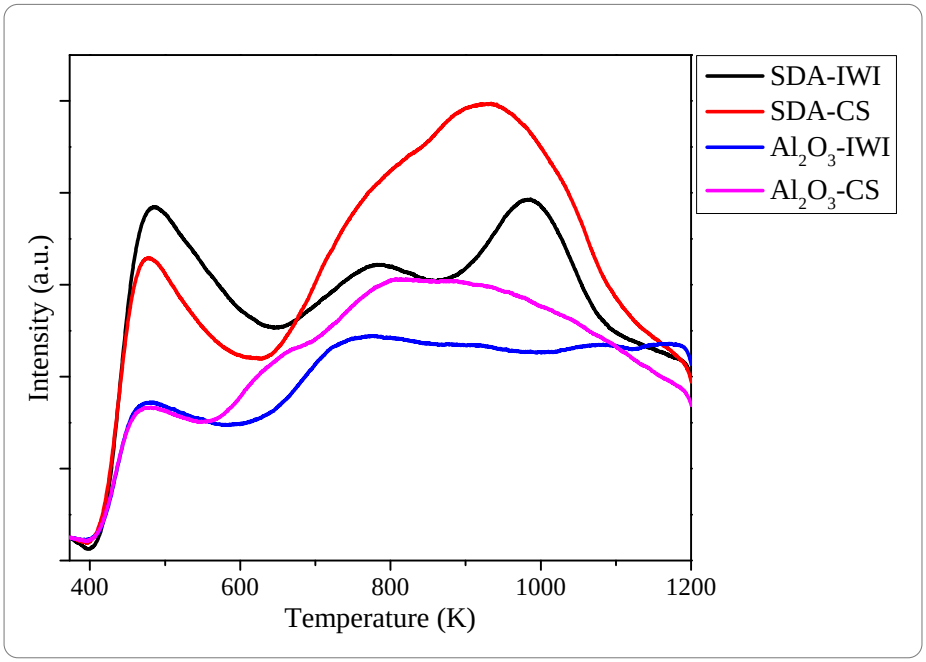

Figure 4.8: NH3-TPD of IWI and CS catalysts

4.3.3 X-ray diffraction

The XRD spectra of calcined and reduced SDA supported cobalt catalysts are shown in Fig 4.9. As expected, the XRD spectrum of IWI and CS calcined catalysts showed distinct peaks for Co_3O_4 . For the calcined catalysts, the 2-theta peaks occurred at 31.2°, 36.94°, 44.86°, 55.72°, 59.36° and 65.24°, which are consistent with the diffraction pattern for Co_3O_4 . While comparing with the XRD spectra of the Al_2O_3 supported cobalt catalysts (see Fig 3.7 and Fig 3.8), the 2-theta peaks for γ-Al_2O_3 observed at 32.9°, 38.6° and 66.9° still exist in the SDA supported catalysts. Daniell et al. [2000] in their work reported a silica encapsulation of Al_2O_3 for silica doping in the range of 30 - 60%. From the XRD results of the SDA supported cobalt catalysts, it is evident that minimum fractions of γ-Al_2O_3 phase still remain exposed on the catalyst surface. The XRD spectra of the catalysts reduced with H_2, at the reduction temperature, show sharp 2-θ peaks at 44.1° and 51.5°, which correspond to the diffraction spectrum for metallic cobalt.

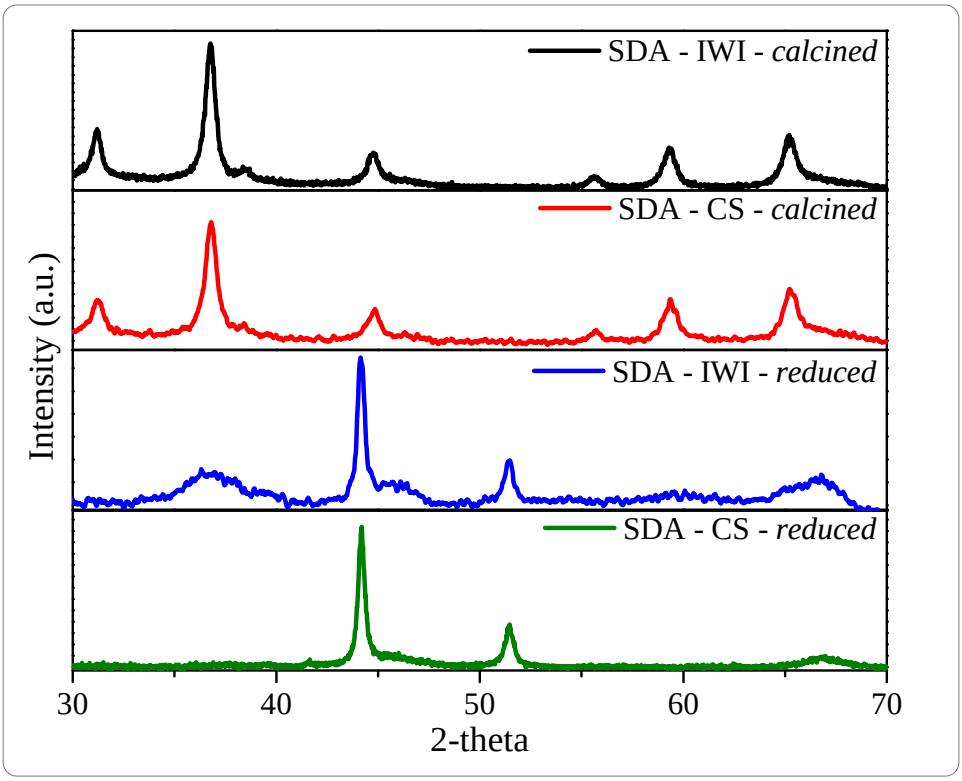

Figure 4.9: XRD spectra of the silica-doped-alumina support

The crystallite size of the calcined catalysts calculated using Eqn.2.5 are

listed in Table 4.3, along with the crystallite size of the reduced catalysts. The Co_3O_4 crystallite size for SDA supported catalysts decreases by a margin of 31% for CS catalysts (14.1 nm), compared to IWI catalysts (10.7 nm). The Co_3O_4 crystallite size for Al_2O_3 supported catalysts are comparable to SDA supported catalysts. Markedly, the crystallite size of the reduced cobalt crystals are larger than the calcined catalysts. The elevated reduction temperatures (800 - 1200 K) are bound to cause considerable sintering of the cobalt crystals, resulting in increased crystallite size. A 70 - 80% increase in the cobalt crystallite size is observed for the reduced cobalt catalysts. Similar observation is recorded for Al_2O_3 supported catalysts.

Table 4.3: Crystallite sizes of the SDA and Al_2O_3 supported catalysts

Catalyst	$\mathbf{d}_{Co3O4}$ **(nm)** [a]	$\mathbf{d}_{Co}$ **(nm)** [b]
SDA - IWI	14.1	26
SDA - CS	10.7	18.2
Al_2O_3 - IWI	15.0	22
Al_2O_3 - CS	10.5	17.6

[a]from XRD of calcined catalysts

[b]from XRD of reduced catalysts

4.3.4 X-ray photoelectron spectroscopy

Supporting the XRD results, the XPS spectra of the SDA supported Co catalysts reveal Co_3O_4 as the dominating cobalt oxide phase on the catalyst surface. Fig 4.10 shows the deconvoluted XPS spectra of the SDA supported catalysts, Similar to the Al_2O_3 supported cobalt catalysts, the peak at 779.9 eV for the SDA-IWI catalyst is assigned to the Co^{3+} oxidation state and the peak at 781.8 eV is assigned to the Co^{+2} oxidation state. The satellite peaks for the $2p_{3/2}$ orbital is observed at 787.6 eV. For the SDA-CS catalysts, the binding energy associated with the Co^{3+} oxidation state is observed at 779.7 eV, implying that the electron density of surface Co^{3+} is higher than that of IWI

catalysts and therefore signifying a weaker metal support interaction in the case of CS catalysts.

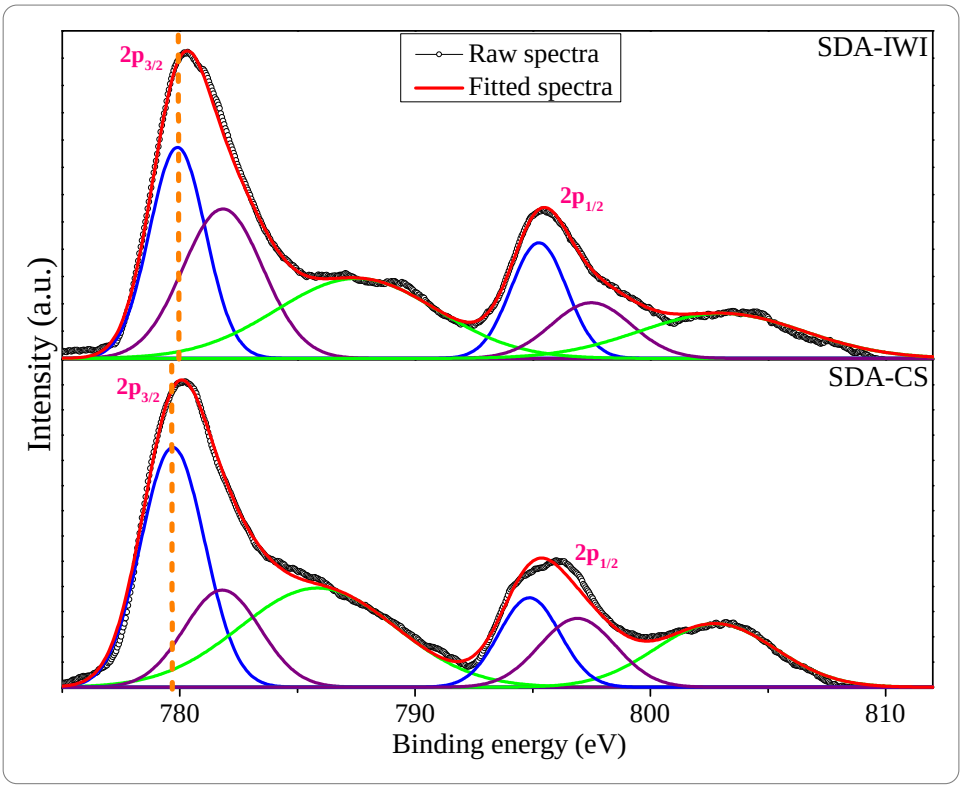

Figure 4.10: XPS spectra of the SDA supported cobalt catalysts

The binding energy of Co^{3+} in the 2p-$_{3/2}$ orbital and the spin orbital splitting are tabulated in Table 4.4. As reported earlier, the ratio of the intensities of Co-2$p_{3/2}$ peak at 779.9 eV to the intensity of the shake-up satellite peak provides the relative formation of $CoAl_2O_4$ in the synthesized catalysts (see section 3.1.4). From Table 4.4, it is evident that the silica doping in the Al_2O_3 drastically reduces the formation of cobalt aluminates. Moreover, the CS catalysts too revealed decreased production of cobalt aluminates, indicating lower metal support interaction. The measure of the cobalt dispersion, evaluated from the Al and Co peak intensity ratios, indicate a higher cobalt dispersion for the SDA supported catalysts compared to Al_2O_3 supported catalysts. As seen in Table 4.4, the SDA supported cobalt catalysts synthesized by the combustion method, exhibit highest metal dispersion. The percentage metal dispersion obtained from the H_2 TPR-TPD experiments support the values obtained from XPS spectrum analysis. The metal dispersion as observed from the XPS spectral analysis shows

Table 4.4: XPS comparison for SDA and Al_2O_3 supported cobalt catalysts

Catalyst	B.E. Co-$2p_{3/2}$ (eV)	spin-orbital splitting (eV)	I-$Co2p_{3/2}$/ I-shake-up	$\mathbf{I_{Co}/I_{Al}}$
SDA-IWI	779.9	15.3	0.9	**0.6**
SDA-CS	779.7	15.2	1.1	**1.6**
Al_2O_3 -IWI	780.4	15.2	0.7	**0.2**
Al_2O_3 -CS	779.9	15.2	0.9	**1.1**

that D-$_{Al2O3-IWI}$ < D-$_{Al2O3-CS}$ and D-$_{SDA-IWI}$ < D-$_{SDA-CS}$, further evidencing that the combustion synthesized catalysts result in higher degree of reduction, higher metal dispersion and consequently, larger number of active metal sites for the FT reaction. Additionally, the SDA supports display higher metal dispersion compared to alumina supported catalysts, signifying reduced metal support interaction for SDA supported catalyst.

4.4 FT activity

Fig 4.11 shows the FT activity and the hydrocarbon selectivity of the SDA supported cobalt catalysts compared to the Al_2O_3 supported catalysts. The activity and selectivity are measured at 503 K, 3 MPa, and a space velocity of 1730 ml/(h·g_{cat}). The enhanced properties of the CS catalysts improve the CO conversions, which has been already evidenced by Al_2O_3 supported catalysts (see section 3.2). The CO conversion for SDA-CS catalysts increased to 51.2% from 37.9% as seen for SDA-IWI catalysts. A similar trend is observed for Al_2O_3 supported catalysts with 28% increase in CO conversion observed for CS catalysts. The C_{5+} selectivity increases by 5.6% for Al_2O_3 -CS catalysts, but only a marginal increase of 0.7% is seen for SDA-CS catalysts. The FT activity of IWI and CS catalysts measured as the rate of CO consumption per unit mass of catalysts is shown in Fig 4.12. Again, the increased performance of CS catalysts is attributed to its reduced cobalt crystallite size, increased degree of reduction and higher metal dispersion. A 2% increase in the CH_4 selectivity is observed for SDA-CS catalyst compared to SDA-IWI catalyst while the CH_4 selectivity remained steady at 10% for Al_2O_3 -CS and Al_2O_3 -IWI catalysts. As seen in

Fig 4.11, the SDA supported cobalt catalyst displays higher selectivity for C_2-C_5 hydrocarbon fraction as compared to the Al_2O_3 supported cobalt catalyst. The C_2-C_5 selectivity for SDA-IWI and SDA-CS catalyst is 3.1 and 2.7 times higher than Al_2O_3 -IWI and Al_2O_3 -CS catalysts. The higher selectivity of C_2-C_5 hydrocarbons could be due to the existence of aluminosilicate structure occurring in the supports, giving it a zeolite-like behaviour. A similar observation was reported by Fraenkel and Gates [1980]. The higher C_2-C_5 selectivity for SDA supported catalysts results in lower C_{5+} selectivity, compared to Al_2O_3 supported catalysts.

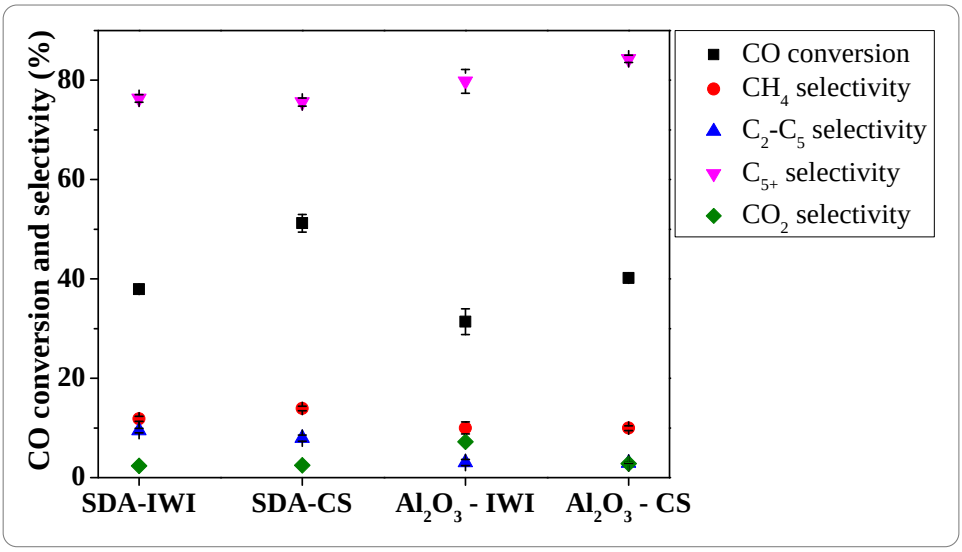

Figure 4.11: CO conversion and hydrocarbon selectivity for SDA and Al_2O_3 supported catalysts
[*Measured at 503 K, 3 MPa and WHSV = 1730 ml/(h·g_{cat})*]

The stability of the synthesized catalysts is evaluated by observing the activity and selectivity changes during the experimental run for a duration of 160 hours. Fig 4.13 and Fig 4.14 shows the variation in CO conversion and hydrocarbon selectivity as a function of time on stream. In case of SDA supported catalysts synthesized by IWI and CS, the CO conversion, and HC selectivity remain steady for a duration of 160 hours, indicating no possible catalyst deactivation. In case of Al_2O_3 supported catalysts synthesized by IWI method (also shown in the previous chapter), the CO conversion increases from 23% to 34% over 160 hours of operation.

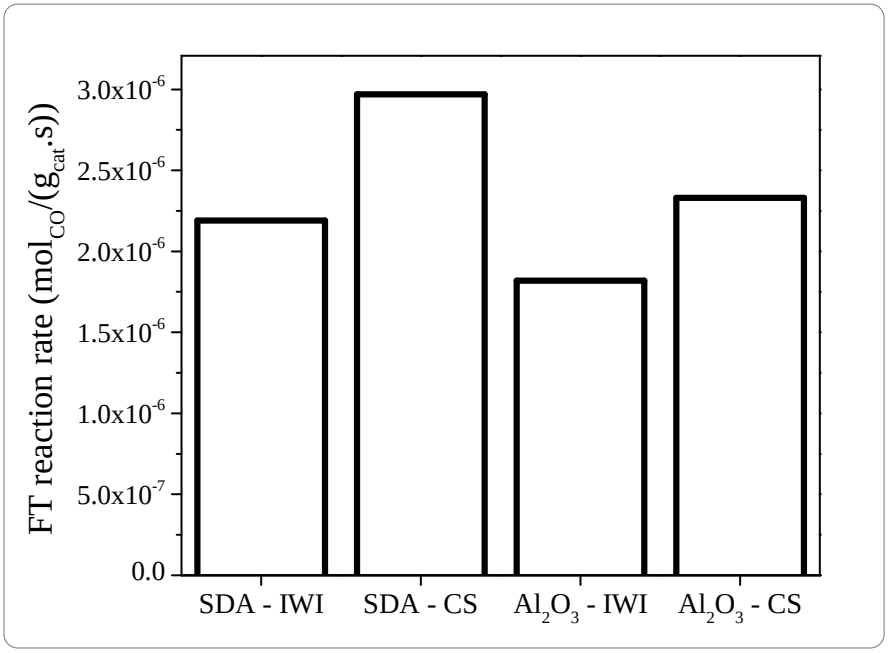

Figure 4.12: FT activity measured for SDA and Al_2O_3 supported catalysts [*Measured at 503 K, 3 MPa and WHSV = 1730 ml/(h·g_{cat})*]

4.4.1 Product spectrum

In the previous chapter, it was observed that the product spectrum is exceedingly affected by the synthesis procedure. The hydrocarbon product analysis for SDA supported catalysts show that the nature of FT products is not only not only a function of the synthesis procedure but also depends on the support material used. Fig 4.15 and Fig 4.16 show the weight fraction distribution of the liquid hydrocarbon products and waxes. The liquid hydrocarbon products consist of hydrocarbons ranging from C_{10} to C_{24}, while the wax hydrocarbons comprise of hydrocarbons of mainly C_{24+}. Above all, the hydrocarbons are mostly, straight chain paraffins. For SDA supported catalysts, the C_{24+} weight fraction increases from 0.01 wt.% for combustion synthesized catalysts to 0.6 wt.% for IWI catalysts. For Al_2O_3 supported catalysts, the C_{24+} weight fraction increases from 0.67 wt.% to 0.8 wt.%. The hydrocarbons synthesized over Al_2O_3 supported cobalt catalysts resulted in the formation of heavier waxes than middle distillates as compared to catalysts synthesized over SDA supports. The HC product spectrum for Al_2O_3 -CS catalysts show 0.8 wt.% C_{24+} compared to 0.6 wt.% C_{24+} for SDA-CS catalysts. The 33% higher weight fraction of C_{24+} hydrocarbons for Al_2O_3 supported cobalt catalysts is due to the total number of acidic sites present

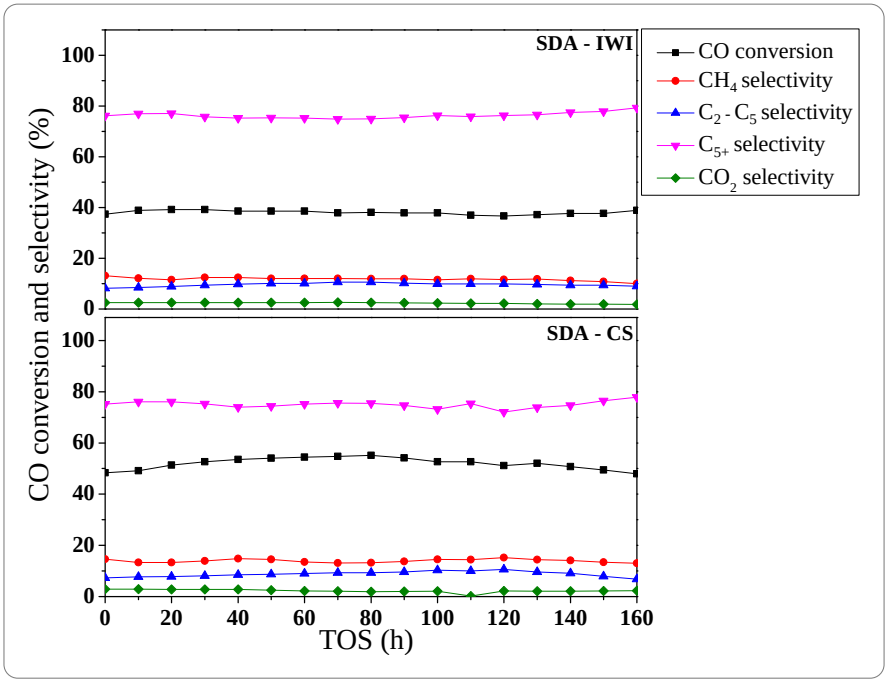

Figure 4.13: Variation in the CO conversion and HC selectivity with time on stream, for SDA supported CO catalysts
[*Process conditions : T = 503 K, P = 3 MPa and WHSV = 1730 ml/(h·g_{cat})*]

in the SDA supports. The addition of silica to alumina results in the formation of stronger Bronsted acid sites, through bridged hydroxyl group formation across aluminium and silicon atoms. Lower surface acidity results in FT product spectrum consisting primarily of lighter and more branched hydrocarbons [Di et al., 2013]. The NH_3-TPD of SDA supports, as seen in Table 4.2, shows surface acidity of 0.7 mmol NH_3/g_{cat} compared to 0.4 mmol NH_3/g_{cat} for Al_2O_3 supported catalysts, additionally supporting the effect of surface acidity on the FT product spectrum. As already mentioned in the earlier section, the C_2-C_5 selectivity for SDA-IWI and SDA-CS catalyst is observed to be nearly 2.4 times greater than the Al_2O_3 supported catalysts. A detailed analysis of the GC-MS spectrum of the FT products reveal the variation in the hydrocarbon weight fraction for the SDA and Al_2O_3 supported catalysts.

Fig 4.17 shows the variation in the C_{5+} yield for CS catalysts with varying space velocities. A decrease in the space velocity from 2610 ml/(h·gcat) to 873.3 ml/(h·gcat) results in the increase of yield from 0.28 g-$_{C5+}$/g-$_{syngas}$ to 0.52 g-$_{C5+}$/g-$_{syngas}$, indicating 86% increase in the product yield. However, negligible

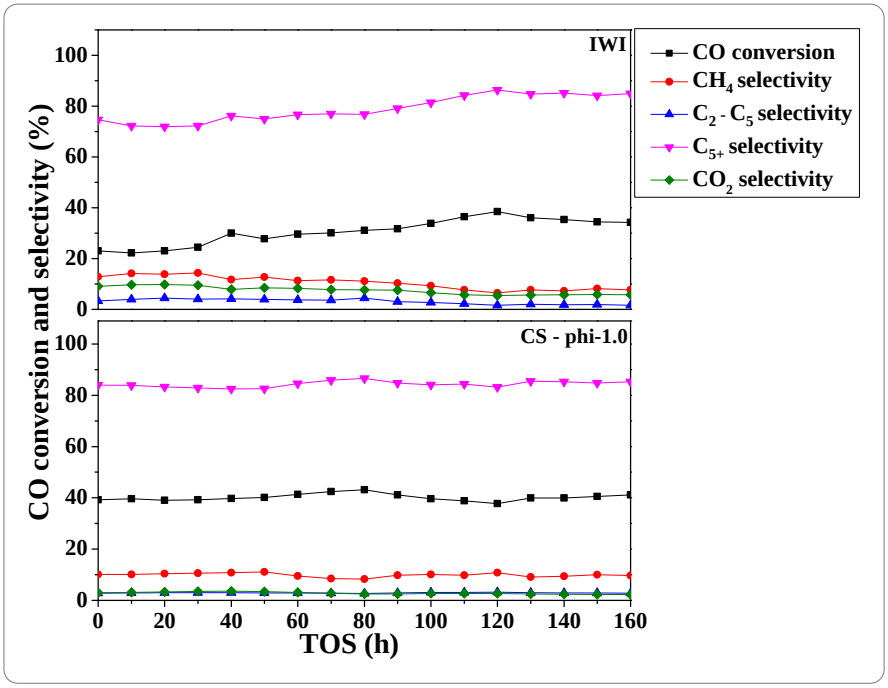

Figure 4.14: Variation in the CO conversion and HC selectivity with time on stream, for Al_2O_3 supported CO catalysts
[*Process conditions : T = 503 K, P = 3 MPa and WHSV = 1730 ml/(h·g_{cat})*]

change in the hydrocarbon product spectrum is observed by changing the reactor bed residence time. 84% increase in the product yield is observed for Al_2O_3 supported CS catalysts by decreasing the space velocity from 2610 ml/(h·gcat) to 873.3 ml/(h·gcat). Above all, a reduction in the space velocity, i.e., an increase in the bed residence time from 6 s to 18 s gradually shifts the product spectrum from waxes to the liquid hydrocarbon as shown in Fig 4.18. A possible reason for this could be attributed to the decrease in the superficial velocity that prevents the external mass transfer of waxes formed on the catalyst surface. Higher superficial velocity would favour external mass transfer that increases proportionally with the half order of the flow rate around the catalyst spheres [Yang et al., 2010]. Moreover, a higher superficial velocity is preferred for the fixed bed FT reaction to remove the water produced during the FT process - presence of water promotes the sintering of catalyst particles [Rafiq et al., 2011].

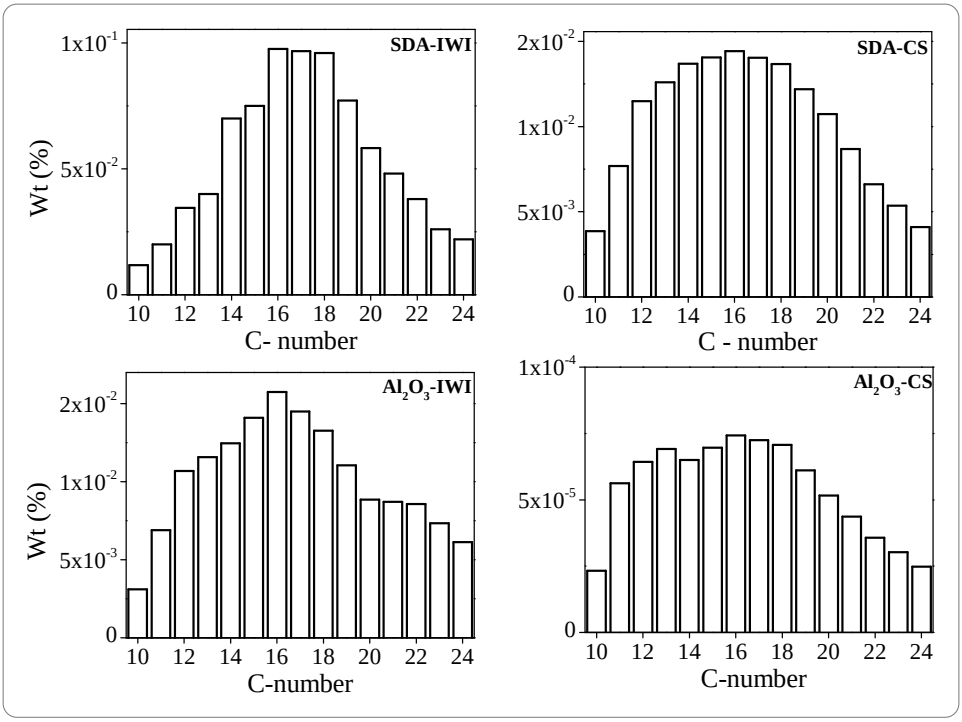

Figure 4.15: Weight fraction of the C_{10}-C_{24} hydrocarbons for SDA and Al_2O_3 supported cobalt catalysts
[*Process conditions : T = 503 K, P = 3 MPa and WHSV = 1730 ml/(h·g_{cat})*]

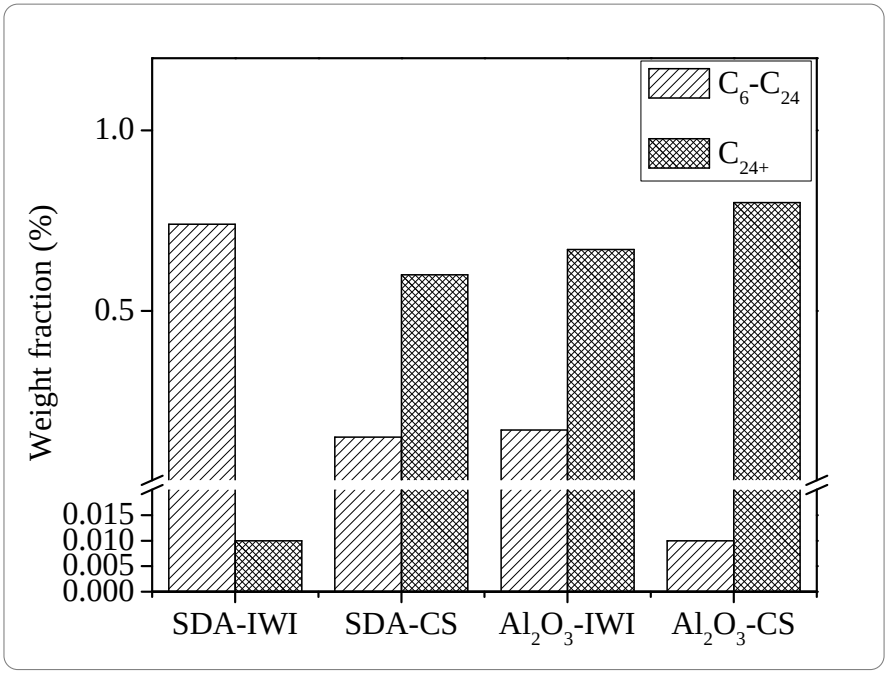

Figure 4.16: Weight fraction of the C_{24+} hydrocarbons for SDA and Al_2O_3 supported cobalt catalysts
[*Process conditions : T = 503 K, P = 3 MPa and WHSV = 1730 ml/(h·g_{cat})*]

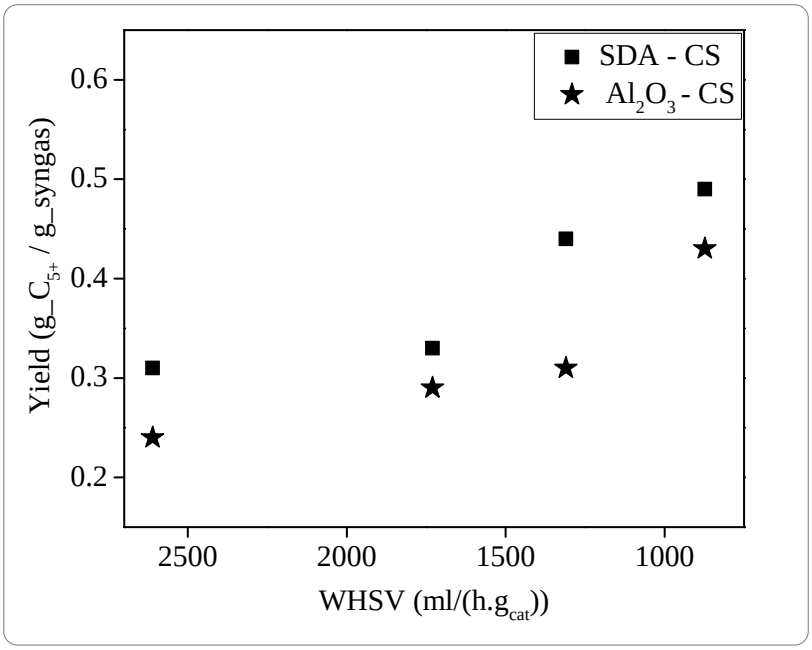

Figure 4.17: Hydrocarbon yield (C_{5+}) as a function of WHSV

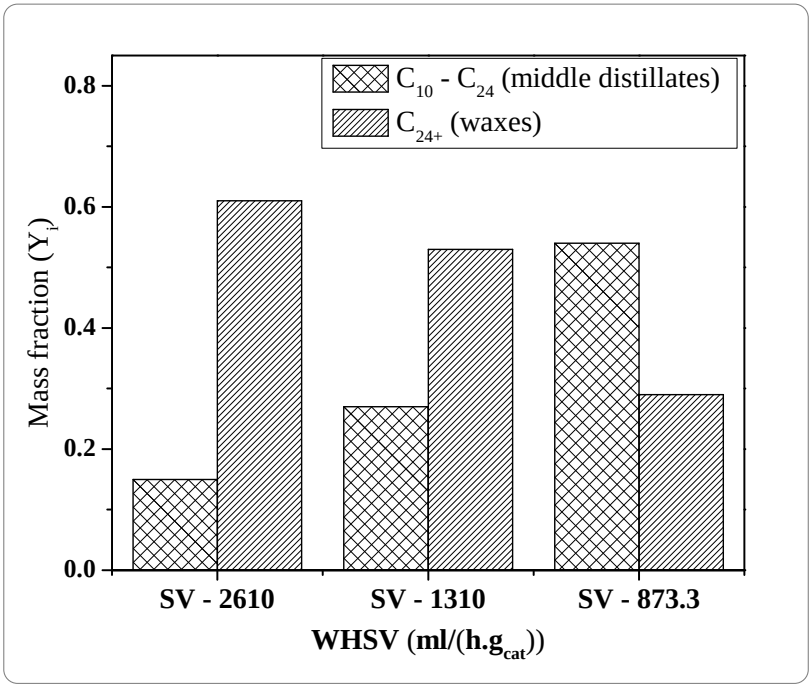

Figure 4.18: Variation in the weight fraction of the middle distillates and waxes with WHSV

4.5 Summary

This chapter has identified the role of supports in the Fischer Tropsch reaction. From the catalyst properties point of view, the incorporation of SiO_2 in the Al_2O_3 support framework results in the formation of higher concentration of Lewis acid sites and also formation of small fractions of highly acidic Bronsted acid sites. The total surface acidity as measured by the NH_3-TPD experiments, reveal nearly 90% increase acid strength of the SDA supports. The Lewis acid sites are formed by the isomorphous substitution of tetrahedral Si^{4+} by Al^{3+} ions. Further, the XRD and XPS study of the SDA support reveal surface encapsulation of Al_2O_3 by SiO_2 atoms with a silica doping of 30 wt.%. Incorporation of silica into the alumina support, drastically reduces the formation of cobalt aluminates, resulting in lower metal support interaction as compared to cobalt deposited in Al_2O_3 supports. Consequently, the degree of cobalt reduction of 92% is observed for SDA-CS catalysts, while the reduction degree is merely 68.7% for Al_2O_3 -CS catalysts. Simultaneously, the metal dispersion, measured by the H_2-TPD experiments increase by a margin of 48% for SDA-CS catalysts compared to Al_2O_3 -CS catalysts. The higher degree of reduction and enhanced metal dispersion for SDA supported catalysts is additionally substantiated by the XPS analysis.

The SDA supported cobalt catalysts show higher FT activity and selectivity compared to Al_2O_3 supported catalysts synthesized by IWI method. The CO conversions and C_{5+} selectivity are further enhanced for SDA supported cobalt catalysts synthesized by solution combustion method. Alumina supported catalysts, due to its higher surface basicity compared to SDA catalysts, largely resulted in the formation of waxes (C_{24+}), while hydrocarbons ranging from C_{10}-C_{20} formed as the primary product for SDA supported catalysts. Furthermore, the improved performance of CS catalysts is attributed to higher degree of reduction, enhanced metal dispersion, and reduced metal support interaction.

Chapter 5

Summarizing catalyst properties and overall hydrocarbon yield

Besides the synthesis of CS catalysts with high metal loading ($\sim$ 20 wt.%), the CS catalysts resulted in enhanced catalyst properties, ideal for FT synthesis. This chapter highlights the properties of the synthesized catalysts with respect to their crystallite size, reduction degree, cobalt dispersion and the metal support interaction. Further, the overall FT activity, hydrocarbon selectivity and in particular the hydrocarbon yield for the synthesized catalysts are discussed and compared with the catalysts from the literature.

5.1 Catalyst properties

The designation for cobalt catalysts synthesized in this work are listed in Table 5.1, and the variation in their properties are shown in Fig 5.2. The combustion synthesized cobalt catalysts resulted in lower Co_3O_4 crystallite size ranging from 6.6 nm - 10.7 nm. However, not much variation in the Co_3O_4 crystallite size was observed for Al_2O_3 and SDA supported CS catalysts. It was observed that elevated reduction temperatures (800 - 1200 K), resulted in considerable increase in the Co crystallite size, ranging from 14.8 nm - 18.2 nm. Even then, the CS catalysts displayed lower crystallite size compared to IWI catalysts. However, not much variation in the Co_3O_4 crystallite size was observed for Al_2O_3 and SDA supported CS catalysts.

Higher degree of reduction and cobalt dispersion are obtained for CS catalysts compared to the IWI catalysts. The cobalt dispersion for CS catalysts is in the range of 11 - 16% and the degree of reduction as high as 92%. The en-

Table 5.1: Designation used for the synthesized catalysts

Designation	Catalyst support	Synthesis method
Al-I	Al_2O_3	IWI
Al-C	Al_2O_3	CS
Al-C-1.2	Al_2O_3	CS(ϕ=1.2)
Al-C-1.5	Al_2O_3	CS(ϕ=1.5)
SDA-I	SDA	IWI
SDA-C	SDA	CS

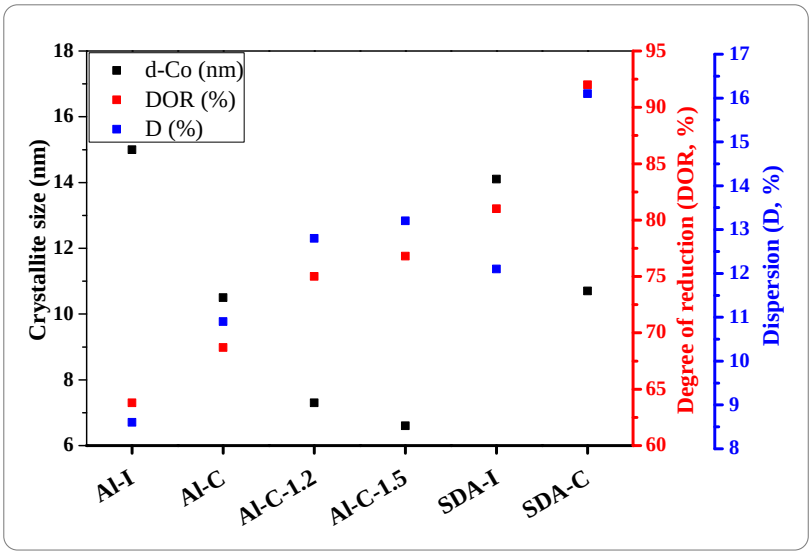

Figure 5.1: Summarizing the crucial FT catalyst properties synthesized in this work

hanced degree of reduction and higher fraction of active Co^0 sites are attributed exclusively to the decreased formation of cobalt-alumina compounds (*cobalt aluminates*), additionally indicating a lower metal support interaction. Besides, the maximum degree of cobalt reduction and the largest fraction of active cobalt sites are attained for SDA-CS cobalt catalysts, which is attributed to the formation of aluminosilicate that hinders the formation of cobalt aluminates, increasing the degree of reduction to 92% and cobalt dispersion to 16.1%.

5.2 Overall hydrocarbon yield comparison

This section compares the overall hydrocarbon yield for the catalysts synthesized in this work. Overall, the combustion synthesized catalysts, owing to its enhanced catalyst properties, showed higher FT activity and higher C_{5+} selectivity compared to the IWI catalysts. For alumina supported catalysts, highest syngas conversion was recorded for CS(ϕ=1.2) catalysts, for which a two fold increase in the CO conversion was observed compared to Al_2O_3 -IWI catalysts. Only a marginal variation in the C_{5+} selectivity was observed for the alumina supported catalysts. For the SDA supported catalysts, the FT activity additionally increased. A 24% increase in the CO conversion was observed for SDA-CS catalysts compared to Al_2O_3 -CS catalysts. Strikingly, the C_2-C_5 hydrocarbon mass fraction for SDA supported catalysts was almost 2.4 times higher than the Al_2O_3 supported catalysts. The higher fraction of gas phase hydrocarbons for SDA support was attributed to the existence of aluminosilicate structure, giving it a zeolite like behaviour. Subsequently, a lower C_{5+} selectivity was recorded for SDA supported catalysts.

However, the product spectrum varied not only with the catalyst synthesis procedure but also with the choice of support. With CS catalysts, the product spectrum predominantly yielded waxes. The spectrum shifted to middle distillates for CS catalysts synthesized with higher equivalence ratio. Increased surface acidity with SiO_2 doping of Al_2O_3 resulted in relatively higher concentrations of middle distillates. Fig 5.2 shows the C_{5+} hydrocarbon yield for the synthesized catalysts. Clearly, the largest hydrocarbon yield is obtained for Al_2O_3 -CS-1.2 catalysts.

Fig 5.3 compares the FT activity and product yield for the catalysts synthesized in this work and with the catalysts from other literature sources ([Visconti et al., 2011], [Jean-Marie et al., 2009], [Lira et al., 2008], [Phienluphon et al., 2014], [Shi et al., 2011], [Shi et al., 2012]), that employed alumina or silica doped alumina supported cobalt catalysts. The SDA supported combustion synthesized catalysts show highest C_{5+} yield corresponding to 0.31 g- C_{5+}/g-$_{cat}$, at a space velocity of 2610 ml/(h·g$_{cat}$). The CS SiO_2 supported cobalt catalysts synthesized by Shi et al. [2012] and Shi et al. [2011] reported C_{5+} yields with a space velocity of 2477.6 ml/(h·g$_{cat}$), that are 20% and 42% lower than yields reported in this work. Moreover, in spite of lower CO conversion compared to that achieved with

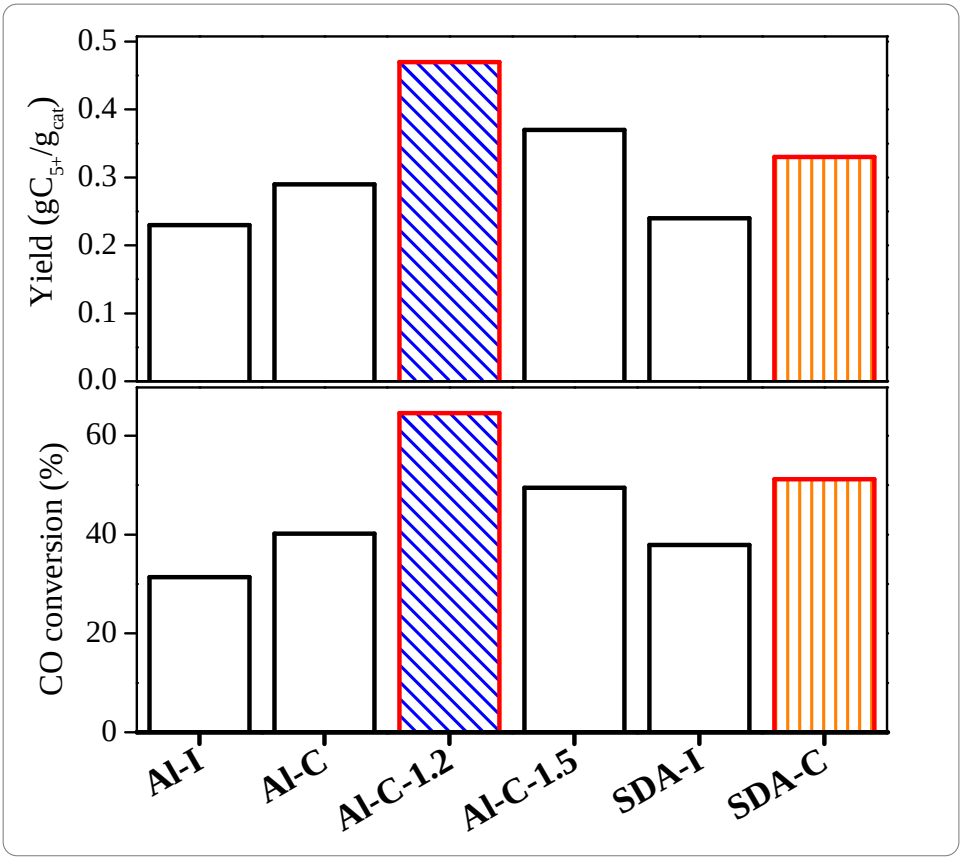

Figure 5.2: Comparison of the CO conversion and overall C_{5+} hydrocarbon yield [*Process conditions : P = 3 MPa; T = 503 K; WHSV = 1730 ml/(h·g$_{cat}$)*]

the Shi et al. [2012] and Shi et al. [2011] catalysts, the higher hydrocarbon yield indicates higher *site time yield* for the CS-SDA cobalt catalysts.

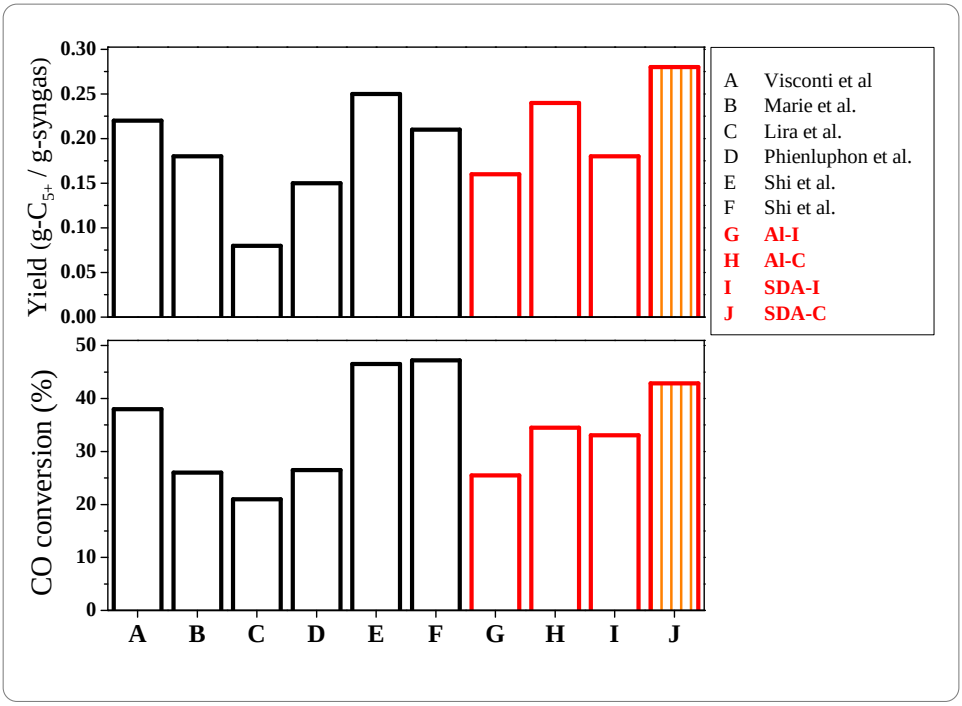

Figure 5.3: CO conversion and overall C_{5+} hydrocarbon yield comparison with catalysts from other literature sources

5.3 Summary

This chapter has summarized the overall performance of the synthesized catalysts in terms of the CO conversion and the hydrocarbon yield. Comparison was made between the synthesized catalysts at reaction conditions of 503 K, 3 MPa and WHSV = 1790 ml/(h·g_{cat}). Further, these catalysts were also compared to the catalysts from the available literature. The combustion synthesized cobalt catalysts supported over silica doped alumina spheres display highest hydrocarbon yield.

Chapter 6

Conversion, product yield and economics

6.1 Introduction

The quandary of fluctuating oil prices and, the deteriorating environmental factors have sufficiently motivated us to exploit renewable energy sources. For a country such as India, which imports nearly 75% of its crude oil, a primary requisite emerges to investigate and establish indigenous facilities for producing crude oil. It has been shown in chapter one, that the Fischer Tropsch process is the only viable route, at present, to synthesize crude oil which can be further hydrocracked and upgraded to produce transportation fuels and chemicals. Syngas obtained from biomass gasification unit can be used as a feed to the FT reactor for generation of higher hydrocarbons. For a large scale implementation of any new technology, it is naturally essential to evaluate its economic feasibility and, above all, for a sustainable and sound operation of the BTL plant, a detailed assessment of the financial returns is needed. The purpose of this work is to analyse the economic feasibility of a BTL plant. The syngas generation unit includes a steam-oxygen gasification unit coupled to a fixed-bed low temperature FT reactor. The overall conversions, FT activity, selectivity and the hydrocarbon yield of cobalt based catalysts, developed earlier, constitute the FT building block. The techno-economic analysis is demonstrated for a 1000 kg/h fixed-bed, biomass gasification system. The following sections associate the mass and energy flow from a fully developed steam-oxy biomass gasifier to the FT reactor.

6.2 Biomass gasification unit

Gasification is a two-stage reaction consisting of oxidation and reduction processes. These processes occur under sub-stoichiometric conditions of air with biomass. The first part of sub-stoichiometric oxidation leads to the loss of volatiles from biomass and is exothermic; it results in peak temperatures of 1400 to 1500 K and generation of gaseous products like carbon monoxide, hydrogen in some proportions and carbon dioxide and water vapour which in turn are reduced in part to carbon monoxide and hydrogen by the hot bed of charcoal generated during the process of gasification. Reduction reaction is an endothermic reaction to generate combustible products like CO, H_2 and CH_4 as indicated below.

Among the biomass gasification technologies in the world, the open top, twin air entry, re-burn gasifier developed at *Combustion, Gasification and Propulsion Laboratory* (CGPL) of Indian Institute of Science (IISc) is unique in terms of generating superior quality producer gas. There are more than 40 plants that are successfully operating in India and overseas for heat and power applications. The reactor is developed in a way to increase the residence time inside the reactor and, by creating an elevated temperature in the char bed, thereby enhancing the conversion efficiency and decreasing the tar fractions to negligible concentrations. In this reactor configuration, air (gasifying medium) is extracted into the reaction chamber from the top and from the side air nozzles and the product gasses exit through the base of the reactor. For the steam-oxygen gasification operation, the reactor openings (top and side air nozzles) are sealed and, the reactor bed is injected with oxygen and steam at desired flow rates. Fig 6.1 shows the layout of the oxy-steam biomass gasifier used in this study. Casurina wood chips are used as a fuel for gasification. These wood chips are dried at 378 K to reduce the moisture content below 1%. Table 6.1 lists the proximate and ultimate analysis details of the biomass used.

Amongst the process conditions for oxy-steam biomass gasification, the steam to biomass ratio (SBR) and equivalence ratio have a significant effect. Fig 6.2 shows the variation of H_2/CO ratio with varying SBR. Increasing SBR, elevates the H_2 concentration in the syngas and at the same time, the adiabatic flame temperature reduces due to the endothermic nature of steam gasification (see Eqn.1.3). As seen in the plot, and SBR must be in the range of 0.8 to 1.2, to achieve syngas with H_2/CO in the ratio 2.1:1, which is an ideal case for

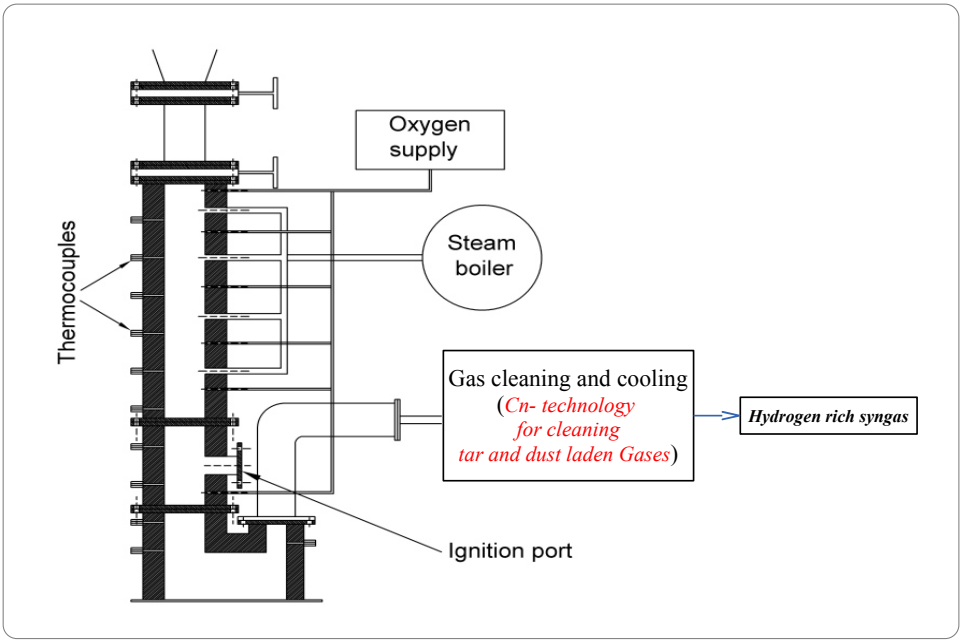

Figure 6.1: Oxy-steam gasification layout
[*A 10kg/h oxy-steam biomass gasification setup developed by Sandeep and Dasappa [2014]*]

cobalt based FT system. Simultaneously, the equivalence ratio (ER) affects the bed temperature, and has to be selected appropriately in order to maintain the H_2/CO ratio. An adiabatic temperature of 1200 K is preferable for enhancing the H_2 concentration in the syngas and, therefore, an ER of 0.1 is maintained, and SBR ranging from 0.8 to 1.2. The time variation of gas concentration under these conditions, is shown in Fig 6.3. The exit syngas composition as shown in the figure were recorded for a duration of six hours. The mass and energy balance for the techno-economic analysis consider these volumetric fractions of the syngas for FT reaction.

Table 6.1: Proximate and ultimate analysis of casurina wood chips

Proximate analysis	**Mass fraction** (%, dry basis)
Fixed carbon	18.38
Volatile matter	81.28
Ash content	0.34
Calorific value	17.95 MJ/kg
Ultimate analysis	**Mass fraction** (%, dry basis)
Carbon	52.02
Nitrogen	0.12
Sulphur	0.42
Hydrogen	6.55
Oxygen	41.43
Chemical composition	$CH_{1.4}O_{0.6}$
Molecular weight	23 g/mol

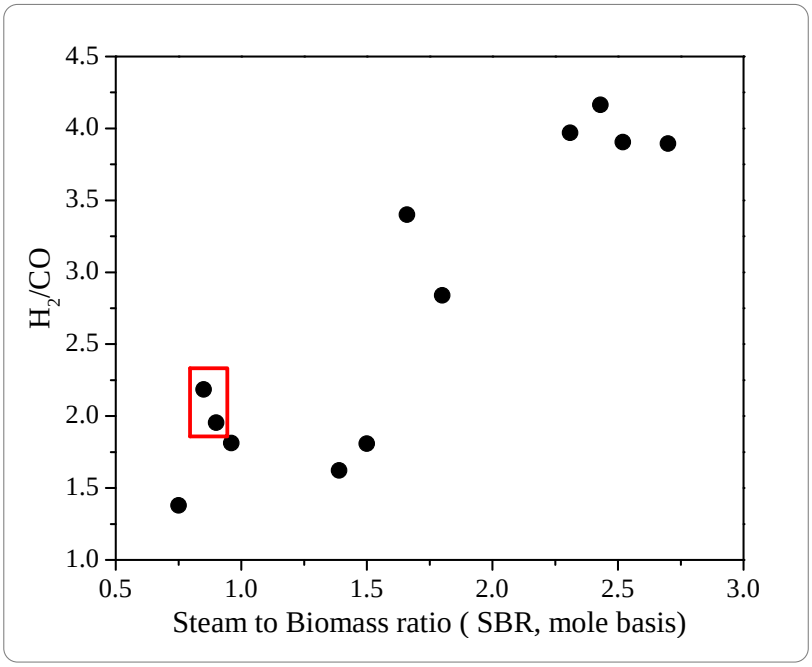

Figure 6.2: Effect of steam to biomass ratio on the H_2/CO ratio in the syngas [Sandeep and Dasappa, 2014]
[*Desired operating range enclosed in red; SBR = 0.8 - 1.2*]

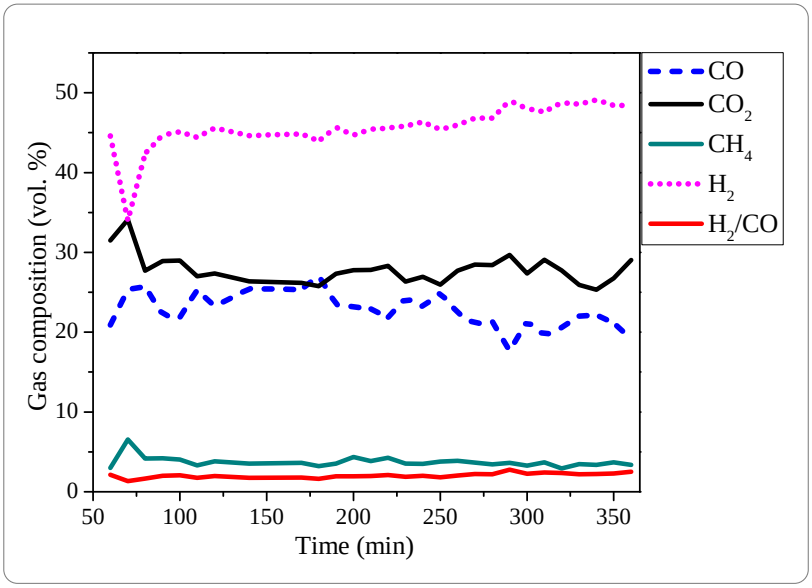

Figure 6.3: Variation in the syngas composition with time; SBR = 0.8, ER = 0.8

6.3 Process flows and, mass and energy balance

Table 6.2 gives the mass flow rate of the components involved in the biomass gasification system. The gasifier is designed for 1000 kg/h biomass consumption rate, utilizing steam and oxygen at a rate of 660 kg/h and 230 kg/h respectively. The exit syngas flow rate is obtained at 1350 kg/h. The residual char and condensed water are produced at 20 and 515.2 kg/h respectively. The exit gas syngas comprises volume fraction of 47% H_2, 22% CO, 27% CO_2 and 4% CH_4. Considering the biomass calorific value of 17.9 MJ/kg, and the evolving syngas calorific value of 10.6 MJ/kg, a 79% gasification efficiency is achieved.

The exit syngas is scrubbed of its CO_2 with the help of a commercially established *Rectisol* technology. Rectisol is a physical acid gas removal process which uses an organic solvent (typically methanol) at subzero temperatures and can purify synthesis gas down to 0.1 vppm total sulphur (including COS) and CO_2 to ppm range. Though sulphur concentrations are low in biomass derived syngas, it is crucial to reduce the H_2S and COS concentration to sub-ppm levels to prevent any catalyst deactivation. CO_2 is known to dissociatively adsorb on the catalyst surface and is hydrogenated to form higher hydrocarbons. Yao et al. [2012] demonstrated the effective hydrogenation of CO_2 on the cobalt catalysts leading to the formation of higher hydrocarbons. However, unlike CO hydrogena-

Table 6.2: Biomass gasification - mass & energy parameter

Input	**m^* (kg/h)**
Biomass	1000
Steam	660
Oxygen	230
Output	**m^* (kg/h)**
Syngas	1350
Char	20
Water	515.2
Syngas composition	
X_{H2}	0.47
X_{CO}	0.22
X_{CO2}	0.27
X_{CH4}	0.04
MW_{syngas}	19.6 kg/kmol
ρ_{syngas}	0.79 kg/m^3
$E_{i-biomass}$	4.9 MW
$E_{o-syngas}$	3.9 MW
$\eta_{gasification}$	79.5%
Syngas composition after CO_2 & CH_4 removal	
X_{H2}	0.68
X_{CO}	0.32
$m^*_{FT-syngas}$	488.5 kg/h

tion, the CO_2 reaction produces methane-rich short chain hydrocarbons. Hence CO_2, if introduced into the FT catalyst bed, acts as an effective reactant, dramatically affecting the reaction stoichiometry, varying the H_2/CO consumption ratio and consequently reducing the syngas conversion rates. The gas stream from Rectisol system consists of syngas with 68.1 vol.% H_2, and 31.9 vol.% CO. The syngas is then compressed to 30 bar before making a single pass through the FT reactor.

The FT unit is a single casing enclosed multi-tubular fixed bed reactor and the catalyst bed is maintained at 503 K and at 3 MPa pressure. The reactor tubes are packed with combustion synthesized 20wt.% Co/SDA catalysts. The syngas conversion and product formation rates in the FT reaction section are considered for varying space velocities - 2610 ml/h*g_{cat}, 1730 ml/h*g_{cat}, 1310

ml/h*g_{cat}, 873.3 ml/h*g_{cat}. In each of the cases, the CO conversions, hydrocarbon selectivity and overall yield are considered from the lab-scale experiments discussed in Chapter 5. Table 6.3 lists the FT reaction details. The packing density of catalyst is estimated to be 850 kg/m^3 and the mass of catalyst used in the FT reaction is calculated by dividing the volumetric syngas flow rate with the WHSV. Based on the mass of the catalyst required for syngas conversion, the reactor is volume is established. The reactor is designed similar to a commercial fixed bed FT reactor, with a singe tube diameter of 0.05 m for a catalyst particle size ranging from 1.5 to 2 mm [Jess and Kern, 2012]. The syncrude leaves the reactor in two separate streams. One stream is in liquid state, consisting primarily of waxes (C_{24+}), hot condensate (C_{12}-C_{24}), cold condensate(C_5-C_{12}) and aqueous product (reaction water, alcohols, carboxylic acids and dissolved paraffins and olefins). The second stream is gas phase products consisting of unconverted syngas and lighter gas phase hydrocarbons. As seen in Table 6.3 a great fraction of input energy remains in the gas phase FT products. A choice predominantly exists to further recycle this gas into the FT reactor or use it in an IC engine for in-house power generation. The wax products are separated and directed to a hydrocracker where they are converted into high quality liquid transportation fuel. Fig 6.4 details the overall description of the BTL unit considered in this study.

Table 6.3: FT reaction - mass & energy variables; T = 503 K, P = 3 MPa

Parameter	**Case 1**	**Case 2**	**Case 3**	**Case 4**
WHSV (ml/h*g_{cat})	2610	1730	1310	873.3
m_{cat} (kg)	451.0	680.4	898.6	1347.9
Reactor volume (m^3)	0.5	0.8	1.1	1.6
ξ_{CO} (%)	42.9	51.2	65.6	73.1
ξ_{H2} (%)	54.7	61.4	66.1	80.6
S_{CH4} (wt.%)	14.6	13.9	12.8	11.4
S_{C2-C5} (wt.%)	8.6	7.9	6.9	5.3
S_{C5+} (wt.%)	75.7	75.6	77.92	78.8
S_{CO2} (wt.%)	1.10	2.49	2.39	4.58
m^*_{C5+} (kg/h)	136.8	161.2	215.0	239.4
$m^*_{fuel-gas}$ (kg/h)	351.7	327.3	273.5	249.2
Calorific Value $_{Fuel-gas}$ (MJ/kg)	27.2	28.3	31.3	32.7
$FT_{liquid-fuel-output}$ (MW)	1.5	1.8	2.4	2.7
$FT_{fuel-gas-output}$ (MW)	2.7	2.6	2.5	2.2
η_{fuels} (% of biomass)	30.6	36.0	48.0	53.5

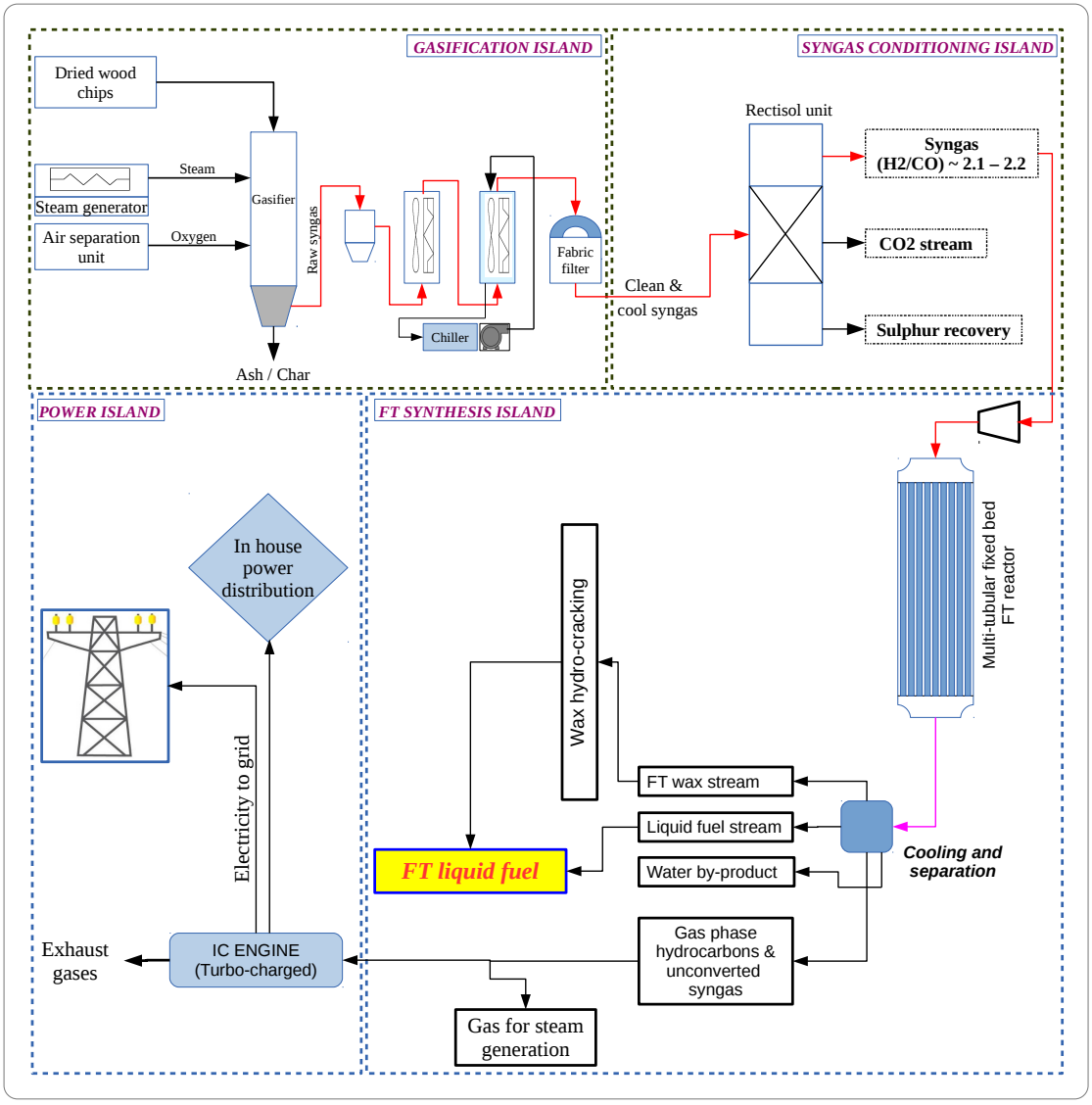

Figure 6.4: Process flow description of the 1000 kg/h biomass to liquid fuel plant, using oxy-steam gasification and Fischer Tropsch synthesis

6.4 Cost analysis

The mass and energy conservation analysis provided particulars related to the maximum hydrocarbon produced for a 1000 kg/h oxy-steam biomass gasifier via FT reaction, using the efficient Co/SDA catalyst developed and tested for a lab-scale setup in Chapter 5. The cost analysis determines the effectiveness of the investment cost with respect to the cost of the liquid-fuel product per unit litre. The assumptions involved in the economic analysis are listed in Table 6.4. All the cost analysis calculations are made using discount factor of 12%, and the costs reported in this techno-economic analysis are considered for the baseline year of 2014-2015. The cost of liquid fuel output (*INR/litre*, or alternatively as *Rs/l*) is calculated based on the annualized life cycle (ALC) of the systems involved. The ALC is evaluated by taking into account the annualized capital cost, annual fuel cost and annualized current value of all the upcoming costs that include, operation and maintenance cost, equipment replacement cost, and electricity cost. The ALC of the liquid fuel is determined by dividing the ALC of the system with the annual liquid product output from the BTL plant. Eqn.6.1 and Eqn.6.2 show the formula for the ALC calculations. Here, C_{cap}, C_{op}, C_m, C_{ele} are the annualized capital cost, annual operation cost, annual maintenance cost, and the annual electricity cost respectively. CRF is the capital recovery factor, d and n are the discount factor and the system life.

$$ALC = \frac{(C_{cap} * CRF) + C_{op} + C_m + C_{ele}}{(m -^{*}_{liq} / \rho -_{liq})} \tag{6.1}$$

$$CRF = \frac{d * (1+d)^n}{(1+d)^n - 1} \tag{6.2}$$

The total operating cost, which is the expenses related to the total man-power required for various plant activities, is Rs 1900/h. The annual maintenance cost is 5% of the total capital cost. Electricity from the grid is obtained at Rs 6/kWh and the plant is operated for 7000 hours annually. The discount factor, which is required to evaluate the net present value of the various operating sub-systems, is assumed to be 12%. The associated capital costs for each of the components are specified in Table 6.5. All the costs are expressed in Indian rupees (INR) and the capital cost were obtained from literature sources, equipment

Table 6.4: Assumptions for economic analysis

Component	**Parameter**
Grid electricity cost (Rs/KWh)	6
Discount factor (%)	12
Annual maintenance cost (Rs)	5% of capital cost
Total plant manpower	19
Per head manpower cost (Rs/h)	100
Daily operational hour (h)	24
Annual operation (days)	300
1 US $ = Rs (Indian Rupees)	67.15 (December 12, 2015)

vendor quotes, industry experts and from the estimates of earlier work [Mahapatra and Dasappa, 2012] [Mahapatra et al., 2009]. A reduced WHSV requires larger FT reactor and liquid fuel processing volumes. Simultaneously, increasing reactor volumes result in elevated capital costs and higher energy requirements. Consequently, the fraction of total capital cost for FT synthesis island increases from 15% to 34% of the total capital cost by decreasing the WHSV from 2760 ml/(h*g_{cat}) to 873.3 ml/(h*g_{cat}). Fig 6.5 shows the increase in the fraction of the overnight-capital cost required for the FT section with decreasing weight hourly space velocity. For higher space velocities, the maximum capital cost is required for installation of oxy-steam gasifier along with the gas cleaning and cooling components. The gas cleaning and cooling unit, which comprises of a cyclone separator, water scrubber, water-chiller and a fabric filter, is a synchronized and customized accessory along with the oxy-steam gasification unit.

6.4.1 Effect of varying WHSV on the liquid fuel cost

By decreasing the WHSV in the FT reactor, the CO conversion increases and consequently the ratio of mass of liquid fuel to the mass of gas phase hydrocarbons (referred to as fuel-gas, which also includes the unconverted syngas), increases. This ratio is termed as the ***fuel ratio***. The BTL system is designed such that a part of the fuel-gas energy is used for generating steam for the gasification reaction and the rest is converted to electricity in an internal combustion engine and exported to the grid at the rate of Rs 6/kWh. Decreasing fractions

Table 6.5: Estimated installed capital, operation and maintenance cost

Unit	**Capacity** (kg/h)	**Power use** (kW_e)	**Capital cost** (Rs)	**Annual O&M cost** (Rs)	**Life** (years)
ASU	250	20	9750000	1927500	10
Steam generator	750	510	1495000	2234750	5
Gasifier	1000	100	30000000	5100000	15
CO_2 separator	820	50	22750000	3297500	10
FT reactor[a]	500	250	15000000	4350000	10
FT reactor[b]	500	250	22500000	4725000	10
FT reactor[c]	500	280	30000000	8700000	10
FT reactor[d]	500	300	45000000	9450000	10
Engine	0.75 MW_e	-	24000000	2220000	10

[a] WHSV = 2610 ml/(h*g_{cat})

[b] WHSV = 1730 ml/(h*g_{cat})

[c] WHSV = 1310 ml/(h*g_{cat})

[d] WHSV = 873.3 ml/(h*g_{cat})

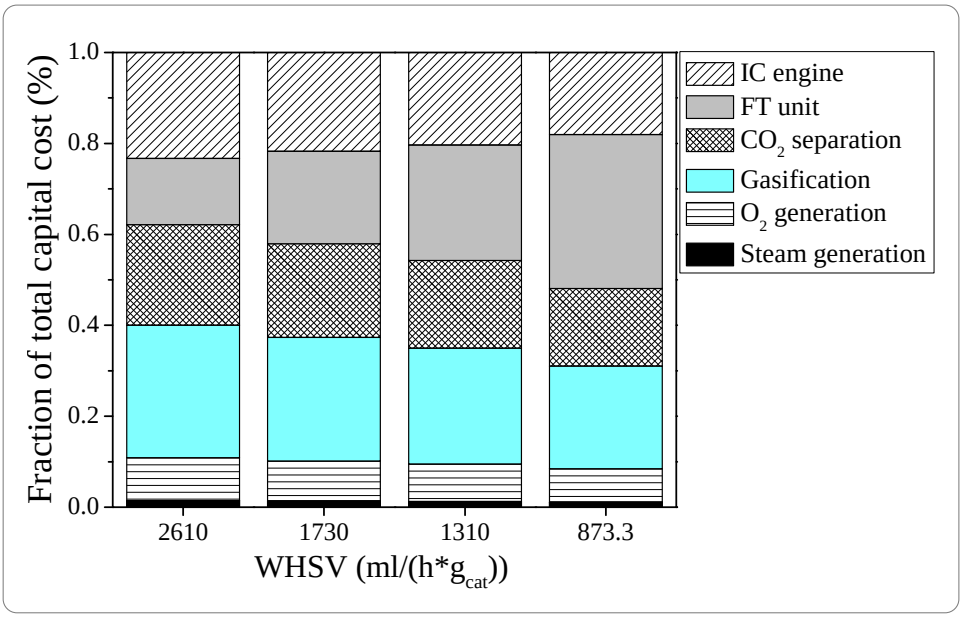

Figure 6.5: Varying capital cost fraction of individual BTL components as a function of decreasing syngas WHSV in the FT unit

of fuel-gas, reduces the net electricity export to the grid. As a result, the cost of electricity per unit kilo watt hour increases and also decreases the gross cash

inflow emerging from the sale of electricity as a product. Fig 6.6 shows a decreasing trend in the net grid electricity export with the increasing fuel ratio and a consequent increase in the effective unit electricity cost. The total electricity available for export to the grid decreases from 0.35 MW_e to 0.17 MW_e as the fuel ratio increases from 0.39 to 0.96.

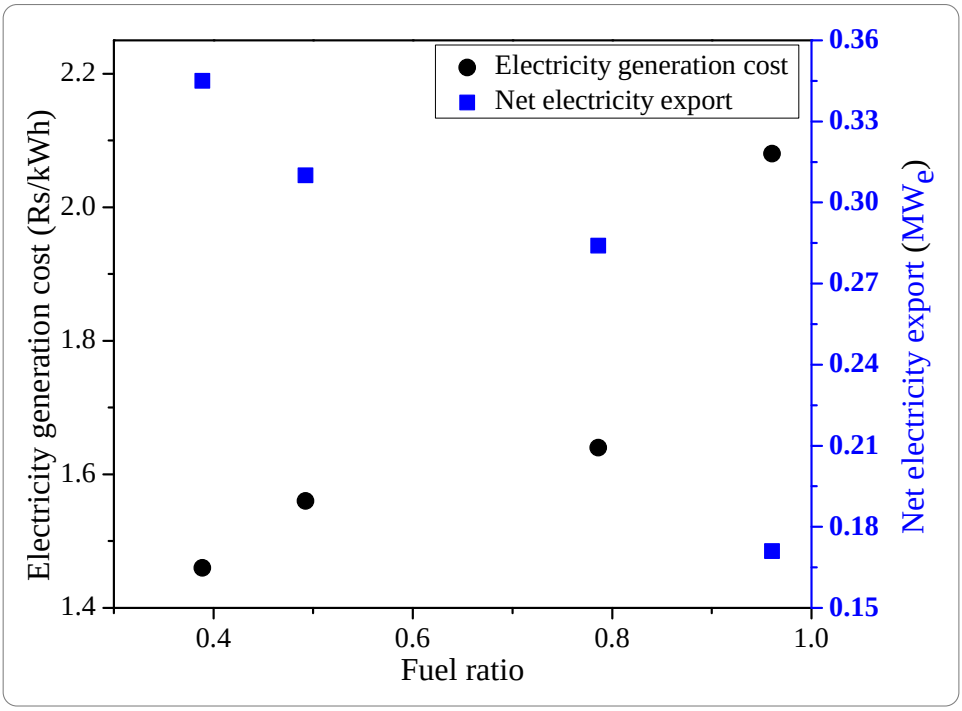

Figure 6.6: Effect of increasing fuel-ratio on the net-grid electricity export and on the electricity generation cost

As the WHSV is reduced from 2610 ml/(h·g_{cat}) to 873.3 ml/(h·g_{cat}), the CO conversion increases from 43% to 73.1% and the hydrocarbon yield increases from 0.28 kg_{C5+}/kg_{syngas}, to 0.49 kg_{C5+}/kg_{syngas}, with a simultaneous decrease in the fuel ratio. Fig 6.7 shows a decrease in the liquid fuel cost with increasing fuel ratio. The unit price of the liquid fuel decreases from Rs 57.80/l to Rs 37.01/l, as the fuel ratio increases from 0.39 to 0.96. Equivalently, the liquid fuel production increases from 1000 tonnes/year to 1800 tonnes/year

A possible way to determine the volume of profitability of a BTL plant, is to estimate the internal rate of return (IRR) for the varying fuel ratio scenarios. A project with a significantly higher IRR value as compared to the other reviewed options, indicates a higher rate of growth that a project is expected to return.

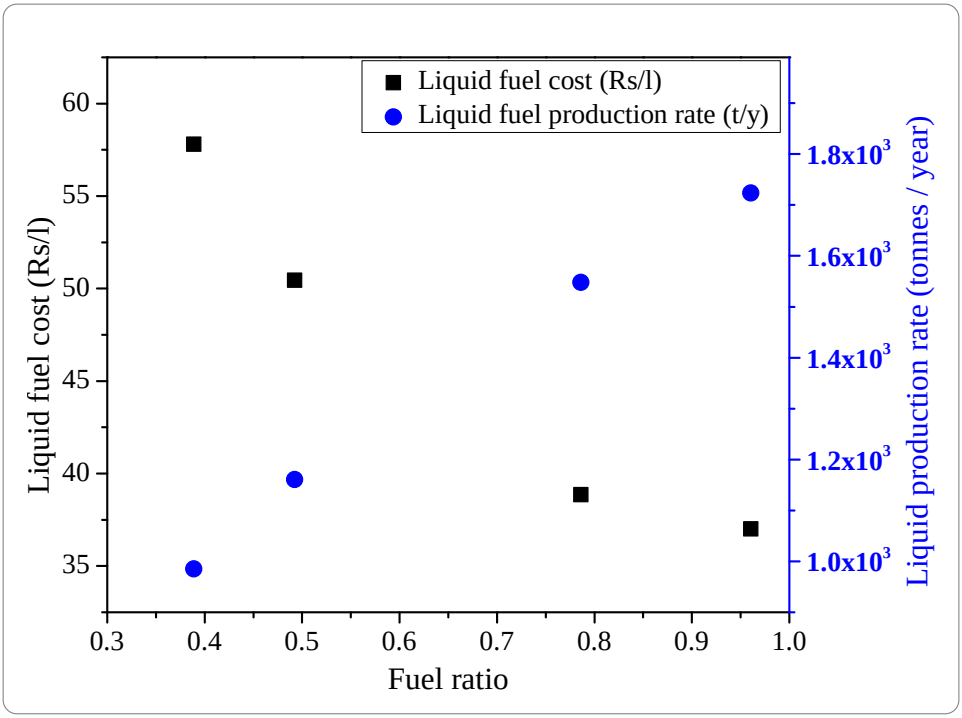

Figure 6.7: Effect of increasing fuel-ratio on annual production rate and the liquid fuel cost

The present diesel cost in India ranges from from Rs 45/litre to Rs 50/litre. For the FT operating condition of 0.39 and 0.49 fuel ratio, the estimated liquid fuel cost is Rs 57.8/litre and Rs 50.4/litre, respectively. Under these conditions, no profits can be obtained by the sale of generated liquid fuels. However, the volume of net profits generated is mainly due to the revenues earned from the export of electricity to the grid at Rs 6/kWh. Even under these conditions, the IRR are 27% and 32% for the BTL plant with the fuel ratio of 0.39 and 0.49, respectively, which is a clear indication of electricity as major co-product of the BTL plant. The net investment of Rs 68000/ton (fuel ratio = 0.4) and Rs 58052/ton (fuel ratio = 0.5) of liquid fuel has a payback period of 4.5 - 5 years. On the other hand, the net investment of Rs 45000/ton (fuel ratio = 0.78) and Rs 41314/ton (fuel ratio = 0.96) of liquid fuel has a payback period of 3 - 3.5 years, with an IRR of 43.17% and 45.06%, considering a liquid fuel selling price of Rs 52.1/l and the export electricity unit price of Rs 6/kWh. These parameters clearly indicate that a BTL plant with the CO conversion greater than 60% (fuel ratio $>$ 0.8) results in an economical and sustainable production of liquid fuels.

Fig 6.8 shows the variation in the internal rate of return for varying liquid fuel selling price. Ideally, if the IRR of the contemplated BTL scenario is greater than demanded rate of return on the total investment, that framework is desirable. In Fig 6.8, for fuel ratio 0.39 and 0.49, the liquid fuel selling price needs to be greater than Rs 40/litre for an IRR $>$ 20%. Above all, under these conditions, the positive revenues for the BTL plants are earned entirely from the sales of generated electricity, instead of liquid fuel. For fuel ratio of 0.96, the IRR increases by 19.7% with a 45% increase in the liquid fuel selling price. Similarly, for the fuel ratio of 0.78, the IRR increases by 15.3% when the liquid fuel selling price increases from its production cost of Rs 38.86/litre to Rs 52.14/litre.

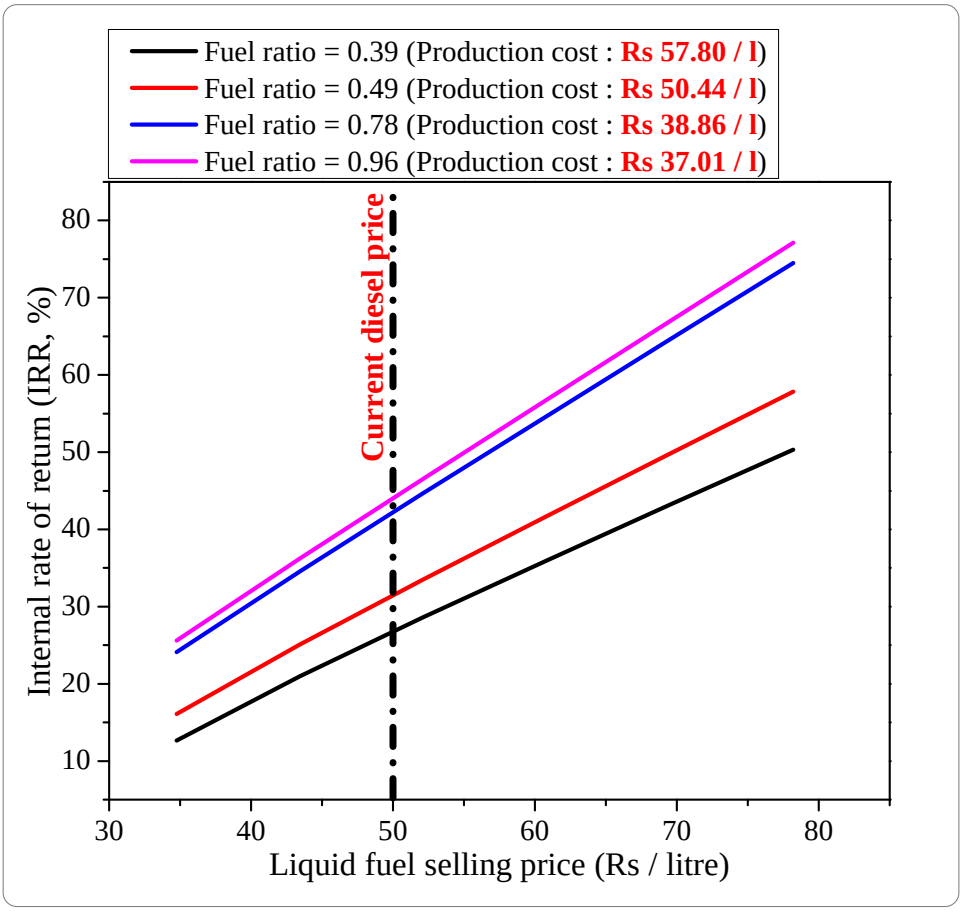

Figure 6.8: Effect of the variation in the liquid fuel cost on the IRR, considered for varying fuel ratios

6.4.2 Sensitivity analysis for cost parameters

Biomass being the raw material, its variation in the cost is bound to extensively affect the liquid fuel cost. Anticipating biomass cost is challenging since it is coupled with several factors, such as local supply chain, resource availability, processing costs, land availability, deforestation risks, simultaneous competitive uses and the sustainability touchstone. Each of these crucial factors influence the biomass cost directly, or indirectly. Above all, the practicability of biomass based power plants is associated with the long term availability of biomass feedstock and low costs. If *wastes* are employed as a source of biomass, which otherwise incur disposal costs, the feedstock costs may be avoided. Similarly, for biomass produced on site, the transportation cost of biomass can be discounted to further reduce the costs of biomass per unit kilogram. Fig 6.9 shows the effect of variation in the cost of liquid fuel with varying biomass cost. The base cost of biomass is considered to be Rs 4/kg and, a two fold increase in the biomass cost increases the fuel cost by 40% - 45%. For a fuel ratio of 0.96, a doubling increase in the biomass cost, elevates the cost of liquid fuel from Rs 37.01/l to Rs 50.4/l. Similarly, for a fuel ratio of 0.4, a two fold increase in the biomass cost, increases the liquid fuel cost from Rs 57.80/l to Rs 86.5/l. The plot clearly indicates that a sustainable and cost effective source of biomass is absolutely essential for continual and propitious operation of the BTL plant.

Identical to the biomass cost, the operation and maintenance (O&M) cost are subject to variation. Hence, an estimate on the effect of variation in the O&M costs on the product cost needs to be evaluated. O&M costs are the expenses incurred in the servicing and repair of associated equipments, staff remuneration, facility planning and management and utility services. During the duration of plant operation, the costs associated with these elements may change, affecting the product cost. Fig 6.10 shows the effect of variation in the O&M costs on the liquid fuel costs. On an average, the cost of liquid fuel increases by 10% to 14% with 50% increase in the O&M cost. Clearly, the percentage increase in the fuel cost with O&M costs is not as severe as the effect caused by the increase in biomass cost.

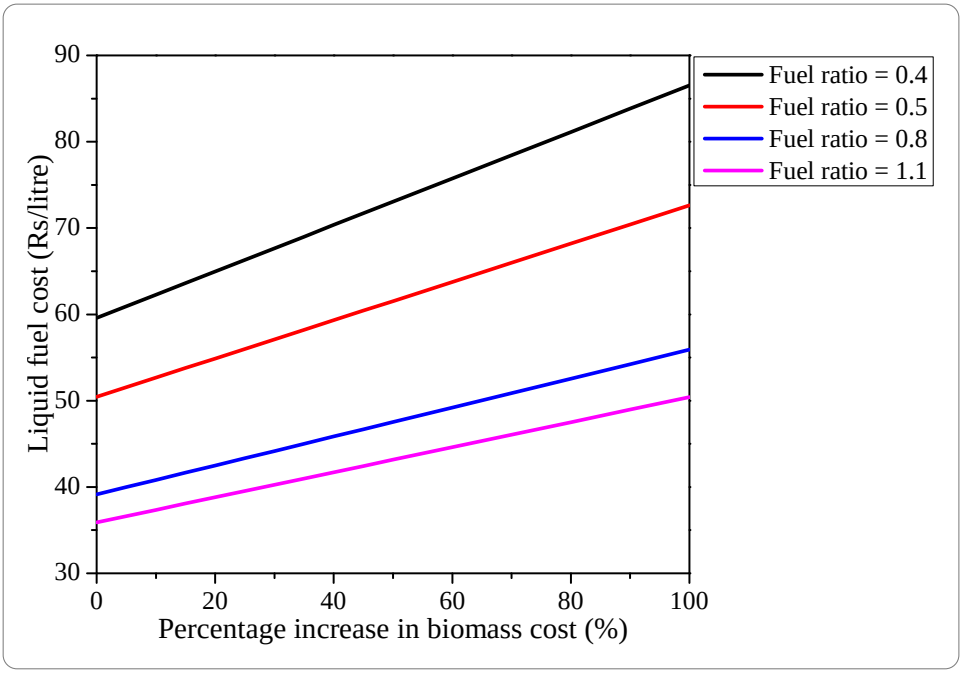

Figure 6.9: Liquid fuel cost variation with variation in the biomass cost

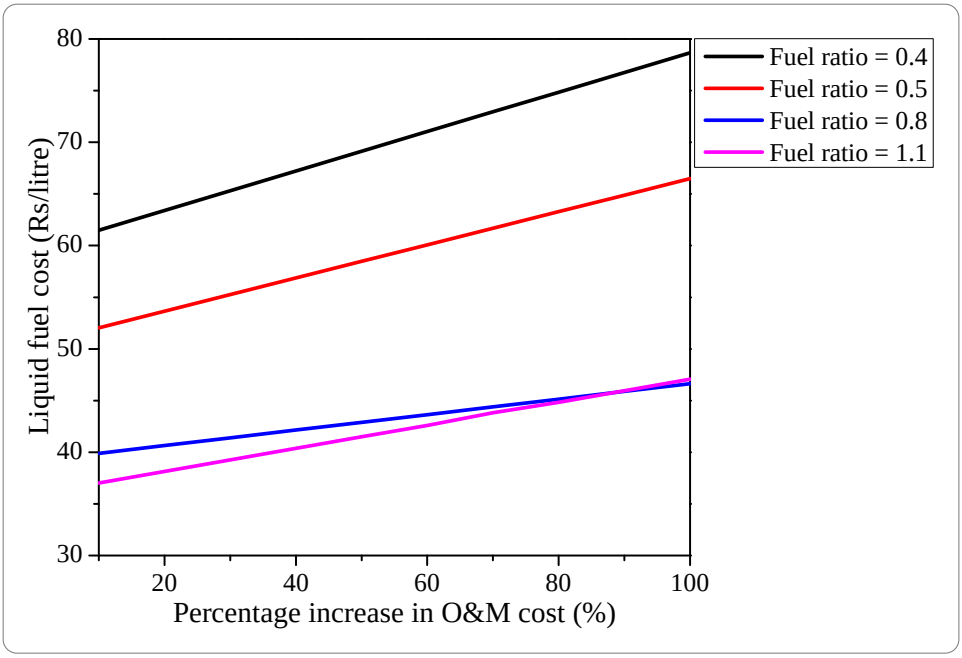

Figure 6.10: Liquid fuel cost variation with variation in the operation and maintenance cost

6.5 Summary

The extensive techno-economic analysis was performed to conduct a feasibility study of a biomass to liquid fuel generation plant. The thermochemical gasification of biomass route to produce liquid fuels via Fischer Tropsch synthesis can be commercially and sustainably established. Four different conversion scales of FT reactors were tested. The syngas conversion to liquid fuels were increased by reducing the WHSV and consequently increasing the CO conversion from 43% to 73%. For a market competitive liquid fuel generation, the CO conversion should be maintained above 60%. It was shown that the liquid fuel cost for CO conversion of 65.6% and 73.1% yielded liquid fuels priced at Rs 39.1/litre and Rs 35.9/litre.

Electricity is a major co-product in the BTL system. Since a major fraction of FT products remain in the gas-phase, it was shown that the combustion of the fuel gas in an IC engine can be used to generate electricity, for export to the grid, sold at Rs 6/kWh. Another major factor affecting the liquid fuel cost, is the price of biomass. The cost analysis has indicated that a 50% increase in the biomass cost results in a 15 to 18% increase in the liquid fuel cost. For a sustainable and long-term operation of the BTL plant, a consistent and economic source of biomass is absolutely crucial.

Chapter 7

Conclusions and future work

This thesis has explored an effective way to convert syngas to liquid fuel via the Fischer Tropsch reaction. Throughout this work, primary focus is fixed towards the conversion of biomass derived syngas to higher hydrocarbons. Syngas used in this study is in a simulated form in pressurized cylinders with the H_2/CO ratio of 2.3:1 (70 vol.% H_2, 30 vol.% CO). The conditions selected for the conversion process in the reactor are 3 MPa and 573 K. The catalyst was synthesized in-house and comprised of various synthesis methods and support materials. Supported cobalt catalysts synthesized by combustion method using novel techniques enhanced the yield of paraffins as compared to the hydrocarbon yield with catalysts synthesized by the conventional incipient wetness impregnation method. The combustion synthesis method developed in this work uniquely enables the FT active metal loading of 20 wt.% over support extrudes for direct use in fixed bed FT reactors. The developed method permits the controlled synthesis of catalysts, which otherwise results in uncontrolled reactions resulting in powdering of catalysts and even loss of active components, particularly for metal loading above 5 wt.%. The dominant catalyst properties that were observed to enhance the hydrocarbon yield are the following:

- Smaller crystallite size (6.5 nm - 10.5 nm)
- Higher degree of cobalt reduction ($\sim$ 92%)
- Lower metal support interaction and hence metal dispersion in the range of 13.2% - 16.1%.

It was important to recognize that the synthesized catalysts should not possess a strong metal support interaction, as usually observed in the case of

Al_2O_3 supported catalysts synthesized by the incipient wetness impregnation method. From the experimental results, it was observed that a strong metal support interaction largely reduces the degree of metal reduction and decreases the fraction of active sites available for the syngas conversion. Harnessing the advantage of high temperature combustion synthesis reaction, the alumina supported cobalt catalysts can be synthesized with decreased concentrations of irreducible cobalt aluminate compounds, that are prevalent in IWI synthesized catalysts. The cobalt aluminate compounds exist in stable form at low calcination temperatures. The formation of these compounds are further reduced with higher redox equivalence ratio, observed for CS-ϕ=1.2 and CS-ϕ=1.5 catalysts.

Contrary to the general understanding, this work additionally reports that in spite of higher reduction temperature, the CS catalysts have higher degree of reduction and high cobalt dispersion. The high reduction temperature for CS catalysts are attributed to the reduction of surface or subsurface Co^{2+} ions in the Co^{2+}-Al^{3+} spinel structure, that continue to get reduced at higher temperatures. It should be noted that the catalysts conditions must be created to enhance the reduction of hardly reducing cobalt support compounds. Furthermore, the catalyst properties listed above also increase the chain growth probability, shifting the product spectrum to favour the formation of waxes (C_{24+}) instead of middle distillates.

An alternative route explored to reduce the metal support interaction and increase the FT activity is by doping the Al_2O_3 support with 40 wt.% SiO_2. The characterization studies revealed an additional reduction in the metal support interaction and a corresponding increase in the degree of cobalt reduction. The fraction of active cobalt sites deposited over SDA supports increased by 11% for CS catalysts, compared to the Al_2O_3 -CS catalysts. Besides the reduction in the metal support interaction, the silica doping into the Al_2O_3 framework results in the generation of stronger Bronsted acid sites and increased fraction of Lewis acid sites on the support surface. The enhanced acid sites that occur due to bridged hydroxyl group formation across Al and Si atoms, shift the hydrocarbon spectrum from waxes to middle distillates owing to the conducive conditions for the considerable cracking of higher hydrocarbons. Therefore, it is important to note that the choice of catalysts under the given process conditions has a strong influence on the hydrocarbon product spectrum.

Overall the combustion synthesized catalysts showed higher FT activity and higher C_{5+} selectivity compared to the IWI catalysts. For alumina supported catalysts, highest syngas conversion was recorded for CS(ϕ=1.2) catalysts, for which an almost two fold increase in the CO conversion was observed compared to Al_2O_3-IWI catalysts. Only a marginal variation in the C_{5+} selectivity was observed for the alumina supported catalysts. For the SDA supported catalysts, the FT activity additionally increased. A 27% increase in the CO conversion was observed for SDA-CS catalysts compared to Al_2O_3 -CS catalysts. Strikingly, the C_2-C_5 hydrocarbon mass fraction for SDA supported catalysts was almost 2.4 times higher than the Al_2O_3 supported catalysts. The higher fraction of gas phase hydrocarbons for SDA support was attributed to the existence of aluminosilicate structure, giving it a zeolite like behaviour. Subsequently, a lower C_{5+} selectivity was recorded for SDA supported catalysts. Furthermore, the hydrocarbon product analysis performed in this thesis confirmed the formation of higher hydrocarbons/waxes (C_{24+}) on the CS catalysts, implying a higher degree of surface polymerization for the CS catalysts. Imperatively, this thesis demonstrated the effect of support on the syngas conversion and the hydrocarbon product spectrum. The SDA supported catalysts, despite higher conversion showed reduced formation of waxes compared to Al_2O_3 supported catalysts. This occurrence was plainly ascribed to the higher fraction of acid sites on SDA supported catalysts, which cause considerable cracking of higher hydrocarbons resulting in the increased fraction of middle distillates instead of waxes. *All this effort resulted in the increased syngas conversion to higher hydrocarbon fuel which included fractions of middle distillates (C_{10}-C_{24}) and waxes (C_{24+}).*

A techno-economic analysis was conducted on the basis of:

- a perceived scale of 1000 kg/h of dry biomass throughput (7200 tonnes/year).
- the availability of substantial experimental data (from a parallel study in the laboratory) that showed that the technology of converting biomass with oxygen-steam combination requires steam to biomass ratio ranging from 0.8 to 1.2 and an equivalence ratio of 0.1, to generate syngas with H_2/CO of 2.1:1.
- the scale of biomass gasifier generating 1100 m^3/h of syngas to yield 1500

tonnes/year of a mix of hydrocarbon fuel (liquid fuel and waxes)

The calculations demonstrated that the market competitive liquid fuel generation can be attained with a CO conversion greater than 60% and the overall energy efficiencies under these conditions vary from 45% to 50%. The techno-economic analysis clearly indicates that a continual and cost effective source of biomass is absolutely essential for sustainable operation of the BTL plant. Locally obtained biomass such as industrial wastes, agricultural residues and municipal solid wastes can be ideally processed as a fuel for syngas production and subsequent conversion to liquid fuels. An economically affordable and environmentally favourable BTL systems present a positively clean carbon neutral liquid fuels, provided the biomass is sustainably grown, transported, converted and consumed. For several developing countries, such as India, biomass to liquid fuel production via Fischer Tropsch synthesis, can be achieved relatively easier as compared to industrialized countries. This is due to the better-growing climates, lower labour costs and in some cases, even lower capital costs.

7.1 Future work

This study has demonstrated an effective utilization of combustion synthesized cobalt catalysts for the conversion of syngas to higher hydrocarbons via FT reactions. It has also led to the evolution of combustion parameters that lead to high syngas conversion efficiencies. Eventually, it is crucial to specify that two kinds of catalysts have been designed and tested - one exclusively for the production of liquid hydrocarbons (diesel) and the other for the production of heavy waxes. In the authors' view, further development in the catalyst properties need to be evolved, especially to synthesize cobalt catalyst in a single step without the need for further reduction. This work is currently advancing.

Appendix A

XRD - instrumental broadening analysis

The widening of diffraction peaks due to the instrumental effect was evaluated using the refinement of the XRD pattern of a silicon polycrystalline standard sample (*ICSD-51688*). Fig A.1 shows the x-ray diffraction pattern for the silicon polycrystalline standard, which is used to evaluate the contribution of instrumental peak broadening. Fig A.2, shows "2-theta" plotted against FWHM (β_{std}) of the Si-polycrystalline x-ray diffraction peaks. The values of β_{std} are obtained for 2-theta peaks of the sample XRD spectrum. The effective FWHM, incorporating the instrumental broadening is evaluated using Eqn.A.1, where β_{crys} is the FWHM of the cobalt catalyst at a given 2-θ and β_{std} is the FWHM of the Si-polycrystalline at the same 2-θ.

$$\beta_e = \sqrt{\beta_{crys}^2 - \beta_{std}^2} \tag{A.1}$$

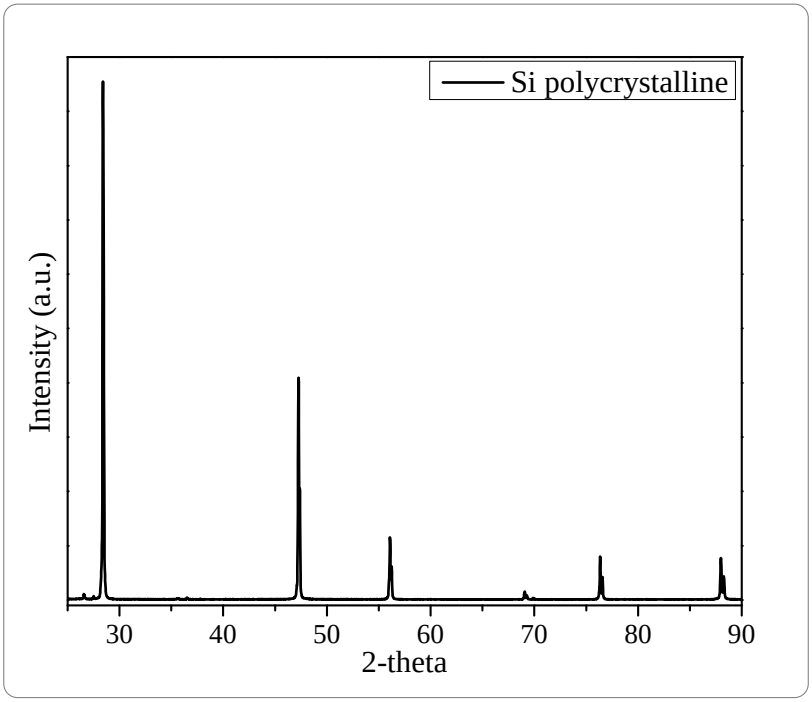

Figure A.1: X-ray diffraction pattern of the Si-polycrystalline standard

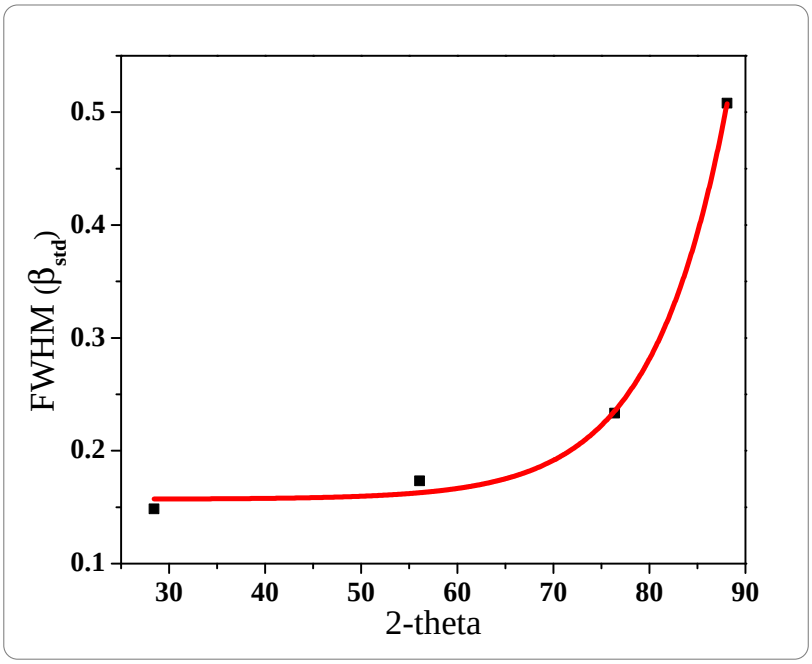

Figure A.2: 2-theta vs FWHM for Si-polycrystalline standard

Appendix B

Gas chromatograph calibration

B.1 GC - TCD-FID

The exit gas composition were analysed by two online gas chromatograms. The Mayura analytical GC-1100 was equipped with a thermal conductivity detector (TCD) to identify, CO, H_2 and CO_2. The hydrocarbon gas products were analysed using an online Perkin Elmer GC, equipped with the FID detector. The methods of analyses for TCD and FID operations are listed in Table B.1.

Table B.1: GC - TCD - FID parameters

GC	***Perkin Elmer - Clarus 680***
Column	Elite - Alumina (Capillary)
Oven ramp rate (K/min)	5
Oven initial temperature (K)	313
Oven final temperature (K)	473
Column length (m)	30
Column i.d. (mm)	0.53
Injector temperature (K)	523 (PSS injector)
Sample injection volume (μL)	5
Detector	FID
Detector temperature (K)	473
Carrier gas	He
Carrier gas flow rate (ml/min)	1
FID - H_2 flow rate (ml/min)	40
FID - Air flow rate (ml/min)	400
GC	***Mayura analytical - GC 1100***
Column	Molecular sieve & HaySep-A (Packed)
Operation	Column switching / Isothermal
Detector	TCD
Oven temperature (K)	313
Carrier gas	He
Carrier gas flow rate (ml/min)	40

The FID is calibrated using standard gas mixtures, as listed in Table B.2.

Table B.2: Calibration factors for the gas phase hydrocarbon standards (C_1 - C_5)

Component	**Retention time** (min)	**Composition** (Vol%)	**Chromatogram area**	**Calibration factor**
CH_4	1.07	4.99	3795.9	1.32e-02
C_2H_6	1.13	5.02	7577.6	6.63e-04
C_2H_4	1.18	5.14	7662.0	6.71e-04
C_2H_2	1.74	5.03	6886.9	7.30e-04
C_3H_8	1.29	5.02	11374.8	4.41e-04
C_3H_6	1.53	5.01	10549.4	4.75e-04
C_4H_{10}	1.8	5.16	14908.7	3.46e-04
C_5H_{12}	3.42	5.16	18166.79	2.84e-04

The chromatogram for the gas phase hydrocarbon standard are shown in Fig B.1

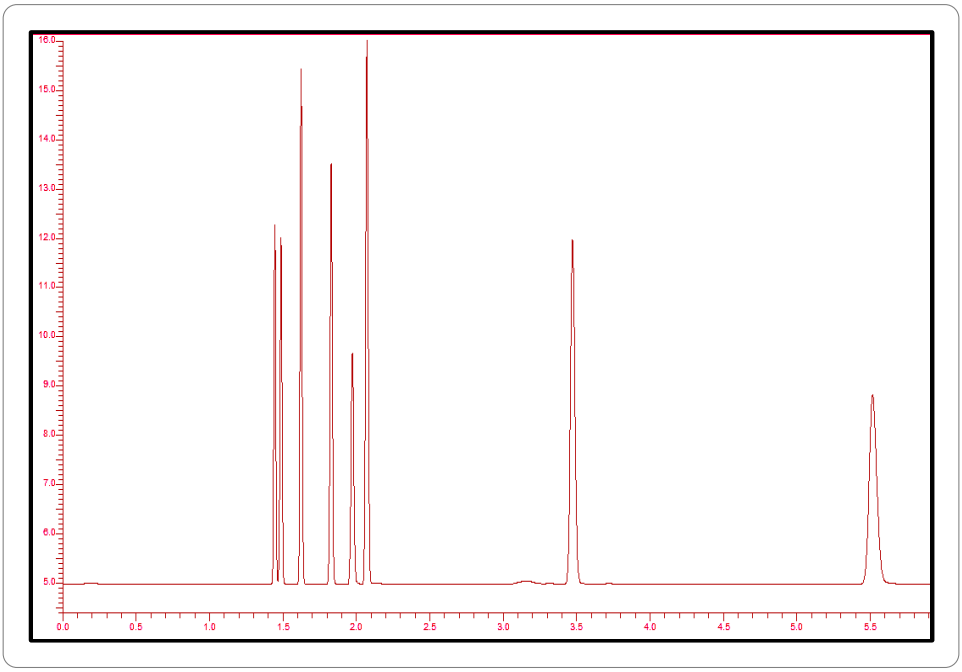

Figure B.1: GC-FID chromatogram for gas phase hydrocarbon standards

B.2 GC - MS

The liquid hydrocarbons are analysed using the Perkin Elmer Clarus SQ8 MS. The hydrocarbon compunds are identified using *NIST 13 Mass Spectral Library*. Fig B.2 shows the chromatogram for the liquid hydrocarbon standards and, the calibration constants for these standards are listed Table B.3.

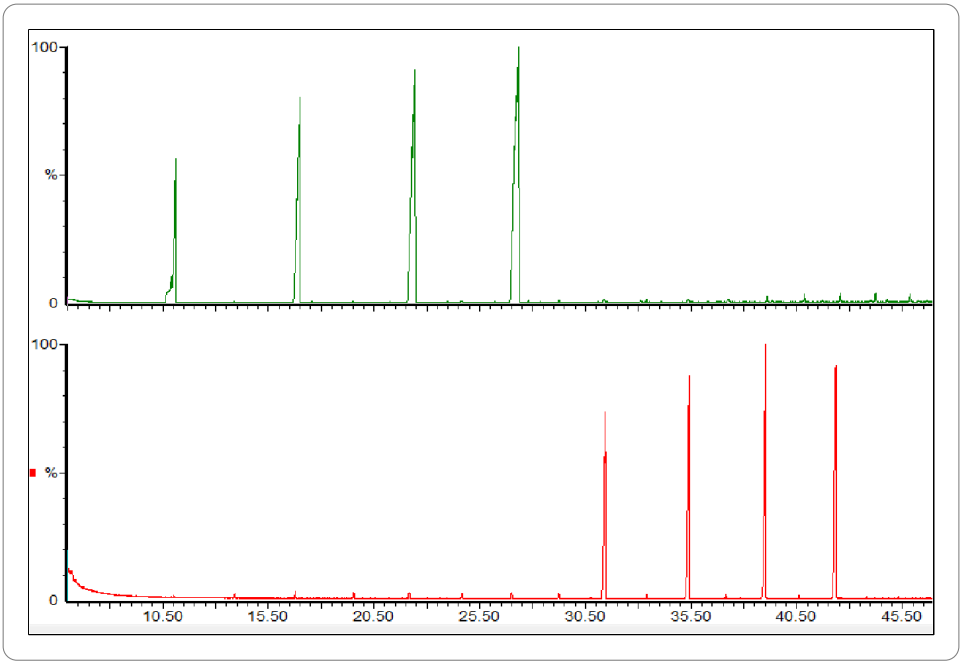

Figure B.2: GC-MS chromatogram for liquid hydrocarbon standards

Table B.3: Calibration factor for liquid hydrocarbon standards (C_{10} - C_{24})

Component	**Retention time** (min)	**Composition** (wt.%)	**Chromatogram area**	**Calibration factor**
$C_{10}H_{22}$	11.07	1.37	8.30e08	1.65e-09
$C_{12}H_{26}$	16.85	1.82	1.32e09	1.38e-09
$C_{14}H_{30}$	22.26	2.28	1.95e09	1.17e-09
$C_{16}H_{34}$	27.11	2.73	2.47e09	1.11e-09
$C_{18}H_{38}$	31.29	2	1.05e09	1.91e-09
$C_{20}H_{42}$	35.24	2	1.09e09	1.84e-09
$C_{22}H_{46}$	38.83	2	1.16e09	1.73e-09
$C_{24}H_{50}$	42.13	2	1.20e09	1.66e-09

Appendix C

FT exit gas composition

The following tables list the exit gas composition measured using an online gas chromatograph and and the exit gas flow rates, as measured using the water displacement technique. The values are recorded at T = 503 K, P = 3 MPa and WHSV = 1730 ml/(h·g_{cat})

Table C.1: FT product gas composition and flow rate for Al_2O_3 - IWI catalysts

Time	**CO**	**CO_2**	**CH_4**	**C_2H_6**	**C_2H_4**	**C_3H_8**	**C_3H_6**	**C_2H_2**	**C_4H_{10}**	**C_5H_{12}**	**H_2**	**F**
(h)	**vol.(%)**											**(l/min)**
0	31.28	0.54	2.10	0.12	0.03	0.06	0.00	0.15	0.03	0.00	76.49	0.13
10	31.20	0.55	2.20	0.13	0.03	0.06	0.00	0.18	0.04	0.00	75.10	0.13
20	30.40	0.57	2.20	0.14	0.04	0.07	0.00	0.19	0.05	0.00	73.10	0.13
30	29.60	0.58	2.40	0.14	0.04	0.07	0.00	0.21	0.04	0.00	68.20	0.13
40	27.38	0.59	2.41	0.15	0.05	0.08	0.00	0.26	0.05	0.02	61.52	0.13
50	28.10	0.58	2.40	0.15	0.05	0.07	0.00	0.26	0.05	0.00	60.30	0.13
60	27.60	0.61	2.30	0.16	0.03	0.08	0.00	0.25	0.05	0.00	61.50	0.13
70	27.40	0.58	2.40	0.15	0.05	0.06	0.00	0.27	0.06	0.00	62.40	0.13
80	27.17	0.60	2.39	0.15	0.05	0.08	0.00	0.26	0.06	0.03	63.03	0.13
90	27.60	0.62	2.30	0.15	0.05	0.06	0.00	0.24	0.04	0.00	63.60	0.13
100	27.60	0.59	2.30	0.15	0.05	0.07	0.00	0.23	0.03	0.00	63.20	0.12
110	27.40	0.58	2.10	0.13	0.04	0.06	0.00	0.18	0.04	0.00	63.80	0.12
120	27.33	0.60	1.93	0.11	0.04	0.05	0.00	0.16	0.02	0.00	63.13	0.12
130	27.80	0.56	2.10	0.12	0.03	0.06	0.00	0.17	0.03	0.00	64.10	0.12
140	27.40	0.55	1.90	0.11	0.04	0.05	0.00	0.16	0.02	0.00	64.30	0.12
150	27.80	0.54	2.10	0.12	0.04	0.04	0.00	0.13	0.02	0.00	64.60	0.12
160	28.01	0.54	1.96	0.11	0.03	0.04	0.00	0.14	0.01	0.00	65.35	0.12

Table C.2: FT product gas composition and flow rate for Al_2O_3 - CS catalysts

Time	**CO**	**CO_2**	**CH_4**	**C_2H_6**	**C_2H_4**	**C_3H_8**	**C_3H_6**	**C_2H_2**	**C_4H_{10}**	**C_5H_{12}**	**H_2**	**F**
(h)	**vol.(%)**											**(l/min)**
0	29.07	0.36	3.34	0.18	0.03	0.12	0.00	0.17	0.05	0.01	62.74	0.11
10	29.20	0.37	3.40	0.19	0.03	0.12	0.00	0.17	0.05	0.01	62.00	0.11
20	29.20	0.40	3.40	0.20	0.03	0.12	0.00	0.17	0.05	0.01	58.80	0.11
30	29.10	0.42	3.50	0.20	0.03	0.13	0.00	0.17	0.05	0.01	54.60	0.11
40	29.15	0.45	3.65	0.21	0.03	0.13	0.00	0.18	0.05	0.01	53.82	0.11
50	29.20	0.43	3.80	0.20	0.03	0.13	0.00	0.18	0.05	0.01	54.60	0.11
60	29.20	0.40	3.40	0.19	0.03	0.13	0.00	0.19	0.06	0.02	55.80	0.10
70	29.20	0.38	3.20	0.19	0.03	0.13	0.00	0.19	0.07	0.02	57.40	0.10
80	29.29	0.35	3.21	0.18	0.03	0.12	0.00	0.19	0.06	0.02	58.56	0.10
90	29.30	0.33	3.50	0.18	0.03	0.12	0.00	0.19	0.06	0.02	60.10	0.10
100	29.20	0.33	3.40	0.18	0.03	0.12	0.00	0.19	0.06	0.02	62.20	0.11
110	29.30	0.31	3.20	0.19	0.03	0.12	0.00	0.19	0.06	0.02	64.50	0.11
120	29.28	0.31	3.37	0.19	0.03	0.12	0.00	0.19	0.06	0.02	65.15	0.11
130	29.30	0.31	3.10	0.19	0.03	0.12	0.00	0.19	0.06	0.02	63.10	0.11
140	29.30	0.30	3.20	0.18	0.03	0.12	0.00	0.19	0.06	0.02	63.40	0.11
150	29.30	0.30	3.50	0.19	0.03	0.12	0.00	0.19	0.06	0.02	62.10	0.11
160	29.28	0.30	3.46	0.19	0.03	0.12	0.00	0.19	0.06	0.02	62.00	0.10

Table C.3: FT product gas composition and flow rate for Al_2O_3 - ϕ=1.2 catalysts

Time	**CO**	**CO_2**	**CH_4**	**C_2H_6**	**C_2H_4**	**C_3H_8**	**C_3H_6**	**C_2H_2**	**C_4H_{10}**	**C_5H_{12}**	**H_2**	**F**
(h)	**vol.(%)**											**(l/min)**
0	23.48	1.80	11.18	0.75	0.02	0.56	0.16	0.03	0.23	0.07	56.08	0.06
10	23.40	1.40	11.30	0.71	0.02	0.55	0.15	0.03	0.21	0.05	56.10	0.06
20	23.60	1.30	10.80	0.68	0.02	0.50	0.15	0.03	0.20	0.04	55.50	0.06
30	24.20	1.20	9.60	0.64	0.02	0.48	0.14	0.03	0.17	0.03	54.20	0.06
40	24.74	1.20	8.50	0.57	0.02	0.41	0.13	0.03	0.16	0.02	53.44	0.06
50	24.80	1.10	8.20	0.54	0.02	0.40	0.13	0.03	0.16	0.02	53.80	0.07
60	25.20	0.80	8.00	0.54	0.02	0.39	0.13	0.03	0.17	0.03	54.10	0.07
70	26.10	0.70	7.80	0.53	0.02	0.39	0.12	0.03	0.17	0.03	54.80	0.07
80	26.12	0.55	7.65	0.51	0.02	0.39	0.13	0.03	0.17	0.03	55.16	0.08
90	26.30	0.60	7.50	0.51	0.02	0.39	0.12	0.03	0.15	0.03	56.20	0.08
100	26.60	0.50	7.40	0.52	0.02	0.38	0.13	0.03	0.16	0.03	56.90	0.08
110	26.40	0.80	7.60	0.52	0.02	0.38	0.12	0.03	0.15	0.03	58.30	0.08
120	26.70	0.82	7.77	0.51	0.02	0.38	0.13	0.02	0.15	0.03	61.31	0.08
130	26.40	0.70	7.40	0.48	0.02	0.38	0.13	0.02	0.15	0.03	61.40	0.08
140	26.20	0.60	7.80	0.47	0.02	0.37	0.12	0.02	0.15	0.03	61.60	0.08
150	26.40	0.80	7.60	0.44	0.02	0.36	0.12	0.02	0.15	0.04	61.40	0.08
160	26.34	0.77	7.45	0.43	0.02	0.36	0.12	0.02	0.15	0.04	61.31	0.08

Table C.4: FT product gas composition and flow rate for Al_2O_3 - ϕ=1.5 catalysts

Time	**CO**	**CO_2**	**CH_4**	**C_2H_6**	**C_2H_4**	**C_3H_8**	**C_3H_6**	**C_2H_2**	**C_4H_{10}**	**C_5H_{12}**	**H_2**	**F**
(h)	**vol.(%)**											**(l/min)**
0	29.34	0.50	4.90	0.30	0.02	0.21	0.11	0.01	0.08	0.02	56.08	0.08
10	28.96	0.54	4.60	0.30	0.02	0.21	0.11	0.01	0.08	0.02	56.10	0.08
20	28.97	0.56	4.70	0.30	0.02	0.21	0.11	0.01	0.08	0.02	55.50	0.08
30	30.10	0.45	4.50	0.30	0.02	0.21	0.11	0.01	0.08	0.02	54.20	0.08
40	28.00	0.38	4.53	0.28	0.02	0.20	0.12	0.00	0.08	0.02	53.44	0.08
50	30.20	0.43	4.70	0.28	0.02	0.20	0.12	0.00	0.08	0.02	53.80	0.08
60	29.90	0.32	4.80	0.28	0.02	0.20	0.12	0.00	0.08	0.02	54.10	0.09
70	29.10	0.29	4.80	0.28	0.02	0.20	0.12	0.00	0.08	0.02	54.80	0.09
80	30.15	0.24	4.91	0.28	0.03	0.19	0.12	0.01	0.08	0.03	55.16	0.09
90	30.15	0.23	4.50	0.28	0.03	0.19	0.12	0.01	0.08	0.03	56.20	0.09
100	29.85	0.33	4.20	0.28	0.03	0.19	0.12	0.01	0.08	0.03	56.90	0.09
110	29.12	0.30	4.00	0.28	0.03	0.19	0.12	0.01	0.08	0.03	58.30	0.10
120	29.98	0.24	3.91	0.24	0.02	0.20	0.16	0.01	0.16	0.06	61.31	0.10
130	30.15	0.23	3.90	0.24	0.02	0.20	0.16	0.01	0.16	0.06	61.40	0.10
140	29.85	0.33	3.90	0.24	0.02	0.20	0.16	0.01	0.16	0.06	61.60	0.10
150	29.12	0.30	3.80	0.24	0.02	0.20	0.16	0.01	0.16	0.06	61.40	0.10
160	29.98	0.30	3.74	0.24	0.03	0.19	0.15	0.00	0.13	0.05	61.31	0.10

Table C.5: FT product gas composition and flow rate for SDA-IWI catalysts

Time	**CO**	**CO_2**	**CH_4**	**C_2H_6**	**C_2H_4**	**C_3H_8**	**C_3H_6**	**C_2H_2**	**C_4H_{10}**	**C_5H_{12}**	**H_2**	**F**
(h)	**vol.(%)**											**(l/min)**
0	27.70	0.27	3.80	0.43	0.00	0.23	0.21	0.00	0.10	0.00	65.40	0.12
10	26.80	0.27	3.60	0.44	0.00	0.24	0.23	0.00	0.10	0.01	65.60	0.12
20	26.20	0.27	3.40	0.47	0.00	0.25	0.25	0.00	0.11	0.01	65.40	0.12
30	25.80	0.27	3.60	0.48	0.00	0.26	0.25	0.00	0.11	0.02	65.30	0.12
40	25.61	0.26	3.50	0.48	0.00	0.26	0.25	0.00	0.11	0.02	65.30	0.12
50	25.60	0.26	3.40	0.49	0.00	0.26	0.26	0.00	0.11	0.02	66.30	0.12
60	25.60	0.26	3.40	0.49	0.00	0.26	0.27	0.00	0.12	0.02	66.80	0.12
70	25.70	0.26	3.30	0.48	0.00	0.26	0.28	0.00	0.12	0.03	67.20	0.13
80	25.65	0.26	3.30	0.49	0.00	0.26	0.28	0.00	0.12	0.03	67.40	0.12
90	25.90	0.25	3.30	0.46	0.00	0.25	0.28	0.00	0.12	0.02	67.10	0.12
100	25.90	0.23	3.20	0.45	0.00	0.25	0.26	0.00	0.12	0.02	66.70	0.12
110	26.10	0.22	3.20	0.44	0.00	0.24	0.26	0.00	0.11	0.02	65.70	0.13
120	26.19	0.22	3.10	0.44	0.00	0.23	0.26	0.00	0.11	0.02	65.20	0.13
130	26.20	0.20	3.20	0.44	0.00	0.23	0.26	0.00	0.11	0.02	66.10	0.12
140	26.20	0.20	3.10	0.44	0.00	0.23	0.26	0.00	0.11	0.02	66.80	0.12
150	26.20	0.19	3.00	0.44	0.00	0.23	0.26	0.00	0.11	0.02	67.20	0.12
160	26.14	0.19	2.90	0.44	0.00	0.22	0.26	0.00	0.11	0.02	67.40	0.12

Table C.6: FT product gas composition and flow rate for SDA-CS catalysts

Time	**CO**	**CO_2**	**CH_4**	**C_2H_6**	**C_2H_4**	**C_3H_8**	**C_3H_6**	**C_2H_2**	**C_4H_{10}**	**C_5H_{12}**	**H_2**	**F**
(h)	**vol.(%)**											**(l/min)**
0	27.03	0.47	6.50	0.60	0.03	0.32	0.30	0.00	0.11	0.00	51.84	0.10
10	27.10	0.48	6.10	0.65	0.03	0.35	0.34	0.00	0.12	0.00	51.52	0.10
20	26.80	0.50	6.60	0.68	0.03	0.38	0.36	0.00	0.15	0.00	51.43	0.09
30	26.60	0.52	7.20	0.72	0.03	0.42	0.39	0.00	0.16	0.00	51.26	0.09
40	26.17	0.53	7.80	0.75	0.03	0.45	0.43	0.00	0.18	0.00	51.13	0.09
50	26.40	0.49	7.90	0.76	0.03	0.46	0.48	0.00	0.20	0.00	50.84	0.09
60	26.50	0.44	7.50	0.78	0.03	0.49	0.50	0.00	0.23	0.00	50.34	0.09
70	26.60	0.42	7.40	0.79	0.03	0.51	0.52	0.00	0.25	0.00	49.49	0.09
80	26.69	0.41	7.61	0.79	0.03	0.52	0.53	0.00	0.27	0.00	47.66	0.09
90	26.63	0.41	7.54	0.79	0.04	0.52	0.52	0.00	0.27	0.00	48.10	0.09
100	26.64	0.39	7.50	0.77	0.03	0.52	0.55	0.00	0.27	0.00	48.40	0.09
110	26.62	0.04	7.46	0.76	0.04	0.51	0.51	0.00	0.27	0.00	48.62	0.09
120	26.60	0.39	7.40	0.75	0.04	0.51	0.50	0.00	0.27	0.00	49.20	0.10
130	26.40	0.38	7.21	0.71	0.04	0.49	0.46	0.00	0.25	0.00	49.00	0.09
140	26.84	0.37	6.84	0.65	0.04	0.42	0.41	0.00	0.25	0.00	50.40	0.10
150	26.94	0.37	6.21	0.58	0.03	0.35	0.34	0.00	0.19	0.00	50.92	0.10
160	27.06	0.36	5.70	0.51	0.03	0.28	0.30	0.00	0.11	0.00	51.40	0.10

Appendix D

XPS - Survey spectra

The survey spectra, also referred to as the wide scan spectra of the catalyst samples are shown in the figures below. The binding energy values for the dominant elements are obtained from the NIST database [Naumkin et al., 2008] and from [Khassin et al., 2001]. For SDA supported cobalt catalysts the inset plots indicate the Al_{2p} and Si_{2p} binding energy peaks.

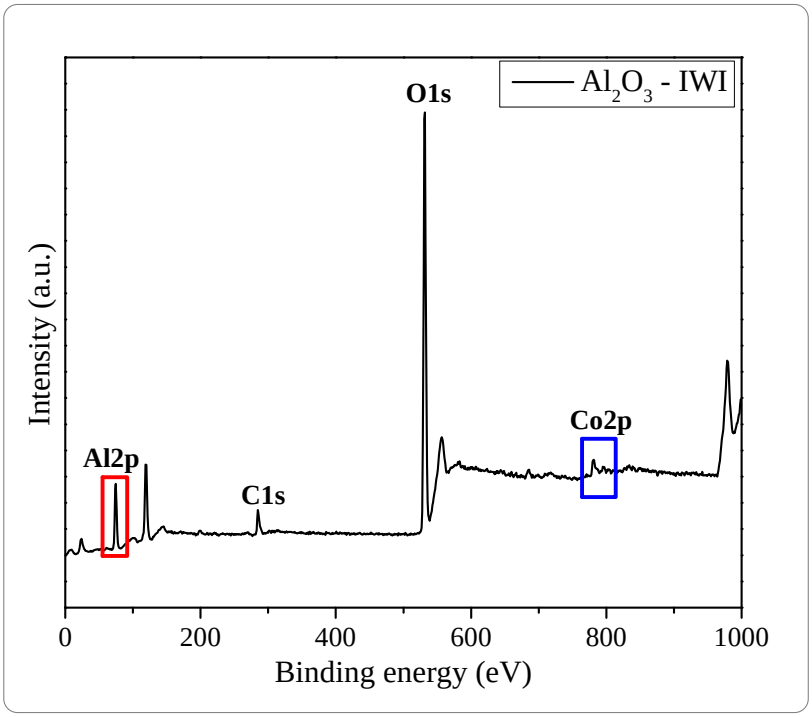

Figure D.1: Survey spectra of Al_2O_3 - IWI cobalt catalysts

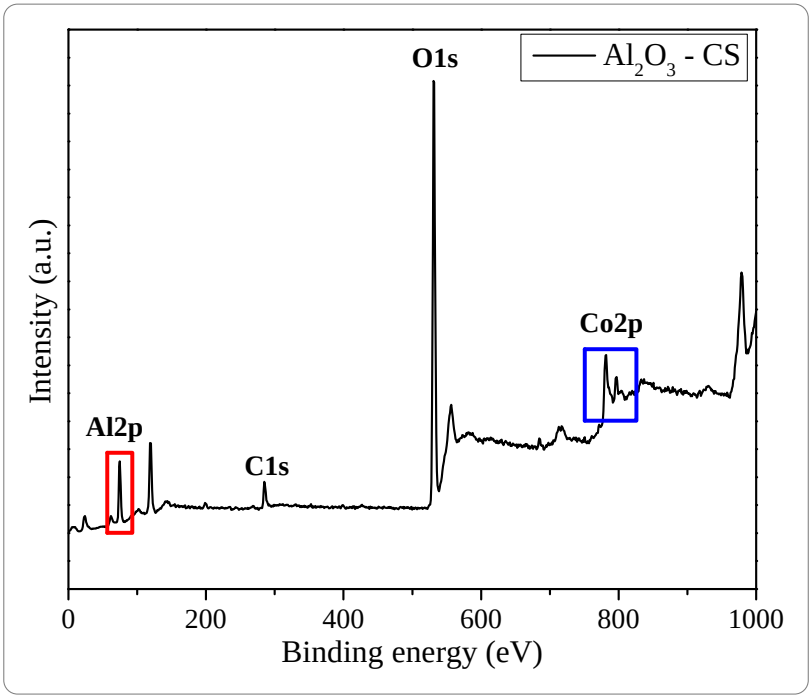

Figure D.2: Survey spectra of Al_2O_3 - CS cobalt catalysts

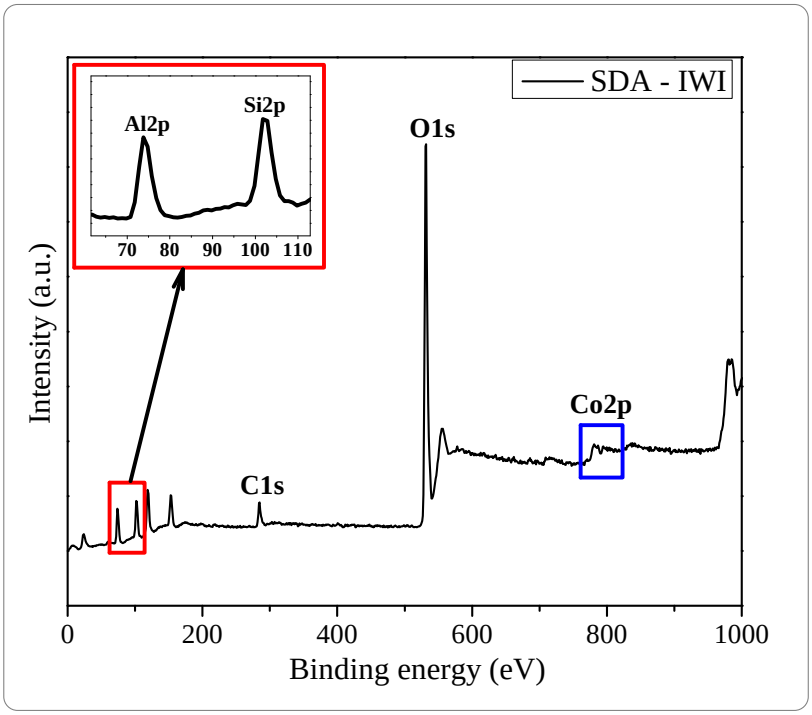

Figure D.3: Survey spectra of SDA - IWI cobalt catalysts

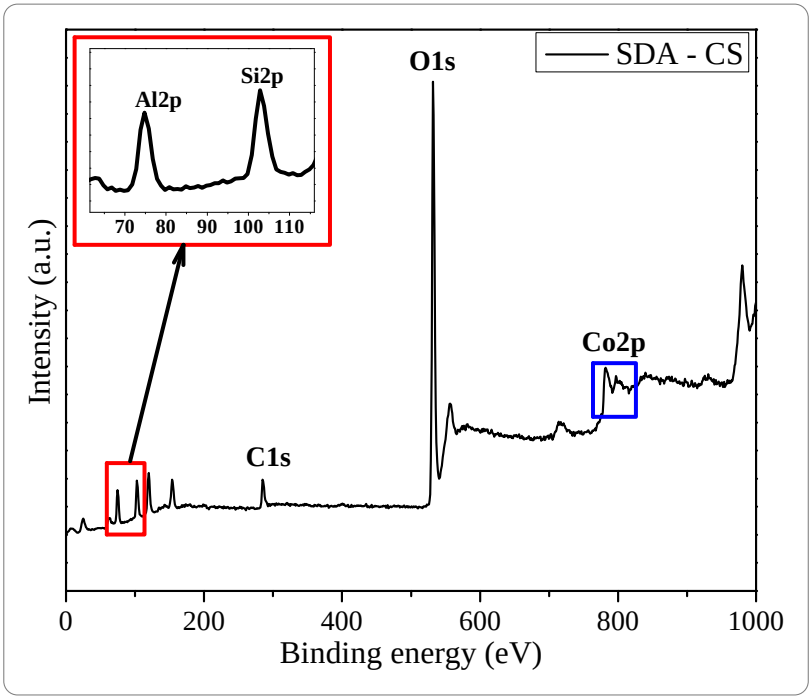

Figure D.4: Survey spectra of SDA - CS cobalt catalysts

Publications

Patent

1. *Snehesh Shivananda Ail & S Dasappa*; Metal catalysts and process for the preparation of catalysts thereof - Indian patent filed - Application number - 6490/CHE/2015

Journal publications

1. *Snehesh Shivananda Ail & S Dasappa*; Biomass to liquid transportation fuel via Fischer Tropsch synthesis - Technology review and current scenario - Renewable and Sustainable Energy Reviews; 58:267-286 (2016)

2. *Snehesh Shivananda Ail & S Dasappa*; Investigations into enhanced wax production with combustion synthesized Fischer Tropsch catalysts - Energy Conversion and Management; 116:80-90 (2016)

3. *Dario Prando, Snehesh Shivananda Ail, David Chiaramonti, Marco Baratieri, S Dasappa*; Characterisation of the producer gas from an open top gasifier: assessment of different tar analysis approaches - Fuel; 181:566-572 (2016)

Conference publications

1. *Prando D, Shivananda S, Karl M, Chiaramonti D, Dasappa S, Baratieri M*; Characterization of tar depositions of three commercial gasification systems - Proceedings of the 23rd European Biomass Conference & Exhibition, Wien (Austria), 2015: 362-365

2. *Snehesh Shivananda Ail & S Dasappa*; Characterization of SiO_2 supported Co catalysts synthesized by solution combustion method for Fischer Tropsch synthesis; - 8th International conference on Environmental Catalysis, Asheville, USA, 2014.

3. *Sandeep K, Snehesh S and S Dasappa*; CO_2 capture through biomass gasification - 19th European Biomass Conference and Exhibition; ISBN-10:88-89407-55-7; 1127-1133; June 2011.

Articles under preparation for Journals

1. Techno-economic analysis of biomass to liquid fuel generation via Fischer Tropsch synthesis - *Energy for Sustainable Development*

2. Investigations into the cobalt-alumina interactions for combustion synthesized Fischer Tropsch catalysts - *Catalysis Science and Technology*

Bibliography

[**Achara et al., 2012**] Nnorom Achara et al. Biofuel from algae. *The Journal of American Science*, 8(1):240–244, 2012.

[**Agwara et al., 2011**] MO Agwara, MD Yufanyi, JN Foba-Tendo, MA Atamba, and Derek Tantoh Ndinteh. Synthesis, characterisation and biological activities of Mn (ii), Co (ii) and Ni (ii) complexes of hexamethylenetetramine. *Journal of chemical and pharmaceutical research*, 3(3):196–204, 2011.

[**Anselm et al., 2011**] Eisentraut Anselm, Adam Brown, and Lew Fulton. *Technology Roadmap : Biofuels for Transport*. International Energy Agency, 2011.

[**Arnoldy and Moulijn, 1985**] P Arnoldy and J A_ Moulijn. Temperature-programmed reduction of CoO/Al_2O_3 catalysts. *Journal of Catalysis*, 93(1):38–54, 1985.

[**Axelson et al., 1967**] G Axelson, U Ericson, A Fahlman, K Hamrin, J Hedman, R Nordberg, C Nordling, and K Siegbahn. New approach to structure studies in organic chemistry. 1967.

[**Bessell, 1993**] Sandra Bessell. Support effects in cobalt-based fischer-tropsch catalysis. *Applied Catalysis A: General*, 96(2):253–268, 1993.

[**Bezemer et al., 2006**] G Leendert Bezemer, Johannes H Bitter, Herman PCE Kuipers, Heiko Oosterbeek, Johannes E Holewijn, Xiaoding Xu, Freek Kapteijn, A Jos van Dillen, and Krijn P de Jong. Cobalt particle size effects in the fischer-tropsch reaction studied with carbon nanofiber supported catalysts. *Journal of the American Chemical Society*, 128(12):3956–3964, 2006.

[**Borg et al., 2007**] Øyvind Borg, Edd A Blekkan, Sigrid Eri, Duncan Akporiaye, Bente Vigerust, Erling Rytter, and Anders Holmen. Effect of calcination atmosphere

and temperature on γ-Al_2O_3 supported cobalt fischer-tropsch catalysts. *Topics in Catalysis*, 45(1-4):39–43, 2007.

[**Bridgwater, 2012**] AV Bridgwater. Review of fast pyrolysis of biomass and product upgrading. *Biomass and Bioenergy*, 38:68–94, 2012.

[**Bridgwater et al., 1999**] AV Bridgwater, D Meier, and D Radlein. An overview of fast pyrolysis of biomass. *Organic Geochemistry*, 30(12):1479–1493, 1999.

[**Brown and Holmgren, 2009**] Robert C Brown and Jennifer Holmgren. Fast pyrolysis and bio-oil upgrading. *Gas*, 13:25, 2009.

[**Bukur et al., 1995**] Dragomir B Bukur, Lech Nowicki, Rama K Manne, and XS Lang. Activation studies with a precipitated iron catalyst for fischer-tropsch synthesis ii. reaction studies. *Journal of Catalysis*, 155(2):366–375, 1995.

[**Butterman and Castaldi, 2009**] H.C. Butterman and M.J. Castaldi. CO_2 as a carbon neutral fuel source via enhanced biomass gasification. *Environmental science & technology*, 43(23):9030–9037, 2009.

[**Camiloti et al., 1999**] AM Camiloti, SL Jahn, ND Velasco, LF Moura, and D Cardoso. Acidity of beta zeolite determined by tpd of ammonia and ethylbenzene disproportionation. *Applied Catalysis A: General*, 182(1):107–113, 1999.

[**Carson et al., 1996**] GA Carson, MH Nassir, and MA Langell. Epitaxial growth of Co_3O_4 on CoO (100). *Journal of Vacuum Science & Technology A*, 14(3): 1637–1642, 1996.

[**Chiche et al., 2013**] David Chiche, Chantal Diverchy, A-C Lucquin, Fabien Porcheron, and Françoise Defoort. Synthesis gas purification. *Oil & Gas Science and Technology–Revue dIFP Energies nouvelles*, 68(4):707–723, 2013.

[**Chisti, 2007**] Yusuf Chisti. Biodiesel from microalgae. *Biotechnology advances*, 25(3): 294–306, 2007.

[**Chisti, 2013**] Yusuf Chisti. Constraints to commercialization of algal fuels. *Journal of biotechnology*, 167(3):201–214, 2013.

[**Conti et al., 2011**] John Conti, Paul Holtberg, LE Doman, et al. International energy outlook 2011. *US Energy Information Administration, Washington, DC, Paper No. DOE/EIA-0484*, 2011.

[**Daniell et al., 2000**] W Daniell, U Schubert, R Glöckler, A Meyer, K Noweck, and H Knözinger. Enhanced surface acidity in mixed alumina–silicas: a low-temperature FTIR study. *Applied Catalysis A: General*, 196(2):247–260, 2000.

[**Dasappa et al., 1989**] S Dasappa, U Shrinivasa, BN Baliga, and HS Mukunda. Five-kilowatt wood gasifier technology: Evolution and field experience. *Sadhana*, 14(3):187–212, 1989.

[**Davis, 2001**] Burtron H Davis. Fischer–tropsch synthesis: current mechanism and futuristic needs. *Fuel processing technology*, 71(1):157–166, 2001.

[**Davis, 2003**] Burtron H Davis. Fischer-tropsch synthesis: relationship between iron catalyst composition and process variables. *Catalysis Today*, 84(1):83–98, 2003.

[**de Klerk, 2011**] A. de Klerk. Fischer–tropsch facilities at a glance. *Fischer-Tropsch Refining*, pages 1–20, 2011.

[**Demirbas, 2011**] M Fatih Demirbas. Biofuels from algae for sustainable development. *Applied Energy*, 88(10):3473–3480, 2011.

[**Dhillon and von Wuehlisch, 2013**] RS Dhillon and George von Wuehlisch. Mitigation of global warming through renewable biomass. *Biomass and Bioenergy*, 48: 75–89, 2013.

[**Di et al., 2013**] Zuoxing Di, Cheng Yang, Xuejing Jiao, Jianqing Li, Jinhu Wu, and Dongke Zhang. A ZSM-5/MCM-48 based catalyst for methanol to gasoline conversion. *Fuel*, 104:878–881, 2013.

[**Fraenkel and Gates, 1980**] Dan Fraenkel and Bruce C Gates. Shape-selective fischer-tropsch synthesis catalyzed by zeolite-entrapped cobalt clusters. *Journal of the American Chemical Society*, 102(7):2478–2480, 1980.

[**Gangwar et al., 2015**] Jitendra Gangwar, Bipin Kumar Gupta, Surya Kant Tripathi, and Avanish Kumar Srivastava. Phase dependent thermal and spectroscopic responses of Al_2O_3 nanostructures with different morphogenesis. *Nanoscale*, 7 (32):13313–13344, 2015.

[**Gaube and Klein, 2008**] Johann Gaube and H-F Klein. Studies on the reaction mechanism of the fischer–tropsch synthesis on iron and cobalt. *Journal of Molecular Catalysis A: Chemical*, 283(1):60–68, 2008.

[**Gerakines et al., 1994**] PA Gerakines, WA Schutte, JM Greenberg, and Ewine F van Dishoeck. The infrared band strengths of H_2O, CO and CO_2 in laboratory simulations of astrophysical ice mixtures. *arXiv preprint astro-ph/9409076*, 1994.

[**Goyal et al., 2008**] HB Goyal, Diptendu Seal, and RC Saxena. Bio-fuels from thermochemical conversion of renewable resources: a review. *Renewable and Sustainable Energy Reviews*, 12(2):504–517, 2008.

[**Guettel et al., 2008**] R. Guettel, U. Kunz, and T. Turek. Reactors for fischer-tropsch synthesis. *Chemical engineering & technology*, 31(5):746–754, 2008.

[**Gutiérrez et al., 2001**] Gonzalo Gutiérrez, Adrian Taga, and Börje Johansson. Theoretical structure determination of γ-Al_2O_3. *Physical Review B*, 65(1):012101, 2001.

[**Hamelinck and Faaij, 2006**] C.N. Hamelinck and A.P.C. Faaij. Outlook for advanced biofuels. *Energy Policy*, 34(17):3268–3283, 2006.

[**Jacobs et al., 2002**] Gary Jacobs, Tapan K Das, Yongqing Zhang, Jinlin Li, Guillaume Racoillet, and Burtron H Davis. Fischer–tropsch synthesis: support, loading, and promoter effects on the reducibility of cobalt catalysts. *Applied Catalysis A: General*, 233(1):263–281, 2002.

[**Jean-Marie et al., 2009**] Alan Jean-Marie, Anne Griboval-Constant, Andrei Y Khodakov, and Fabrice Diehl. Cobalt supported on alumina and silica-doped alumina: Catalyst structure and catalytic performance in fischer–tropsch synthesis. *Comptes Rendus Chimie*, 12(6):660–667, 2009.

[**Jess and Kern, 2012**] Andreas Jess and Christoph Kern. Influence of particle size and single-tube diameter on thermal behavior of fischer-tropsch reactors. part i. particle size variation for constant tube size and vice versa. *Chemical Engineering & Technology*, 35(2):369–378, 2012.

[**Ji et al., 2000**] L Ji, J Lin, and HC Zeng. Metal-support interactions in Co/Al_2O_3 catalysts: a comparative study on reactivity of support. *The Journal of Physical Chemistry B*, 104(8):1783–1790, 2000.

[**Kababji et al., 2009**] AH Kababji, B Joseph, and JT Wolan. Silica-supported cobalt catalysts for fischer–tropsch synthesis: effects of calcination temperature and support surface area on cobalt silicate formation. *Catalysis letters*, 130(1-2): 72–78, 2009.

[**Keyvanloo et al., 2014**] Kamyar Keyvanloo, Maryam Khosravi Mardkhe, Todd M Alam, Calvin H Bartholomew, Brian F Woodfield, and William C Hecker. Supported iron fischer–tropsch catalyst: Superior activity and stability using a thermally stable silica-doped alumina support. *ACS Catalysis*, 4(4):1071–1077, 2014.

[**Khassin et al., 2001**] Alexander A Khassin, Tamara M Yurieva, Vasiliy V Kaichev, Valerii I Bukhtiyarov, Anna A Budneva, Evgeniy A Paukshtis, and Valentin N Parmon. Metal–support interactions in cobalt-aluminum co-precipitated catalysts: XPS and CO adsorption studies. *Journal of Molecular Catalysis A: Chemical*, 175(1):189–204, 2001.

[**Khobragade et al., 2012**] Murnal Khobragade, Sachchit Majhi, and KK Pant. Effect of K and CeO_2 promoters on the activity of Co/SiO_2 catalyst for liquid fuel production from syngas. *Applied Energy*, 94:385–394, 2012.

[**Khodakov et al., 2007**] Andrei Y Khodakov, Wei Chu, and Pascal Fongarland. Advances in the development of novel cobalt fischer-tropsch catalysts for synthesis of long-chain hydrocarbons and clean fuels. *Chemical Reviews*, 107(5):1692–1744, 2007.

[**Kim et al., 2004**] Hak-Joo Kim, Bo-Seung Kang, Min-Ju Kim, Young Moo Park, Deog-Keun Kim, Jin-Suk Lee, and Kwan-Young Lee. Transesterification of vegetable oil to biodiesel using heterogeneous base catalyst. *Catalysis today*, 93:315–320, 2004.

[**Krishna and Sie, 2000**] R. Krishna and ST Sie. Design and scale-up of the fischer–tropsch bubble column slurry reactor. *Fuel Processing Technology*, 64(1):73–105, 2000.

[**Larson et al., 2009**] Eric D Larson, Haiming Jin, and Fuat E Celik. Large-scale gasification-based coproduction of fuels and electricity from switchgrass. *Biofuels, Bioproducts and Biorefining*, 3(2):174–194, 2009.

[**LeViness et al., 2014**] Steve LeViness, Soumitra R Deshmukh, Laura A Richard, and Heinz J Robota. Velocys fischer–tropsch synthesis technologynew advances on state-of-the-art. *Topics in Catalysis*, 57(6-9):518–525, 2014.

[**Lira et al., 2008**] Estephanía Lira, Carmen M López, Freddy Oropeza, Mónica Bartolini, Juan Alvarez, Mireya Goldwasser, Francisco López Linares, Jean-François Lamonier, and M Josefina Pérez Zurita. Hms mesoporous silica as cobalt support for the fischer–tropsch synthesis: Pretreatment, cobalt loading and particle size effects. *Journal of Molecular Catalysis A: Chemical*, 281(1): 146–153, 2008.

[**Liu et al., 2012**] Xiaowei Liu, Andres F Clarens, and Lisa M Colosi. Algae biodiesel has potential despite inconclusive results to date. *Bioresource technology*, 104: 803–806, 2012.

[**Lónyi and Valyon, 2001**] Ferenc Lónyi and József Valyon. On the interpretation of the NH_3-TPD patterns of H-ZSM-5 and H-mordenite. *Microporous and Mesoporous Materials*, 47(2):293–301, 2001.

[**Mahapatra and Dasappa, 2012**] Sadhan Mahapatra and S Dasappa. Rural electrification: optimising the choice between decentralised renewable energy sources and grid extension. *Energy for Sustainable Development*, 16(2):146–154, 2012.

[**Mahapatra et al., 2009**] Sadhan Mahapatra, HN Chanakya, and S Dasappa. Evaluation of various energy devices for domestic lighting in india: technology, economics and CO_2 emissions. *Energy for Sustainable Development*, 13(4): 271–279, 2009.

[**Mardkhe et al., 2014**] Maryam Khosravi Mardkhe, Kamyar Keyvanloo, Calvin H Bartholomew, William C Hecker, Todd M Alam, and Brian F Woodfield. Acid site properties of thermally stable, silica-doped alumina as a function of silica/alumina ratio and calcination temperature. *Applied Catalysis A: General*, 482:16–23, 2014.

[**Medina et al., 2010**] C Medina, R García, P Reyes, JLG Fierro, and N Escalona. Fischer tropsch synthesis from a simulated biosyngas feed over $Co(x)/SiO_2$ catalysts: Effect of co-loading. *Applied Catalysis A: General*, 373(1):71–75, 2010.

[**Meehl et al., 2005**] Gerald A Meehl, Warren M Washington, William D Collins, Julie M Arblaster, Aixue Hu, Lawrence E Buja, Warren G Strand, and Haiyan Teng. How much more global warming and sea level rise? *Science*, 307(5716): 1769–1772, 2005.

[**Moore and Feng, 1995**] John J Moore and HJ Feng. Combustion synthesis of advanced materials: Part I. Reaction parameters. *Progress in Materials Science*, 39(4): 243–273, 1995.

[**Mukasyan et al., 2007**] Alexander S Mukasyan, Paul Epstein, and Peter Dinka. Solution combustion synthesis of nanomaterials. *Proceedings of the Combustion Institute*, 31(2):1789–1795, 2007.

[**Mukasyan and Dinka, 2007**] AS Mukasyan and P Dinka. Novel approaches to solution-combustion synthesis of nanomaterials. *International Journal of Self-Propagating High-Temperature Synthesis*, 16(1):23–35, 2007.

[**Mukunda, 2011**] HS Mukunda. *Understanding clean energy and fuels from biomass*. Wiley India, 2011.

[**Naumkin et al., 2008**] Alexander V Naumkin, Anna Kraut-Vass, and Cedric John Powell. *NIST X-ray photoelectron spectroscopy database*. Measurement Services Division of the National Institute of Standards and Technology (NIST) Technology Services, 2008.

[**O'NEILL, 1994**] H O'NEILL. Temperature dependence of the cation distribution in $CoAl_2O_4$ spinel. *European Journal of Mineralogy*, 6(5):603–609, 1994.

[**Pachauri et al., 2014**] Rajendra K Pachauri, MR Allen, VR Barros, J Broome, W Cramer, R Christ, JA Church, L Clarke, Q Dahe, P Dasgupta, et al. Climate change 2014: Synthesis report. contribution of working groups i, ii and iii to the fifth assessment report of the intergovernmental panel on climate change. 2014.

[**Pandey and Press, 2009**] Ashok Pandey and CRC Press. *Handbook of plant-based biofuels*. CRC Press Boca Raton, 2009.

[**Patil et al., 2008**] KC Patil, MS Hegde, Tanu Rattan, ST Aruna, and World Scientific . Chemistry of nanocrystalline oxide materials-combustion synthesis, properties and applications. 2008.

[**Penn, 1976**] David R Penn. Quantitative chemical analysis by esca. *Journal of Electron Spectroscopy and Related Phenomena*, 9(1):29–40, 1976.

[**Pereira et al., 2011**] Clara Pereira, José F Silva, André M Pereira, João P Araújo, Ginesa Blanco, Jose M Pintado, and Cristina Freire. [VO (acac) 2] hybrid catalyst: from complex immobilization onto silica nanoparticles to catalytic application in the epoxidation of geraniol. *Catalysis Science & Technology*, 1 (5):784–793, 2011.

[**Phienluphon et al., 2014**] Rungravee Phienluphon, Lei Shi, Jian Sun, Wenqi Niu, Peng Lu, Pengfei Zhu, Tharapong Vitidsant, Yoshiharu Yoneyama, Qingjun Chen, and Noritatsu Tsubaki. Ruthenium promoted cobalt catalysts prepared by an autocombustion method directly used for fischer–tropsch synthesis without further reduction. *Catalysis Science & Technology*, 4(9):3099–3107, 2014.

[**Powell and Larson, 1978**] CJ Powell and PE Larson. Quantitative surface analysis by X-ray photoelectron spectroscopy. *Applications of Surface Science*, 1(2): 186–201, 1978.

[**Pradhan et al., 2009**] A Pradhan, DS Shrestha, A McAloon, W Yee, M Haas, JA Duffield, and H Shapouri. Energy life-cycle assessment of soybean biodiesel. *United States, Department of Agriculture, Agricultural Economic Report*, (845), 2009.

[**Prakash et al., 2002**] AS Prakash, AMA Khadar, KC Patil, and MS Hegde. Hexamethylenetetramine: A new fuel for solution combustion synthesis of complex metal oxides. *Journal of Materials Synthesis and Processing*, 10(3):135–141, 2002.

[**Rafiq et al., 2011**] Muhammad Hamid Rafiq, Hugo Atle Jakobsen, Rudolf Schmid, and Johan Einar Hustad. Experimental studies and modeling of a fixed bed reactor for fischer–tropsch synthesis using biosyngas. *Fuel processing technology*, 92(5):893–907, 2011.

[**Regalbuto, 2006**] John Regalbuto. *Catalyst preparation: science and engineering*. CRC Press, 2006.

[**Sandeep and Dasappa, 2014**] K Sandeep and S Dasappa. Oxy–steam gasification of biomass for hydrogen rich syngas production using downdraft reactor configuration. *International Journal of Energy Research*, 38(2):174–188, 2014.

[**Schanke et al., 1995**] D Schanke, S Vada, EA Blekkan, AM Hilmen, A Hoff, and A Holmen. Study of Pt-promoted cobalt CO hydrogenation catalysts. *Journal of Catalysis*, 156(1):85–95, 1995.

[**Schuchardt et al., 1998**] Ulf Schuchardt, Ricardo Sercheli, and Rogério Matheus Vargas. Transesterification of vegetable oils: a review. *Journal of the Brazilian Chemical Society*, 9(3):199–210, 1998.

[**Schulz, 2003**] Hans Schulz. Major and minor reactions in fischer–tropsch synthesis on cobalt catalysts. *Topics in catalysis*, 26(1):73–85, 2003.

[**Schulz et al., 2005**] Hans Schulz, Thomas Riedel, and Georg Schaub. Fischer–tropsch principles of CO-hydrogenation on iron catalysts. *Topics in catalysis*, 32(3-4): 117–124, 2005.

[**Scofield, 1976**] J Hrn Scofield. Hartree-slater subshell photoionization cross-sections at 1254 and 1487 eV. *Journal of Electron Spectroscopy and Related Phenomena*, 8(2):129–137, 1976.

[**Scott et al., 1999**] Donald S Scott, Piotr Majerski, Jan Piskorz, and Desmond Radlein. A second look at fast pyrolysis of biomass - the rti process. *Journal of Analytical and Applied Pyrolysis*, 51(1):23–37, 1999.

[**Sharma et al., 2012**] Pankaj Sharma, Jeong-gu Yeo, Dong Kook Kim, and Churl Hee Cho. Organic additive free synthesis of mesoporous naoncrystalline NaA zeolite using high concentration inorganic precursors. *Journal of Materials Chemistry*, 22(7):2838–2843, 2012.

[**Shi et al., 2011**] Lei Shi, Kai Tao, Tokimasa Kawabata, Takeshi Shimamura, Xue Jun Zhang, and Noritatsu Tsubaki. Surface impregnation combustion method to prepare nanostructured metallic catalysts without further reduction: As-burnt Co/SiO_2 catalysts for fischer–tropsch synthesis. *ACS Catalysis*, 1(10):1225–1233, 2011.

[**Shi et al., 2012**] Lei Shi, Yuzhou Jin, Chuang Xing, Chunyang Zeng, Tokimasa Kawabata, Kouji Imai, Kenji Matsuda, Yisheng Tan, and Noritatsu Tsubaki. Studies on surface impregnation combustion method to prepare supported Co/SiO_2 catalysts and its application for fischer–tropsch synthesis. *Applied Catalysis A: General*, 435:217–224, 2012.

[**Siegbahn et al., 1967**] K Siegbahn, C Nordling, A Fahlman, R Nordberg, K Harmin, J Hedman, G Johansson, T Bergmark, SE Karlsson, J Lindgren, and B Lindberg. Esca, atomic molecular and solid state structure studied by means of electron spectroscopy. *Soc. Sci. Ups*, 20, 1967.

[**Sieminski, 2014**] Adam Sieminski. International energy outlook. 2014.

[**Soled et al., 1990**] S Soled, E Iglesia, and RA Fiato. Activity and selectivity control in iron catalyzed fischer-tropsch synthesis. *Catalysis Letters*, 7(1-4):271–280, 1990.

[**Soled et al., 2003**] Stuart L Soled, Enrique Iglesia, Rocco A Fiato, Joseph E Baumgartner, Hilda Vroman, and Sabato Miseo. Control of metal dispersion and structure by changes in the solid-state chemistry of supported cobalt fischer–tropsch catalysts. *Topics in catalysis*, 26(1-4):101–109, 2003.

[**Steynberg and Dry, 2004**] André Steynberg and Mark Dry. *Fischer-Tropsch Technology*. Elsevier, 2004.

[**Steynberg et al., 2004**] AP Steynberg, ME Dry, BH Davis, and BB Breman. Fischer-tropsch reactors. *Studies in surface Science and Catalysis*, 152:64–195, 2004.

[**Storsæter et al., 2005**] Sølvi Storsæter, Bård Tøtdal, John C Walmsley, Bjørn Steinar Tanem, and Anders Holmen. Characterization of alumina-, silica-, and titania-supported cobalt fischer–tropsch catalysts. *Journal of catalysis*, 236(1):139–152, 2005.

[**Sun et al., 2000**] Shouli Sun, Noritatsu Tsubaki, and Kaoru Fujimoto. The reaction performances and characterization of fischer–tropsch synthesis Co/SiO_2 catalysts prepared from mixed cobalt salts. *Applied Catalysis A: General*, 202(1): 121–131, 2000.

[**Tock et al., 2010**] Laurence Tock, Martin Gassner, and François Maréchal. Thermochemical production of liquid fuels from biomass: Thermo-economic modeling, process design and process integration analysis. *Biomass and Bioenergy*, 34 (12):1838–1854, 2010.

[**Visconti et al., 2011**] Carlo Giorgio Visconti, Enrico Tronconi, Luca Lietti, Pio Forzatti, Stefano Rossini, and Roberto Zennaro. Detailed kinetics of the fischer–tropsch synthesis on cobalt catalysts based on h-assisted co activation. *Topics in Catalysis*, 54(13-15):786–800, 2011.

[**Wang and Chen, 1991**] Wei-Jye Wang and Yu-Wen Chen. Influence of metal loading on the reducibility and hydrogenation activity of cobalt/alumina catalysts. *Applied catalysis*, 77(2):223–233, 1991.

[**Wright et al., 2010**] Mark M Wright, Daren E Daugaard, Justinus A Satrio, and Robert C Brown. Techno-economic analysis of biomass fast pyrolysis to transportation fuels. *Fuel*, 89:S2–S10, 2010.

[**Yang et al., 2010**] Jung Hoon Yang, Hak-Joo Kim, Dong Hyun Chun, Ho-Tae Lee, Jai-Chang Hong, Heon Jung, and Jung-Il Yang. Mass transfer limitations on fixed-bed reactor for fischer–tropsch synthesis. *Fuel Processing Technology*, 91 (3):285–289, 2010.

[**Yao et al., 2012**] Y Yao, X Liu, D Hildebrandt, and D Glasser. The effect of CO_2 on a cobalt-based catalyst for low temperature fischer–tropsch synthesis. *Chemical Engineering Journal*, 193:318–327, 2012.

[**Zhao et al., 2012**] Anmin Zhao, Weiyong Ying, Haitao Zhang, Hongfang Ma, and Dingye Fang. Ni–Al_2O_3 catalysts prepared by solution combustion method for syngas methanation. *Catalysis Communications*, 17:34–38, 2012.

[**Zsoldos et al., 1991**] Zoltan Zsoldos, Tamas Hoffer, and Laszlo Guczi. Structure and catalytic activity of alumina-supported platinum-cobalt bimetallic catalysts. 1. characterization by X-ray photoelectron spectroscopy. *The Journal of Physical Chemistry*, 95(2):798–801, 1991.